INVESTIGATION OF DIELECTROPHORESIS-DIRECTED FLUIDIC ASSEMBLY

A Dissertation
Presented to
the Faculty of the Department of Mechanical Engineering
University of Houston

In Partial Fulfillment
of the Requirements for the Degree
Doctor of Philosophy
in Mechanical Engineering

by
Guoliang He

August 2015

INVESTIGATION OF DIELECTROPHORESIS-DIRECTED FLUIDIC ASSEMBLY

Guoliang He

Approved:

Chair of the Committee
Dong Liu, Associate Professor,
Mechanical Engineering

Committee Members:

Tsorng-Whay Pan, Professor,
Mathematics

Matthew Franchek, Professor,
Mechanical Engineering

Anastassios Mavrokefalos, Assistant
Professor, Mechanical Engineering

Cunjiang Yu, Assistant Professor,
Mechanical Engineering

Suresh K. Khator, Associate Dean,
Cullen College of Engineering

Pradeep Sharma, Professor and
Chair, Mechanical Engineering

ACKNOWLEDGEMENTS

I would like to express my gratitude and appreciation to my advisor, Dr. Dong Liu, Associate Professor of Mechanical Engineering at University of Houston, for all his help and guidance over the duration of my graduate study and for paving the way for my future success. I have benefit a lot from not only the encouragement when I was frustrated but also his rigorous attitude towards details in scientific research, which is essential to achieving satisfaction and distinction in one's pursuits.

I would like to thank Dr. Tsorgn-Whay Pan, Professor of Mathematics, for his invaluable inputs to my numerical work, which have guaranteed the feasibility of many essential aspects of this work. I cannot imagine to accomplish such work without the help and inputs from him.

I also extend my thanks to Dr. Matthew Franchek, Professor of Mechanical Engineering, for his support and encouragement in my research and contribution to this success.

This research was supported by the National Science Foundation (Grant No. 0927340 and Grant No. 1134119). I would like to acknowledge this support and the financial support from University of Houston.

Finally, I would also like to thank my parents for their support during the course of my graduate education. And I would also like to thank all my friends who have made this journey enjoyable.

INVESTIGATION OF DIELECTROPHORESIS-DIRECTED FLUIDIC ASSEMBLY

An Abstract
of a
Dissertation
Presented to
the Faculty of the Department of Mechanical Engineering
University of Houston

In Partial Fulfillment
of the Requirements for the Degree
Doctor of Philosophy
in Mechanical Engineering

by
Guoliang He

August 2015

ABSTRACT

Dielectrophoresis (DEP)-based fluidic self-assembly of nanoscale building blocks, such as nanoparticles and nanowires, is a promising alternative to the current micro/nanofabrication techniques to manufacture functional micro/nanodevices. While individual particles can be manipulated with reasonable precision, it remains a grand challenge to scale up the assembly process to reproducibly assemble a large number of particles. This is partially due to the lack of a quantitative understanding of the complex fluid-particle dynamics when numerous nanostructures are interacting both electrically and hydrodynamically. In this work, both experiment and numerical study were conducted to explore the electrohydrodynamic effects during the assembly of multiple nanostructures driven by DEP.

Direct numerical simulations were conducted that combine the Maxwell Stress Tensor (MST) approach and the Distributed Lagrange Multiplier/Fictitious Domain (DLM/FD) method to solve the conjugate fluid-particle interaction problem. The MST approach was used to compute the DEP forces and torques exerted on the particles, which yields rigorous solutions even for highly non-uniform electric field and for particles of irregular shapes. The DLM/FD method was then employed to simulate the hydrodynamic equations of the particle-fluid system involving multiple particles. The motion of the individual particles and the subsequent aggregation of adjacent particles under three major driving mechanisms for directed self-assembly, namely, DEP, traveling-wave DEP and electrorotation, were studied in details. In addition, microfluidic DEP devices were fabricated and self-assembly experiments were carried out for polystyrene microparticles

suspended in colloidal solutions. The observed particle motion and the assembly patterns were compared to the numerical simulation results. The good agreement suggests the comprehensive numerical framework developed in this work can be used as a powerful tool for the fundamental study of colloidal hydrodynamics with coupled electrokinetic effects.

With further advancement, this work will help to push forward the development of more effective and robust fluidic assembly techniques, and lay the foundation towards large-scale parallel manufacturing of functional nanostructures for various engineering applications.

TABLE OF CONTENTS

LIST OF FIGURES

LIST OF TABLES

Chapter 1 Introduction

The burgeoning field of nanotechnology has called for new methods for fabricating and manufacturing functional structures and devices. Due to the attractive nature of intermolecular forces, the individual nanoscale building blocks, such as the nanoparticles, nanotubes and nanowires, can be assembled into functional nano- and microsystems in a bottom-up manner. The applications range from basic microelectronic components such as field-effect transistors [1-3] to more complex devices like logic circuits [4, 5] and electromechanical switches [6, 7]. Two grand challenges exist [8]: how to precisely position the nanoscale building blocks at a predefined location and orientation to form robust structures, and how to scale up the fabrication process to simultaneously produce a large number of such structures. Among various methods proposed for assembling nanostructures, the electric field guided approach, particularly, the dielectrophoresis (DEP)-directed fluidic assembly, offers the opportunity to conveniently manipulate and position the nanostructures with high precision in colloidal dispersions where the nanostructures will not stick to the solid surface due to the van der Waal force. It also has the advantage of being compatible with standard MEMS technologies, allowing on-chip assembly and integration.

Dielectrophoresis is the motion of uncharged dielectric particles when they experience a net force and torque as the result of the interaction of the induced dipole on the particles with the applied electric field [9]. DEP has been employed as a powerful tool in a broad range of applications including particle separation and concentration, drug discovery, medical diagnostics and particle self-assembly [10-14]. One prominent

advantage of DEP is its ability to precisely manipulate small particles of micron/nanometer scale without physical contact. This noninvasive feature is essential to many biological/biomedical applications where the completeness of the bioparticles must be maintained. More importantly, it enables the directed self-assembly of micro/nanoparticles into pre-defined patterns, which constitutes the foundation for the development of more complex functional structures and devices in nanomaterials and nano/microelectronics [13, 15].

At present, DEP-directed fluidic assembly is largely limited to sparsely distributed micro/nanoparticles (spherical and/or non-spherical). One significant barrier is the lack of a quantitative understanding of the complex fluid-particle dynamics when numerous particles are involved, which interact both electrically and hydrodynamically. For instance, the hydrodynamics interactions associated with DEP-directed assembly are often oversimplified by adding a friction term to the equations of motion of the particles, and very little information is known for the actual impact of the flow field on the assembly process. In addition, most available models employ the effective dipole moment (EDM) approximation to characterize the electrical interactions, which is valid only when the particles are much smaller than the feature size of the non-uniformity of the electric field [16]. Recently, a more accurate model (the immersed electrokinetic finite element method) has been applied to simulate the electrohydrodynamic coupling of nanowires with the surrounding fluid [17-19], however, the number of nanowires that can be modeled are rather small (< 10), thereby restricting its use to dilute nanowire dispersions. Therefore, the current modeling capability has lagged seriously behind the need for reliable predictive

tools that can be used to guide the design of scale-up parallel fluidic assembly of micro/nanostructures.

The overriding goal of the present work is to develop an accurate and efficient numerical model to simulate the colloidal electrohydrodynamics underlying DEP-directed fluidic assembly. The objectives are to study the movement, aggregation and collision of large number of particles undergoing DEP and to investigate the effect of various system parameters on the DEP-directed fluidic assembly. The ultimate aim is to lay the scientific foundation for large-scale parallel manufacturing of functional micro/nanostructures for engineering applications.

In this work, the numerical model is developed by combining the Maxwell Stress Tensor (MST) approach and the Distributed Lagrange Multiplier/Fictitious Domain (DLM/FD) method. The DEP forces and torques acting on each individual particle are calculated by integrating the Maxwell stress tensor over the entire surface of the particle. In the MST approach, the presence of the particle is included in the calculation of the electric field, and no assumptions need to be made regarding the field non-uniformity. This guarantees the DEP forces/torques on the particle are correctly calculated even in regions with strong gradients such as in the vicinity of the electrodes. Additionally, the MST formulation is flexible in dealing with particles of irregular shapes. The hydrodynamic particle-particle and particle-fluid interactions are solved by the DLM/FD method. In this method, the fluid-particle problem is reformulated in an extended domain, the fictitious domain, which is occupied by the fluid together with the interiors of the particles, over which the Navier-Stokes equations are enforced, and the flow inside and on each particle boundary is constrained to be a rigid-body motion using a distributed Lagrange multiplier.

By doing so, the fluid-particle interaction is treated implicitly via a combined weak formulation with which explicit calculation of the hydrodynamic forces and torques on the particles can be completely eliminated. Another advantage of this method is that, structured, regular meshes can be used which significantly improves computational efficiency by avoiding mesh-regeneration. To verify the numerical results, experiments are also conducted in this work with colloidal suspensions, in which the DEP motion of particles is recorded and analyzed. Analytical solutions, when available, are used to test the validation of the numerical model and as a guideline for experiments.

This dissertation is organized as follows. Chapter 2 introduces the application background of DEP and summarizes the primary theoretical methods to calculate the DEP forces and torques on particles. Chapter 3 details the numerical methods, including the governing equations of the particle-fluid interaction problem in the framework of the DLM/FD approach, the direct numerical simulation scheme, and the space and time discretization. Chapter 4 presents the results of the analytical solutions, numerical simulations and experiment observations of a typical DEP-directed fluidic assembly process, particle chaining in a uniform electric field. Chapter 5 describes the DEP motion of suspending colloidal particles confined in a microchannel when a traveling-wave field is applied. Chapter 6 discusses the effect of electrohydrodynamics (EHD) on the DEP-induced flow field when a temperature gradient exists. Chapter 7 describes the electrorotation of microparticles in a rotating electric field. Finally, the conclusions of the present study and recommendations for future work are summarized in Chapter 8.

Chapter 2 Fundamentals of Dielectrophoresis

Dielectrophoresis (DEP) has been employed as a powerful tool in separating, trapping, sorting and translating cells, viruses and proteins in biological and biomedical research [20-23]. A sound understanding of the fluid-particle electrohydrodynamics is indispensable for successful implementation of DEP-directed fluidic assembly. In this chapter, the historical retrospect of DEP is briefly reviewed, and the basic DEP theories are summarized. In particular, various theoretical approaches for calculating the DEP force and torque are compared to highlight the strength and versatility of the Maxwell Stress Tensor (MST) method.

2.1 A Historical Retrospect of DEP

The phenomenon of DEP was discovered back in the early twentieth century [9]. However, the first systematical study of DEP was conducted in 1950s by Pohl [24], who revealed dielectric polarization as the origin of DEP and laid the foundation for future theoretical models. His work deals with the theory of dielectrophoresis based on the polarization of matter. He also performed a series of experiments with colloidal suspensions and biological particles (yeast cells, red blood cells, chloroplasts mitochondria and bacteria) and enumerated the various factors that affect the particle separation process.

By 1980s, a bulk of the research was on the manipulation of biological cells. Pohl examined the behavior of single cells under dielectrophoresis [25] and Gvozadiak studied the separation of microorganisms from water with the help of dielectrophoresis [26]. Subsequently, optical technique of registration, which permits a simultaneous registration

of orientation and dielectrophoretic precipitation, was used to study the dielectrophoretic motion of cells and the electric properties of single cells can be extracted [27, 28].

At the same time, DEP effect on various geometry such as spheres and shells were investigated experimentally by Jones [29] who applied both direct current (DC) and alternating current (AC) signals in colloidal suspensions. Theoretically, Jones derived a general expression to estimate the dielectrophoretic forces for solid spheres and shells of lossy dielectric material in lossy dielectric medium.

In the mid of 1980's, more research were conducted on the use of dielectrophoresis for biological applications. The focus became on more sophisticated applications such as cell soring, cell lysing and cell fusion [30-33]. Electroroation on single cells was studied by Arnold and Zimmermann with a rotating electric field [34]. It provides an accurate measurement for the bio-properties, such as membrane capacity and surface conductance of a single cell.

A treatment of dielectrophoresis considering the particles to be lossy ones was given by Gherardi [35]. Instead of considering the particles to be pure dielectrics, their conductivity is also taken into account.

A few computational studies were also reported during this period. Henry performed numerical investigations on the particle collection efficiency of a fibrous filter [36]. The model took into account the effect of various factors such as dielectrophoresis, electrophoresis, Brownian motion and particle inertial and predict the collection efficiency of the filter under the influence of these factors.

Till this period dielectrophoresis was performed using electrodes made using conventional manufacturing processes. For example, the pin-plate or the wire-wire arrangement used by Pohl in his experiments or the sophisticated geometry manufactured by numerically controlled milling machines [37]. Then, the technology of manufacturing dielectrophoretic devices was revolutionized [38-40] by introducing a novel device called fluid integrated circuit (FIC) [38]. In this device all the components were integrated into a single substrate using photolithography techniques. These were the first dielectrophoretic devices manufactured using MEMS manufacturing process. Using FIC, they were able to accurately control the electrostatic and hydrodynamic forces and therefore the manipulation of single cells [39].

This microfabrication technique was quickly adopted by Pethig for biological dielectrophoresis using microelectrodes [41]. The device has interdigitated castellated microelectrode design for live yeast suspension [41, 42]. The yeast cells were observed to experience positive dielectrophoresis above 10 kHz and negative dielectrophoresis below 500 Hz [43]. Another contribution by Pethig was the studies of dielectrophoretic electrorotation [44-46]. He derived new theoretical relationships linking the dielectric properties of a colloidal suspension to both conventional dielectrophoresis and electrorotation.

Electrorotation was later used to study cells, DNA and microorganism [47-49]. The properties of polarizability and conductivity are chosen as two typical parameters for the research by Jones [50]. He derived methods for determining the electrorotation forces and torques exerted by nonuniform electric fields on biological particles suspended in aqueous media. Electrorotation devices were usually fabricated as four neighboring electrodes with

consecutive 90° phase-shift. The electrodes can be as simple as platinum wires of 0.1 mm diameter bent in a U-turn shape by Holzel [51] in early years and as complicated as microfabricated electrodes designed with CAD software and used as electrical tweezer by Swami [52]. Negative dielectrophoresis comes along with electrorotation as dielectrophoretic field cage [53], which provides trapping and holding forces.

Besides electrorotation, the phenomena of travelling-wave dielectrophoresis also attracted extensive attention. This phenomena was originally observed by Batchelder in 1983 [54]. Later, Fuhr were investigating this effect as the linear analog of dielectrophoresis [55, 56]. In order to obtain travelling wave dielectrophoresis, microelectrodes were arranged linearly with each electrode 90° phase advanced than the last [55], similar to electrorotation. This produces an electric field that travels with the electrodes and the polarized particle will also move along with the field. Liu and Garimella then developed the traveling-wave dielectrophoresis into an effective means for microfluidic flow actuation [57]. A prototype dielectrophoretic micropump was built and the experimental characterization of the induced flow velocity were reported and compared with numerical simulations. They showed that by the interaction of the particle with the surrounding fluid, the particles actuated by traveling-wave dielectrophoresis can generate fluid flow inside the microfluidic channel.

Theoretically, there had been three main analytical approaches in calculating the dielectrophoretic force experience by particles in a suspension. The first one is the energy variation principle in which the particles and the suspending medium are treated as loss free dielectrics [58]. The second approach is the effective dipole/multipole method [59]. The third approach is based on the Maxwell stress tensor method, which involves the

integration of the stress tensor on the entire particle surface [16]. Other methods such as image method were not widely used because it only applies to a certain simplified boundary condition [60]. These methods are compared and discussed in this work.

When it comes to the numerical simulations of dielectrophoresis, at first, most of the studies are limited to the prediction of the electric field developed in the dielectrophoretic devices and the trajectories of the particle motion, without simulating the actual fluid-particle system [61, 62]. Then Kadaksham and Singh developed a numerical method based on the distributed Lagrange multiplier method for the direct simulation of electrorheological liquids [63, 64]. However, in their works, dipole approximation was adopted for dielectrophoretic force calculation. Liu Y. also proposed a new method for modelling the electrokinetic-induced mechanical motion of particles in a fluid domain with immersed finite element method [65]. Assembly process of nano/biomaterials of various geometries were studied with this method. The interactions between a few particles (less than 10) were investigated by Ai, House and Kang [66-69] in order to achieve precise control over the motion of the particles.

2.2 Basic Theory of Dielectrophoresis

DEP is the motion of uncharged particles when they experience a net force and torque as the result of the interaction of the induced dipole on the particles with the applied electric field [9]. In the simplest case, a dielectric particle suspended in a fluid medium is exposed to an applied external electric field (as shown in Figure 1). The electrical charges redistribute in the particle, and net charges are established at the interface between the particle and the fluid, forming an induced dipole across the particle. The induced dipole

tends to align with the applied field. The induced dipole moment, $\vec{p}$, and the dielectrophoretic force, $\vec{F}$, are given by [70]

$$\vec{p} = 4\pi r^3 \varepsilon_m \left(\frac{\varepsilon_p - \varepsilon_m}{\varepsilon_p + 2\varepsilon_m} \right) \vec{E} \quad \text{and} \tag{1}$$

$$\vec{F} = \left(\vec{p} \cdot \nabla \right) \vec{E} \ , \tag{2}$$

in which r is the radius of the particle, $\vec{E}$ is the applied electric field vector, and ε_m and ε_p are the dielectric permittivity of the fluid medium and the particle, respectively. If the applied field is non-uniform ($\nabla \vec{E} \neq 0$), the particle will experience a net force, and the resulting translational and rotational motion of the particle is termed dielectrophoresis [24, 41]. It is noted that Eq. (1), or the effective dipole model, is valid only if the particle is much smaller than the length scale of the spatial variation of the electric field, which is also known as the dipole approximation. More accurate approaches to calculate the dielectrophoretic force will be discussed later in this chapter.

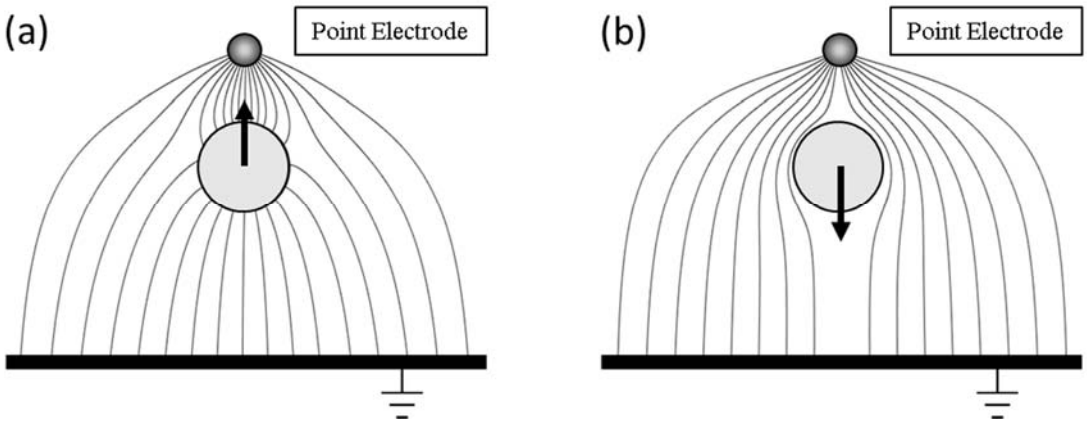

Figure 1. A sketch of positive DEP force (a) and negative DEP force (b) on a dielectric particle.

According to Eq. (2), the direction of the dielectrophoretic force and, therefore, the DEP-induced particle motion with respect to the applied field depend on the relative permittivity of the particle and the surrounding fluid medium. If the particle is more polarizable ($\varepsilon_p > \varepsilon_m$), it experiences an attractive force and will move toward the local maxima of the electric field. This process is called positive DEP. In an opposite situation, the less polarizable particle ($\varepsilon_p < \varepsilon_m$) will move away from the local maxima of the field, leading to negative DEP. In Figure 1(a), the particle is more polarizable than the fluid and, hence, the electric flux lines bend towards the particle, meeting its surface as if it were a metal particle. Consequently, the field intensity near the upper portion of the particle is greater than that near the lower portion, leading to an imbalance of forces on the particle. The induced dipole conforms to the direction of the applied field, and the particle is attracted the point electrode where the maximum electric field exists, i.e., positive DEP occurs. Similarly, Figure 1(b) illustrates the negative DEP for a particle that is less polarizable than the medium.

DEP takes place not only in direct current (DC) but also in alternating current (AC) electric fields. Sustained particle motion only occurs in AC DEP with the appropriate driving frequencies (in particular, in traveling-wave DEP), for which case, the permittivity ε in Eq. (1) is replaced by the frequency-related counterpart,

$$\tilde{\varepsilon} = \varepsilon - i\frac{\sigma}{\omega}\ , \tag{3}$$

in which ε and σ are the permittivity and electrical conductivity, and ω is the angular frequency of the electric field.

For a spherical particle suspended in a fluid in an AC electric field, the corresponding dipole moment is expressed as

$$\vec{p} = 4\pi r^3 \varepsilon_m \left(\frac{\tilde{\varepsilon}_p - \tilde{\varepsilon}_m}{\tilde{\varepsilon}_p + 2\tilde{\varepsilon}_m} \right) \vec{E} \ . \tag{4}$$

Hence, the dielectrophoretic force on the particle becomes

$$\vec{F}_{DEP} = \left(\vec{p} \bullet \nabla \right) \vec{E} = 4\pi r^3 \varepsilon_m \left(\frac{\tilde{\varepsilon}_p - \tilde{\varepsilon}_m}{\tilde{\varepsilon}_p + 2\tilde{\varepsilon}_m} \right) \nabla \vec{E}^2 \ , \tag{5}$$

where the complex relative permittivity is also referred to as Clausius-Mossotti factor f_{CM}

$$f_{CM} = \frac{\tilde{\varepsilon}_p - \tilde{\varepsilon}_m}{\tilde{\varepsilon}_p + 2\tilde{\varepsilon}_m} \ . \tag{6}$$

Assuming the electric field varies with a single angular frequency ω, the time-averaged dielectrophoretic force can be computed as [71]

$$\left\langle \vec{F}_{DEP} \right\rangle = \pi r^3 \varepsilon_m \, \mathrm{Re}\left[f_{CM} \right] \nabla \left| \vec{E} \right|^2 + 2\pi r^3 \varepsilon_m \, \mathrm{Im}\left[f_{CM} \right] \left(E_x{}^2 \nabla \varphi_x + E_y{}^2 \nabla \varphi_y \right), \tag{7}$$

where Re[f_{CM}] and Im[f_{CM}] denote the real and imaginary parts of f_{CM}, and E_x, E_y and E_z are components of the electric field vector; φ_x, φ_y and φ_z are the phase angles if the electric field is spatially phase-shifted. It is noted that the DEP force depends on the spatial non-uniformities in both the field strength ($\nabla \left| \vec{E} \right|^2$) and the phase ($\nabla \varphi$). In fact, the first term on the RHS of Eq. (7) determines the alignment of the DEP force with respect to the maxima/minima of the electric field and is the regular DEP force component in DC DEP. The second term on the RHS of Eq. (7) only appears if the electric field has a spatially

varying phase, such as in a traveling-wave field, and therefore is the traveling-wave DEP (twDEP) force component.

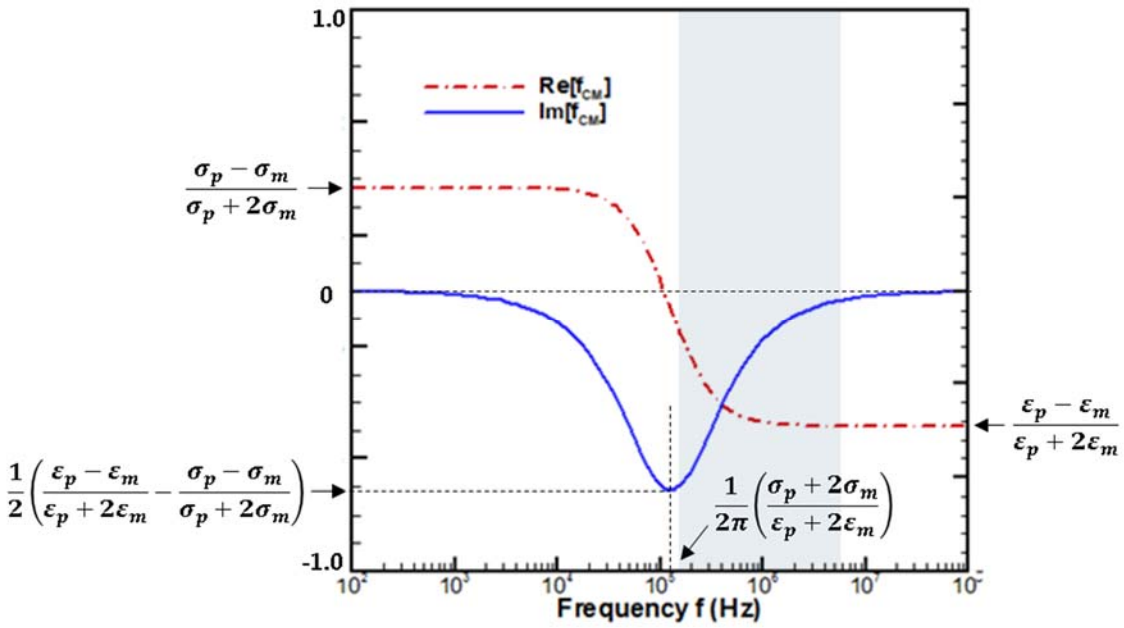

Figure 2. Real and imaginary components of Clausius-Mossotti factor as a function of frequency.

The alignment of the DEP force with the applied field is contingent upon the Clausius-Mossotti factor f_{CM}, which is frequency-dependent. Figure 2 illustrates the real and imaginary parts of f_{CM} as a function of the frequency of the applied field for polystyrene particles suspended in water. Clearly, Re[f_{CM}] is positive in the low-frequency range ($f <$ 1 kHz) in which the particles are more polarizable than the surrounding fluid, and crosses over to negative values as the frequency increases ($f >$ 100 kHz) and the particles become less polarizable than the fluid. If Re[f_{CM}] > 0, the regular DEP force component aligns favorably with the field strength gradient, as indicated by Eq. (7). As a result, the particles move towards the maxima of the electric field, which are usually located at the edges of the electrodes that are used to generate the electric field, and positive DEP occurs. In the

opposite situation, a negative Re[f_{CM}] brings about negative DEP where the particles move away from the maxima of the electric field, distancing themselves from the electrodes.

The imaginary component of the Clausius-Mossotti factor, f_{CM}, plays an important role in twDEP and electrorotation. Im[f_{CM}] vanishes at both extremes of the frequency spectrum but assumes non-zero values in the mid-range around the cross-over frequency. The maximum of the absolute value of Im[f_{CM}] occurs at a relaxation frequency (known as Maxwell-Wagner frequency [72])

$$f_{MW} = \frac{1}{2\pi}\left(\frac{\sigma_p + 2\sigma_m}{\varepsilon_p + 2\varepsilon_m}\right) \tag{8}$$

and the corresponding value of Im[f_{CM}] is

$$\mathrm{Im}\left[f_{CM}\right] = \frac{1}{2}\left(\frac{\varepsilon_p - \varepsilon_m}{\varepsilon_p + 2\varepsilon_m} - \frac{\sigma_p - \sigma_m}{\sigma_p + 2\sigma_m}\right). \tag{9}$$

When Im[f_{CM}] is not trivial, the resulting twDEP force in Eq. (7) propels the particles along or against the propagating traveling-wave field depending on the sign of Im[f_{CM}]. Traveling-wave DEP can be exploited to achieve long-range transport of nanoscale components to desired on-chip sites for assembly. The twDEP force is generally oriented in parallel to the electrode plane. However, in practice, twDEP does not occur in isolation without the companion negative DEP, since the particles must be levitated from the electrode surface. As such, the criteria for effective twDEP are Re[f_{CM}] < 0 and Im[f_{CM}] ≠ 0, which are designated by the shaded area on the frequency spectrum in Figure 2. More details of twDEP and electrorotation will be discussed in Chapters 5 and 7.

DEP is produced by applying voltage signals to specially designed electrode arrays, and the solution of the electric field is required for the calculation of DEP forces and torques on the particles. For the range of current and frequency typically found in DEP problems, the electric field can be described by the quasi-electrostatic form of the Maxwell equations [62]

$$\vec{E} = -\nabla\phi \ , \tag{10}$$

$$\frac{\partial\rho}{\partial t} + \nabla\cdot\left(\sigma\vec{E}\right) = 0 \quad \text{and} \tag{11}$$

$$\nabla\cdot\left(\varepsilon\vec{E}\right) = \rho \ , \tag{12}$$

where ε and σ are the electric permittivity and conductivity of the dielectric materials and ρ is the free charge density. Eqs. (10) - (12) must be solved with proper boundary conditions, which are set by the geometry of the electrodes and the applied voltage signals.

Under an AC field with an angular frequency ω, by using the phasor expression, the Maxwell equation can be reduced to

$$\nabla\cdot\left[\left(\sigma + j\omega\varepsilon\right)\nabla\tilde{\phi}\right] = 0 \ , \tag{13}$$

where $\tilde{\phi} = \phi_R + j\phi_I$, and the real and imaginary components of the phasor satisfy the Laplace's equation $\nabla^2\phi_R = 0$ and $\nabla^2\phi_I = 0$, and $j = \sqrt{-1}$. In other words, the electric potential for an AC field of angular frequency ω is [71]

$$\phi\left(\vec{x},t\right) = \phi_R\cos\left(\omega t\right) + \phi_I\sin\left(\omega t\right) . \tag{14}$$

After solving for the electric potential, the electric field is obtained from

$$\vec{E}\left(\vec{x},t\right) = -\nabla\phi = \vec{E}_R\left(x,y\right)\cos\left(\omega t\right) + \vec{E}_I\left(x,y\right)\sin\left(\omega t\right), \tag{15}$$

where $\vec{E}_R\left(x,y\right) = -\nabla\phi_R$ and $\vec{E}_I\left(x,y\right) = -\nabla\phi_I$.

Past analytical solutions include approaches using Fourier series [71], the Green's theorem [73], and the half-plane Green's function [42, 74], while semi-analytical methods include the charge density method [42] and the Green's function for a line source with conformal mapping [75]. All these solution approaches have used a linear approximation of the electric potential in the gap between consecutive electrodes as the boundary condition. It has been shown that this is not a good assumption and can cause large errors in the analysis [57]. The calculation can be improved by employing numerical method [62].

2.2.1 Multipole Approximation

The effective dipole model (Eq. (5)) is the most common for the calculation of DEP force due to its simplicity, however, its validity is questionable when the particle size is comparable to the characteristic length scale of the electric field non-uniformity, e.g., in the vicinity of the electrode, or when the inter-particle distance becomes comparable to the particle size in the case of multiple particle interactions. Therefore, a more precise estimate of the DEP force should be employed which takes into account of the higher-order multipoles [76-78]. In the framework of this general moment theory, the *n*th-order multipolar moment $\vec{p}^{(n)}$ is first calculated

$$\vec{p}^{(n)} = \frac{4\pi\varepsilon_m a^{2n+1} n}{n!(n-1)!} f_{CM}^{(n)} (\nabla)^{n-1} \vec{E}\,, \tag{16}$$

where $f_{CM}^{(n)}$ is the n[th] order Clausius-Mossotti factor $f_{CM}^{(n)} = \frac{\tilde{\varepsilon}_p - \tilde{\varepsilon}_m}{n\tilde{\varepsilon}_p + (n+1)\tilde{\varepsilon}_m}$, $\nabla^{(n)}$ signifies the *n*th-order derivative, and $\vec{E}$ is the applied electric field. Accordingly, the DEP force can be calculated by summing up all multiple contributions [47, 79]

$$\left\langle \vec{F}_{DEP} \right\rangle = \frac{1}{2} \sum_{n=1}^{\infty} \mathrm{Re}\left[\frac{\vec{p}^{(n)} \bullet \nabla^{(n)} \vec{E}}{n!} \right], \tag{17}$$

where $\langle\ \rangle$ represents the time average of a time-dependent quantity

$$\left\langle X \right\rangle = \lim_{T\to\infty} \frac{1}{T} \int_{t_0}^{t_0+T} X\, dt\ , \tag{18}$$

where X is integrated from an arbitrary starting time t_0 to a sufficiently large time T.

Clearly, the effective dipole model is the first order approximation of the multipole moment model. The higher-order terms are trivial compared to the first-order term.

It should be noted that closed-form solution of the DEP force, such as Eq. (17), is *only* available for spherical particles, and there is no general analytical formula for particles of arbitrary geometries. Green and Jones [80] developed a semi-analytical model to determine the higher-order moments $\vec{p}^{(n)}$ for non-spherical particles, specifically, cylindrically symmetric particles [80].

$$p^{(n)} = 4\pi\varepsilon_m R_t^{n+1} \frac{2n+1}{2} \int_0^{\pi} \Phi_{R_t} P_n(\cos\theta) \sin\theta d\theta\ , \tag{19}$$

where θ the polar angle in spherical coordinates, $P_n(\cos\theta)$ the Legendre polynomials,

$$P_1 = \cos(\theta), \quad P_2 = \left(3\left[\cos(\theta)\right]^2 - 1\right)/2, \quad \ldots , \tag{20}$$

Φ_{R_t} is the electrical potential due to the particle on the spherical surface given by r = R_t, which is determined from the numerical solution, φ_{FEM} , by subtracting the potential from the applied field:

$$\Phi_{R_t} = [\varphi_{FEM} - \varphi_{applied}]_{r=R_t} , \tag{21}$$

which indicates that this method is a semi-analytical model. In other words, this method uses the analytical expressions for the higher order potentials along with numerical solutions of these potentials to calculate the values of individual moments.

By combining Eqs. (16) and (18), higher-order effective moments and the corresponding order dielectrophoretic forces can be obtained. The accuracy of this method has been verified by comparing the calculated DEP force for a variety of particle shapes, such as sphere, truncated cylinder and ellipsoid, with the results obtained with FEM simulations.

2.2.2 Maxwell Stress Tensor (MST) Approach

In view of the inherent drawbacks of the effective dipole and multipole moment methods, the Maxwell Stress Tensor (MST) approach was developed for the calculation of the DEP force and torque [16]. The MST formulation is regarded the most rigorous approach since the presence of the particle is included in the calculation of the electric field, and no assumptions need to be made regarding the field non-uniformity. This

guarantees the DEP force on the particle is correctly calculated even in regions with strong gradients such as in the vicinity of the electrodes. In addition, the MST approach is very flexible in dealing with particles of irregular shapes.

In this model, the DEP force is computed through a surface integral

$$\left\langle \vec{F}_{DEP}^{MST} \right\rangle = \oint \left(\vec{\vec{\sigma}}^{M} \cdot \vec{n} \right) dA \tag{22}$$

and the electrorotation torque is given by

$$\left\langle \vec{\tau}_{E} \right\rangle = \oint \vec{r} \times \left(\vec{\vec{\sigma}}^{M} \cdot \vec{n} \right) dA , \tag{23}$$

where $\vec{n}$ is the unit vector normal to the surface, the Maxwell stress tensor is $\vec{\vec{\sigma}}^{M} = \frac{1}{4}\mathrm{Re}\left(\tilde{\varepsilon}_{m}\right)\left[\left(\vec{E}\vec{E}^{*} + \vec{E}^{*}\vec{E}\right) - \left|\vec{E}\right|^{2}\vec{\vec{I}}\right]$, A is the surface enclosing the particle, and $\vec{\vec{\sigma}}^{M}$ is the Maxwell stress tensor defined as

$$\vec{\vec{\sigma}}^{M} = \tilde{\varepsilon}\left[\vec{E}\vec{E} - \frac{1}{2}\left|\vec{E}\right|^{2}\vec{\vec{I}}\right] + \tilde{\mu}\left[\vec{H}\vec{H} - \frac{1}{2}\left|\vec{H}\right|^{2}\vec{\vec{I}}\right] , \tag{24}$$

where $\tilde{\varepsilon}$ is the complex electric permittivity, $\tilde{\mu}$ the complex magnetic permeability, $\vec{E}$ the electric field, $\vec{H}$ the magnetic field, $\vec{\vec{I}}$ the unit tensor, and the product of two vectors without a dot denotes the dyadic product.

In DEP studies, the frequency of the applied electric field is usually much lower than 100 MHz. Considering the near field approximation [16], the corresponding wavelength is several orders of magnitude larger than the DEP device. Therefore, the effect of magnetic field can be neglected, and the MST reduces to

$$\ddot{\sigma}^M = \tilde{\varepsilon}\left[\vec{E}\vec{E} - \frac{1}{2}\left|\vec{E}\right|^2 \ddot{I}\right] . \tag{25}$$

For a harmonic AC field, the electric field can be written as

$$\vec{E}(\vec{r},t) = \mathrm{Re}\left[\vec{E}\cdot e^{jwt}\right] = \frac{1}{2}\left(\vec{E}+\vec{E}^*\right) , \tag{26}$$

where $\vec{E}^*$ is the conjugation of the complex electric field $\vec{E}$. Using this notation, the Maxwell stress tensor in Eq. (25) becomes

$$\ddot{\sigma}^M = \frac{1}{4}\mathrm{Re}\left[\tilde{\varepsilon}\right]\left[\left(\vec{E}+\vec{E}^*\right)\left(\vec{E}+\vec{E}^*\right) - \frac{1}{2}\left(\vec{E}+\vec{E}^*\right)\cdot\left(\vec{E}+\vec{E}^*\right)\ddot{I}\right] , \tag{27}$$

which can be considered as the sum of two tensors,

$$\ddot{\sigma}_1^M = \frac{1}{4}\mathrm{Re}\left[\tilde{\varepsilon}\right]\left[\vec{E}\vec{E}^* + \vec{E}^*\vec{E} - \left|\vec{E}\right|^2 \ddot{I}\right] \text{ and} \tag{28}$$

$$\ddot{\sigma}_2^M = \frac{1}{4}\mathrm{Re}\left[\tilde{\varepsilon}\right]\left[\vec{E}\vec{E} + \vec{E}^*\vec{E}^* - \frac{1}{2}\left(\vec{E}\cdot\vec{E} + \vec{E}^*\cdot\vec{E}^*\right)\ddot{I}\right] . \tag{29}$$

When calculating the time average of Eq. (29), it can be shown that the instantaneous term $\ddot{\sigma}_2^M$ equals to zero after expanding [16], which leads to $\left\langle \ddot{\sigma}^M \right\rangle = \ddot{\sigma}_1^M$. Hence, the time-averaged DEP force and torque on a particle can be obtained via integrating the tensor over the surface of the particle

$$\left\langle \vec{F}_{DEP}^{MST} \right\rangle = \frac{1}{4}\mathrm{Re}\left[\tilde{\varepsilon}\right]\oint\left(\vec{E}\vec{E}^* + \vec{E}^*\vec{E} - \left|\vec{E}\right|^2 \ddot{I}\right)\cdot\vec{n}dA \text{ and} \tag{30}$$

$$\left\langle \vec{\tau}_E \right\rangle = \frac{1}{4}\mathrm{Re}\left[\tilde{\varepsilon}\right]\oint\vec{r}\times\left(\vec{E}\vec{E}^* + \vec{E}^*\vec{E} - \left|\vec{E}\right|^2 \ddot{I}\right)\cdot\vec{n}dA . \tag{31}$$

The surface integrals in Eqs. (30) and (31) can be computed numerically using either finite element or finite difference method.

2.3 Comparison of Various Models for DEP Calculation

In this section, various approaches for DEP force/torque calculation will be compared using a point-to-plate system shown in Figure 3. The distance between the particle and the point electrode and the aspect ratio of the particle are discussed.

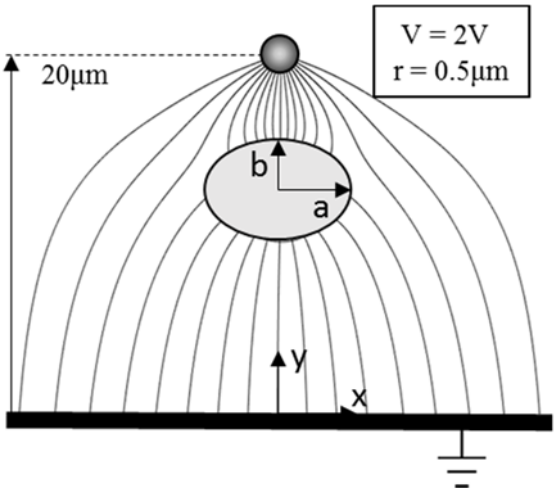

Figure 3. Scheme of the point-plate electrode structure.

The electric field is generated by placing a point electrode above a ground plate with a separating distance of 20 μm. The point electrode has a radius of 0.5 μm and the applied voltage is 2 V. The sketch of the field lines is plotted in Figure 3. In this study, the relative electric permittivities of the particle and the surrounding medium are specified as 2.8 and 78.4, respectively, which correspond to polystyrene and deionized (DI) water typically used in DEP experiments. The electric field is obtained by solving the Gauss equation

$$\nabla^2 \phi = 0 \tag{32}$$

with the following boundary conditions:

$$\phi\big|_{y=0} = 0 \quad \text{and} \tag{33}$$

$$\frac{\partial \phi}{\partial n} = 0 \qquad on \quad \partial P_i(t), i = 1, ..., N \ . \tag{34}$$

The contours of the electrostatic potential, Φ, and the electric field strength, $|E|$, are shown in Figure 4(a) and (b). The distributions of Φ and $|E|$ along the symmetric axis (x = 0) are also presented as a function of the vertical position y to illustrate the numeric values. It is seen that the electric field is largely uniform, but exhibit a sharp increase when approaching the point electrode. The contour of $|\nabla E|$ is plotted in Figure 4(c), from where it is found that $|\nabla E|$ is almost trivial in the space except for near the point electrode.

In dipole approximation, the DEP force is proportional to $\nabla \vec{E}^2$ (whose magnitude is $E \cdot |\nabla E|$), hence, the magnitude of the DEP force calculated via this assumption will increase if $|\nabla E|$ increases. In multipole approximation, the magnitude of the DEP force is proportional to $\nabla^{(n)} \vec{E}$ (n = 1, 2, 3 …), which are maximum near the point electrode from Figure 4 contours on the left. Thus it can be predicted that the dielectrophoretic forces calculated by dipole/multipole approximation, according to Eq. (16), are significantly greater near the point electrode than other regions.

On the RHS of Figure 4, it is clearly shown how the existence of a particle affects the local potential and the according electric field strength. As follows, the DEP force is

computed and compared for an elliptic particle and a circular particle placed at various vertical locations (along y-direction in Figure 4).

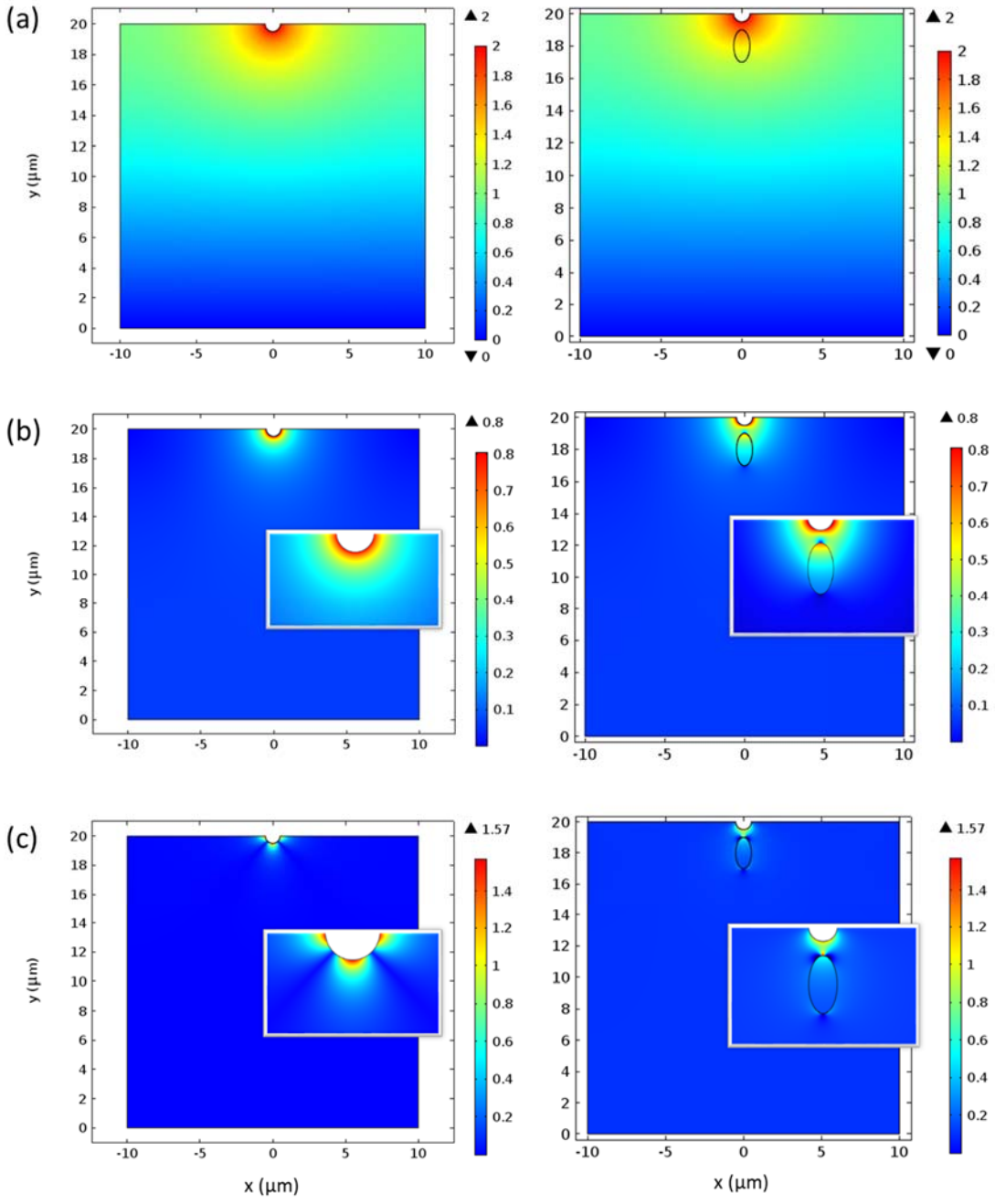

Figure 4. Electric field potential (a), strength (b) and gradient of the electric field strength (c).

2.3.1 DEP force on Circular Particle

The 2D particles are the simplified versions of the ellipsoidal and spherical particles. In particular, the elliptic shape is chosen as a representative of the non-spherical (non-circular) particles. The semi-major and semi-minor axes are a and b along the x- and y-direction, respectively (as shown in Figure 3). The circular particle is considered as a special case of the elliptic particle when a = b.

Circular particles of three different radii are considered, (a) r = 1 μm, (b) r = 0.8 μm and (c) r = 0.5 μm, in order to examine how the particle size with respect to field non-uniformity affects the accuracy of DEP force calculation. The DEP force with first order approximation (dipole) and second order approximation (multipole) are

$$\left\langle \vec{F}_{DEP} \right\rangle = \frac{1}{2}\mathrm{Re}\left[\vec{p}\bullet\nabla\vec{E} \right] \quad \text{and} \tag{35}$$

$$\left\langle \vec{F}_{DEP} \right\rangle = \frac{1}{2}\mathrm{Re}\left[\vec{p}\bullet\nabla\vec{E} + \frac{1}{2}\left(\vec{p}^{(2)}\bullet\nabla^{(2)}\vec{E} \right) \right] . \tag{36}$$

Figure 5 shows the DEP forces on the particle calculated from the dipole approximation (Eq. (17) and n = 1), the multipole approximation (Eq. (17) and n = 2) as well as the MST approach, respectively. The negative value of the DEP force indicates negative DEP is taking place, i.e., the particle will be repelled from the point charge, since $\varepsilon_p < \varepsilon_m$ for the polystyrene-water combination. It is seen that as the particle is positioned closer to the point electrode, the magnitude of the DEP forces increase drastically, and, more importantly, the variance in the three model predictions widens.

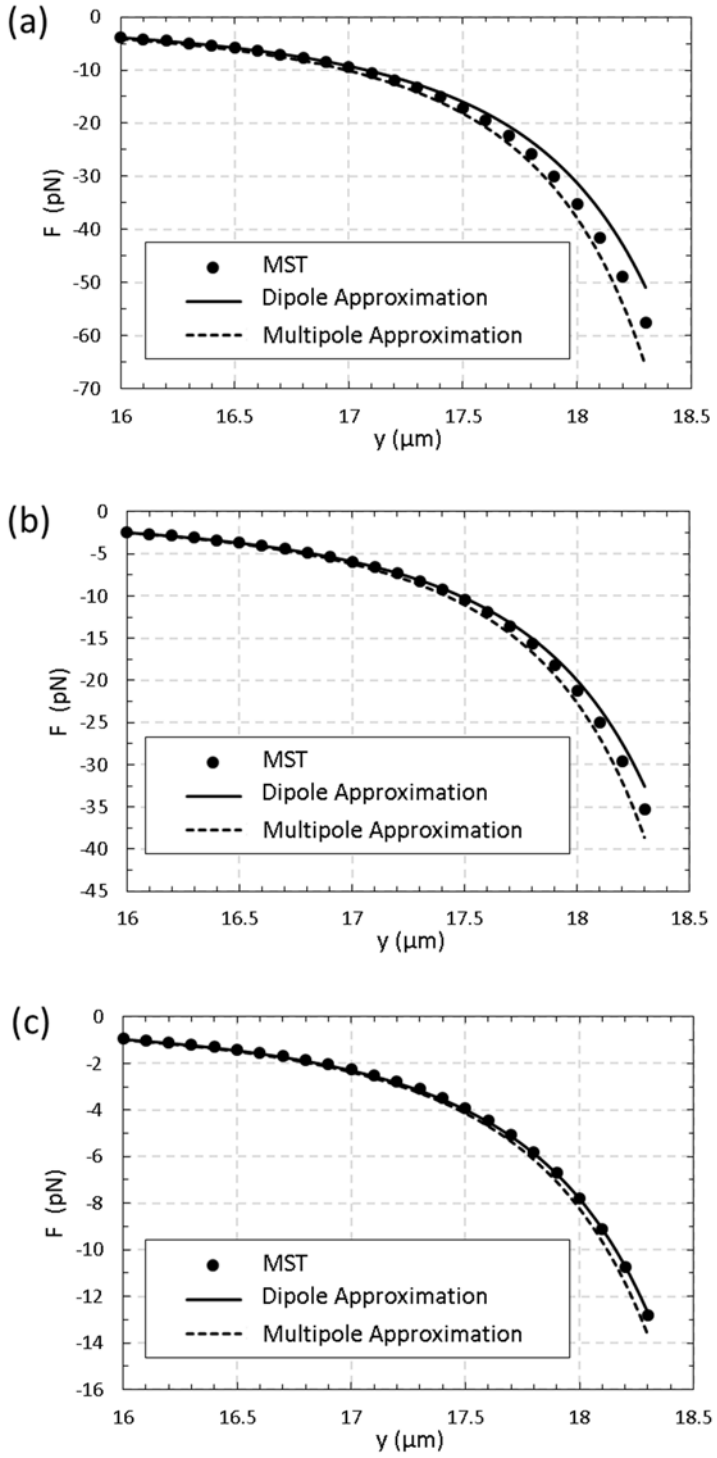

Figure 5. Forces on circular disk particles positioned along y axis.

This is due to the fact that the field non-uniformity becomes stronger near the electrode (refer to Figure 4(c)) that renders the dipole and multipole approximations less accurate compared to the MST approach. However, the variance diminishes as the particle size decreases, and the results eventually converge for the smallest particle size (Figure 5(c)).

Table 1 shows the non-uniformity factor [81] and the relative error with respect to the MST model prediction, which are defined as

$$f = \frac{E_{\max} - E_{av}}{E_{av}} \times 100\% \quad \text{and} \tag{37}$$

$$Err = \left| \frac{F_{DM} - F_{MST}}{F_{MST}} \right| \times 100\% \ , \tag{38}$$

where $E_{\max}$ is the maximum value of electric field intensity inside the particle, E_{av} is the average value, F_{DM} is the DEP force acting on a particle from dipole or multipole approximation and F_{MST} is the force calculated by Maxwell stress tensor.

It is found that the error of the dipole moment model is 11.63% for 1 μm diameter particle, and drops to 0.38% as the Non-uniformity factor decreases, which means the electric field is more uniform. Similar observations can be made for the multipole moment model as the errors decrease with the non-uniformity of the electric field. Overall, the multipole approximation performs better than the dipole approximation at any given non-uniformity value. However, the error is not negligible if electric field has been distorted in a manner.

Table 1. Dipole approximation errors vs. non-uniformity of the electric field.

Non-uniformity Factor (%)	Dipole Approximation Error (%)	Multipole Approximation Error (%)
8.00	11.63	8.69
7.00	8.44	6.10
6.07	7.65	2.43
5.14	1.09	0.87
4.13	0.78	0.44
3.95	0.38	0.31

2.3.2 DEP force on Elliptical Particle

Figure 6 shows the DEP forces calculated for an elliptic particle whose major axis is aligned with the x-direction. Two different particle aspect ratios (defined as $r = b/a$) are considered, 0.5 in Figure 6(a) and 0.25 in Figure 6(b), where the semi-major axis is kept constant, $a = 1$ μm. The general trend of the DEP force is similar to that for the circular particle.

As the particle approaches the point electrode, the contribution from higher-order terms of multipole moment to the DEP force becomes more important, which is evidenced by the larger discrepancy between the dipole prediction and the MST. In general, the errors in the DEP calculation from multipolar moment models are much greater for elliptic particles than for circular particles, given identical particle volume. For instance, at z = 16 μm, the error in the dipole approximation for a circular particle ($a = 1$ μm) is 1.01%, as compared to the error of 20.0% for an elliptic particle of aspect ratio $r = 0.5$ at the same location. For an elliptic particle of a smaller aspect ratio $r = 0.25$, the error further increases to 41.3%.

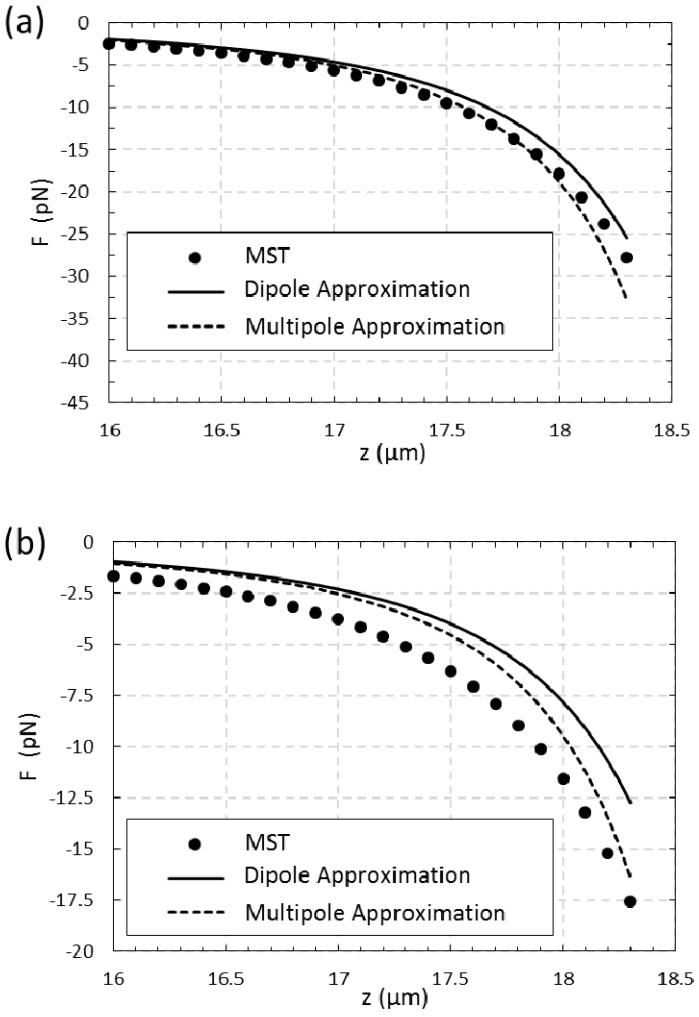

Figure 6. Forces on ellipse particles positioned along y axis.

Chapter 3 Computational Models and Numerical Methods

Assembly and manipulation of nano/biomaterials are of great interest and have become feasible with the development of advanced micro/nanoscale devices [14, 65, 66, 82]. Among the applications, there is growing interest in the manipulation of individual polymer particles or cells [68, 69]. Forces resulting from an electric field can be advantageous for the manipulation of micro/nanoscale particles because both the amplitude and the direction of forces can be controlled by the applied electric field strength and frequency [83]. However, the fundamental mechanisms are not fully understood due to the complexity of the assembly processes at the micro/nanoscale. The underlying mechanisms of electric field-driven assembly are yet to be elucidated, i.e., how large-scale assembly can be achieved in a precise manner by the electric/flow field-guided methods. The main reason is that the potential for solid-liquid flows has yet to be fully realized.

The fluid-particle and particle-particle interactions, both hydrodynamic and electrodynamic, are essential to the DEP-directed fluidic assembly of micro/nanoparticles. In the simplest case, the motion of a single particle under the influence of DEP can be described by the Stokes' law, which states the particle's instantaneous velocity is determined by balancing the DEP force with the drag force [82]. However, this model is only valid for sparsely distributed particles because it ignores the electrohydrodynamic interactions between neighboring particles. When multiple particles are considered, a myriad of direct numerical simulation methods, which originate from the study of particulate flows, can be exploited to accurately capture the fluid-particle interactions [64, 65, 84].

Several approaches exist for numerical modeling of particulate flows, which may be classified according to the length scale of numerical resolution compared with the length scales of the domain of interest (i.e., the size of industrial equipment), the flow scales or the size of the individual particles. At the fine extreme of the spectrum, Direct Numerical Simulation (DNS) methods have the capability of resolving all length and time scales and present an alternative route to experimentation for fundamental studies. Several approaches exist here as well, including Arbitrary Lagrangian-Eulerian (ALE) methods with moving grids in changing geometries [85, 86], lattice-Boltzmann methods (LBM) [87, 88], immersed finite element method [19], and distributed Lagrange multiplier / fictitious domain methods [84, 89-92]. The ALE approach enables accurate solution, but the computational cost is very high due to the need for re-meshing at each time step, especially when many particles are considered in the analysis. LBM gains increasing popularity in simulating complex fluid systems and is usually applied to study wetting and spreading phenomena [93], bubble collision and bubble rising phenomena [94]. The immersed finite element method was combined with the electrokinetic theory by Liu [19, 65] as the immersed electrokinetic finite element method (IEFEM), which can be used to model particles of irregular shapes in an electric field.

In this work, a new methodology is developed by combining the distributed Lagrange multiplier/fictitious domain (DLM/FD) method with the Maxwell Stress Tensor (MST) approach to simulate the electrohydrodynamic fluid-particle interactions for DEP-directed fluidic assembly. As discussed in Chapter 2, the MST approach is known for its precision in modeling DEP forces and torques. On the other hand, the DLM/FD method [91] is a powerful method to solve incompressible NS equations, based on the explicit

utilization of Lagrange multipliers defined on the actual boundary and associated to the genuine boundary conditions. It employs a global variation formulation, which obviates the need to compute the hydrodynamic forces due to the fluid-particle and particle-particle interactions explicitly in the simulation. Moreover, regular structured grids (which are not boundary fitted) are used in the DLM/FD method over a simple shape auxiliary domain (the fictitious domain) to solve the NS equations around the moving bodies (i.e., the particles). Hence, accurate solutions of the DEP flow involving interaction of numerous particles can be obtained with reasonable computational cost.

3.1 Solution Strategy

As illustrated in Figure 7, the computational flow chart consists of two modules. For a given electrode configuration and the initial spatial distribution of particles, the first MST module (marked by the blue box) analyzes the electric field by solving the electrostatic problem, and calculates the DEP forces and torques by integrating the Maxwell stress tensor over the surfaces of the particles. The resulting forces/torques are passed on as the external forces on the individual particles to the second DLM/FD module (marked by the red box). Then, the hydrodynamics problem is solved to yield detailed information of the flow field as well as the particle motion, the latter including the orientation and translational/rotational velocities of the particle. This completes the computation at one time step. Subsequently, the locations of the particles are updated and the simulation moves to the next time step. In this work, FORTRAN 77 is used to implement the algorithms.

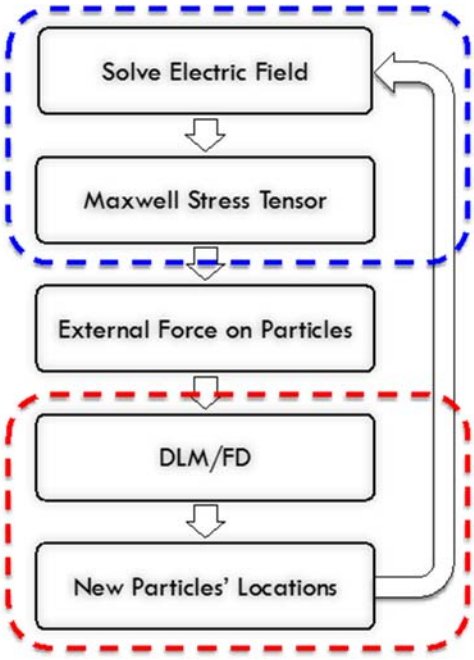

Figure 7. Solution strategy with electric solver in blue module and flow solver in red module.

3.2 Governing Equations

As shown in Figure 8, the computational domain containing N particles and a Newtonian fluid is denoted by Ω, its outer boundary by Γ, the interior space of the i-th particle by P_i (i = 1, …, N), and the interface between the particle and the fluid by ∂P.

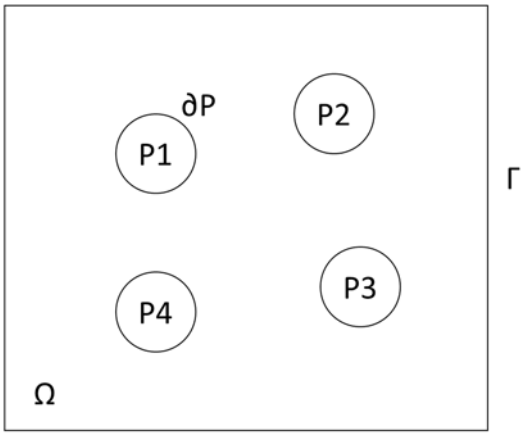

Figure 8. A typical computational domain.

The motion of a Newtonian fluid mixture is governed by:

$$\rho_m \frac{\partial \vec{u}}{\partial t} + (\vec{u} \cdot \nabla)\vec{u} = \rho_m \vec{g} + \nabla \cdot \vec{\vec{\sigma}}^H \qquad in \quad \Omega \setminus P(t) \ , \tag{39}$$

$$\nabla \cdot \vec{u} = 0 \qquad in \quad \Omega \setminus P(t) \ , \tag{40}$$

$$\vec{u} = \vec{u}_\Gamma \qquad on \quad \Gamma \ , \tag{41}$$

$$\vec{u} = \vec{U}_i + \vec{\omega}_i \times \vec{r}_i \qquad on \quad \partial P_i(t), i = 1, ..., N \quad \text{and} \tag{42}$$

$$\vec{u}\big|_{t=0} = \vec{u}_0 \qquad in \quad \Omega \setminus P(0) \ . \tag{43}$$

Here $\vec{u}$ is the fluid velocity, ρ_m the fluid density, $\vec{g}$ the gravitational force, $\vec{U}_i$ and $\vec{\omega}_i$ the translational and angular velocities of the *i*-th particle; the Cauchy stress tensor is $\vec{\vec{\sigma}}^H = -p\vec{\vec{I}} + 2\mu\vec{\vec{D}}[\vec{u}]$, where p is the fluid pressure, μ the fluid viscosity, and the rate-of-strain tensor $\vec{\vec{D}}[\vec{u}] = \frac{1}{2}\left[\nabla\vec{u} + (\nabla\vec{u})^T\right]$.

The particles experience a variety of external forces as they travel in the surrounding fluid. The motion of the *i*-th particle is governed by

$$m_i \frac{d\vec{U}_i}{dt} = m_i \vec{g} + \vec{F}_i \ , \tag{44}$$

$$I_i \frac{d\vec{\omega}_i}{dt} = \vec{T}_i \ , \tag{45}$$

$$\vec{U}_i\big|_{t=0} = \vec{U}_{i,0} \quad \text{and} \tag{46}$$

$$\omega_i\big|_{t=0} = \omega_{i,0} \ , \tag{47}$$

where m_i and I_i are the mass and moment of inertia of the *i*-th particle, respectively; $\vec{F}_i$ and $\vec{T}_i$ are the hydrodynamic force and torque on the *i*-th particle, which include contributions from both the Cauchy stress tensor (due to the viscous flow) and the Maxwell stress tensor (due to the dielectrophoretic force)

$$\vec{F}_i = \int\limits_{\partial P_i(t)} \left(\ddot{\sigma}^H + \ddot{\sigma}^M \right) \cdot \hat{n} \, dA \ \text{ and} \tag{48}$$

$$\vec{T}_i = \int\limits_{\partial P_i(t)} \vec{r}_i \times \left[\left(\ddot{\sigma}^H + \ddot{\sigma}^M \right) \cdot \hat{n} \right] dA \ , \tag{49}$$

where $\hat{n}$ is the unit normal vector pointing out of the particle.

In addition, the following kinematic equations must be satisfied

$$\frac{d\vec{X}_i}{dt} = \vec{U}_i \ , \tag{50}$$

$$\frac{d\Theta_i}{dt} = \omega_i \ , \tag{51}$$

$$\vec{X}_i\big|_{t=0} = \vec{X}_{i,0} \ \text{ and} \tag{52}$$

$$\Theta_i\big|_{t=0} = \Theta_{i,0} \ , \tag{53}$$

where $\vec{X}_i$ and Θ_i are the center of mass and the angular orientation of the *i*-th particle, respectively.

3.3 Direct Numerical Simulation

3.3.1 Distributed Lagrange Multiplier

The distributed Lagrange multiplier/fictitious domain (DLM/FD) method is used to solve the coupled fluid-particle interactions [95]. One of the advantages of this method is that the fluid and particle equations are integrated into one weak equation of motion, i.e., the total momentum equation or the combined equation of motion, thereby eliminating the need to calculate the hydrodynamic forces and torques on the particles explicitly. This is implemented through the DLM, which enforces the rigid-body motion in the particle interiors and on the boundary of each particle. By this means, the DLM acts as an additional body force inside the boundary of the particle to maintain the rigid-body motion and is analogous to the pressure in incompressible fluid flow, whose gradient is the force maintaining the constraint of incompressibility. The full details of the DLM/FD method can be found in [84], and only the key components are briefly reviewed here.

The key to derive the combined equation of motion is the combined velocity space

$$\begin{aligned} \vec{V}_{u_\Gamma}(t) = \{(\vec{v},\vec{V},\vec{\xi}) \big| \vec{v} \in H^1(\Omega \setminus \overline{P(t)})^2, \vec{V} \in R^2, \vec{\xi} \in R, \\ \vec{v} = \vec{V} + \vec{\xi} \times \vec{r} \text{ on } \partial P(t), \text{and } \vec{v} = \vec{u}_\Gamma(t) \text{ on } \Gamma\}. \end{aligned} \tag{54}$$

The combined fluid-particle velocity $(\vec{v},\vec{U},\vec{\omega})$ must lie in the combined velocity space, $\vec{V}_{u_\Gamma}(t)$. To derive the combined equation of motion, a combined variation $(\vec{v},\vec{V},\vec{\xi})$ is taken from the combined variation space

$$\begin{aligned} \vec{V}_0(t) = \{(\vec{v},\vec{V},\vec{\xi}) \big| \vec{v} \in H^1(\Omega \setminus \overline{P(t)})^2, \vec{V} \in R^2, \vec{\xi} \in R, \\ \vec{v} = \vec{V} + \vec{\xi} \times \vec{r} \text{ on } \partial P(t), \text{and } \vec{v} = 0 \text{ on } \Gamma\}. \end{aligned} \tag{55}$$

Then, the single weak equation can be stated as

$$\int_{\Omega\setminus\overline{P(t)}} \rho_m \left[\frac{\partial \vec{u}}{\partial t} + (\vec{u}\cdot\nabla)\vec{u} - \vec{g} \right] \cdot \vec{v}\, d\vec{x} + m\left(\frac{d\vec{U}}{dt} - \vec{g} \right) \cdot \vec{V} + I \frac{d\omega}{dt} \xi = \int_{\Omega\setminus\overline{P(t)}} \vec{\sigma} : \vec{D}[\vec{v}]\, d\vec{x}, \quad \textit{for all } (\vec{v},\vec{V},\vec{\xi}) \in \vec{V}_0. \tag{56}$$

Here, both $\vec{u}$ and $\vec{v}$ must satisfy the no-slip boundary conditions

$$\vec{u} = \vec{U} + \vec{\omega} \times \vec{r} \quad \textit{on } \partial P(t) \text{ and} \tag{57}$$

$$\vec{v} = \vec{V} + \vec{\xi} \times \vec{r} \quad \textit{on } \partial P(t)\ . \tag{58}$$

Similarly, the fluid pressure P must lie in the space

$$L_0^2(\Omega \setminus \overline{P(t)}) = \left\{ q \in L^2(\Omega \setminus \overline{P(t)}) \middle| \int_{\Omega\setminus\overline{P(t)}} q\, d\vec{x} = 0 \right\}\ , \tag{59}$$

and the weak formulation of the problem is completed by the weak form of the incompressibility constraint

$$\int_{\Omega\setminus\overline{P(t)}} q \nabla\cdot\vec{u}\, d\vec{x} = 0, \quad \textit{for all } q \in L^2(\Omega \setminus \overline{P(t)})\ . \tag{60}$$

This scheme has two advantages over other methods due to the fact that the hydrodynamic force and torque have been eliminated in the derivation of the combined equation of motion. The first one is that it saves computation time as the force and torque are implicit and need not be computed. More importantly, the scheme is not subject to a numerical instability which arises when the equations of the fluid and particle motion are integrated as a coupled system [96].

3.3.2 Fictitious Domain

Once the combined weak form is obtained, it is necessary to extend the problem from the domain excluding the particles, denoted as $\Omega \setminus \overline{P(t)}$, to the whole domain Ω, while still forcing the solution to satisfy the no-slip condition on $\partial P(t)$. Accordingly, the fictitious domain method is applied to achieve this goal. The idea is to assume that the whole domain is filled with fluid, both inside and outside the particle boundaries. The domain obtained as a result of this is simpler, which enables the use of a more simple regular mesh. Moreover, the extended domain being time-independent allows the use of the same mesh for the entire simulation.

With the fictitious domain method, the constraint of the rigid-body motion is still required to be satisfied on the surface of the particles. In addition, the particle interior requires the rigid-body constraint as well, which is achieved by applying the distributed Lagrange multiplier.

The extension in the fictitious method is implemented in two steps. Firstly, the weak equation is extended from $\Omega \setminus \overline{P(t)}$ to the whole of Ω, by obtaining an analogous equation of motion for $P(t)$. The second step is to relax the constraint of the rigid-body motion by removing it from the combined velocity spaces and enforcing it as a side constraint using a Lagrange multiplier.

In order to obtain a combined equation of motion in the first step, it is necessary to enforce the constraint of rigid-body motion for both $\vec{u}$ and $\vec{v}$ throughout $P(t)$. So it requires that

$$\vec{u} = \vec{U} + \vec{\omega} \times \vec{r} \quad in\ P(t) \ \text{ and} \tag{61}$$

$$\vec{v} = \vec{V} + \vec{\xi} \times \vec{r} \quad in\ P(t)\ . \tag{62}$$

The weak equation in the fictitious domain can be stated as

$$\begin{aligned} &\int_{P(t)} \rho_m \left[\frac{\partial \vec{u}}{\partial t} + (\vec{u} \cdot \nabla)\vec{u} - \vec{g} \right] \cdot \vec{v}\, d\vec{x} - \frac{\rho_m}{\rho_d} m \left(\frac{d\vec{U}}{dt} - \vec{g} \right) \cdot \vec{V} - \frac{\rho_m}{\rho_d} I \frac{d\vec{\omega}}{dt} \cdot \vec{\xi} \\ &\quad = \int_{P(t)} \vec{\sigma} : \vec{D}[\vec{v}]\, d\vec{x}. \end{aligned} \tag{63}$$

To obtain the combined weak equation of motion for the entire domain Ω, the combined velocity and combined variation spaces are extended to $P(t)$ by using the extended rigid-body motion constraint Eq. (62)

$$\begin{aligned} \tilde{\tilde{V}}_{u_\Gamma}(t) = \{ (\vec{v}, \vec{V}, \vec{\xi}) \,\big|\, &\vec{v} \in H^1(\Omega)^2, \vec{V} \in R^2, \vec{\xi} \in R, \\ &\vec{v} = \vec{V} + \vec{\xi} \times \vec{r}\ in\ P(t),\ and\ \vec{v} = \vec{u}_\Gamma(t)\ on\ \Gamma \}, \end{aligned} \quad \text{and} \tag{64}$$

$$\begin{aligned} \tilde{\tilde{V}}_0(t) = \{ (\vec{v}, \vec{V}, \vec{\xi}) \,\big|\, &\vec{v} \in H^1(\Omega)^2, \vec{V} \in R^2, \vec{\xi} \in R, \\ &\vec{v} = \vec{V} + \vec{\xi} \times \vec{r}\ in\ P(t),\ and\ \vec{v} = 0\ on\ \Gamma \}. \end{aligned} \tag{65}$$

The extended fluid-particle velocity $(\vec{v}, \vec{U}, \vec{\omega})$ must lie in $\tilde{\tilde{V}}_{u_\Gamma}(t)$. Hence, the combined weak equation of motion for the entire domain Ω can be obtained as

$$\begin{aligned} &\int_\Omega \rho_m \left[\frac{\partial \vec{u}}{\partial t} + (\vec{u} \cdot \nabla)\vec{u} - \vec{g} \right] \cdot \vec{v}\, d\vec{x} + \left(1 - \frac{\rho_m}{\rho_d} \right) \left(m \left(\frac{d\vec{U}}{dt} - \vec{g} \right) \cdot \vec{V} + I \frac{d\vec{\omega}}{dt} \cdot \vec{\xi} \right) \\ &\quad = \int_\Omega \vec{\sigma} : \vec{D}[\vec{v}]\, d\vec{x}, \quad for\ all\ (\vec{v}, \vec{V}, \vec{\xi}) \in \tilde{\tilde{V}}_0. \end{aligned} \tag{66}$$

The second step is to relax the constraint of rigid-body motion. In Eq. (66), the solution function $\vec{u}$ and variation $\vec{v}$ are required to satisfy the constraint of rigid-body motion throughout $P(t)$. This constraint can be relaxed by removing it from the combined velocity spaces, enforcing it as a side constraint in the weak sense and adding an appropriate distributed Lagrange multiplier term to the right hand side of the equation. This results in the following weak formulation of the problem in the extended domain: Find $\vec{u} \in \vec{W}_{u_\Gamma}$, $p \in L_0^2(\Omega), \lambda \in \Lambda(t), \vec{U} \in R^2$ and $\vec{\omega} \in R$ that satisfy

$$\begin{aligned} &\int_\Omega \rho_m \left[\frac{\partial \vec{u}}{\partial t} + (\vec{u} \cdot \nabla)\vec{u} - \vec{g} \right] \cdot \vec{v}\, d\vec{x} + \int_\Omega p \nabla \cdot \vec{v}\, d\vec{x} + \int_\Omega 2\eta \vec{D}[\vec{u}] : \vec{D}[\vec{v}]\, d\vec{x} \\ &\quad + \left(1 - \frac{\rho_m}{\rho_d} \right) \left(m \left(\frac{d\vec{U}}{dt} - \vec{g} \right) \cdot \vec{V} + I \frac{d\vec{\omega}}{dt} \cdot \vec{\xi} \right) \\ &\quad = \left\langle \lambda, \vec{v} - \left(\vec{V} + \vec{\xi} \times \vec{r} \right) \right\rangle_{P(t)}, \quad \textit{for all } \vec{v} \in \vec{W}_0, \vec{V} \in R^2, \vec{\xi} \in R, \end{aligned} \tag{67}$$

$$\int_\Omega q \nabla \cdot \vec{u}\, d\vec{x} = 0, \quad \textit{for all } q \in L^2(\Omega)\ , \tag{68}$$

$$\left\langle \lambda, \vec{v} - \left(\vec{V} + \vec{\xi} \times \vec{r} \right) \right\rangle_{P(t)} = 0, \quad \textit{for all } \mu \in \Lambda(t) \ \text{ and} \tag{69}$$

$$\vec{u}\big|_{t=0} = \vec{u}_0 \qquad \textit{in} \quad \Omega\ , \tag{70}$$

where $\vec{u}_0$ satisfies the compatibility conditions

$$\nabla \cdot \vec{u} = 0 \qquad \textit{in} \quad \Omega \setminus \overline{P(0)} \ \text{ and} \tag{71}$$

$$\vec{u}_0 = \vec{U}_0 + \vec{\omega}_0 \times \vec{r}_0 \qquad \textit{in} \quad P(0)\ . \tag{72}$$

Here

$$\vec{r}_0 = \vec{x} - \vec{X}(0) \ , \tag{73}$$

$$\vec{W}_{u_\Gamma} = \{\vec{v} \in H^1(\Omega)^2 \,|\, \vec{v} = \vec{u}_\Gamma(t) \ on \ \Gamma\} \ , \tag{74}$$

$$\vec{W}_{u_\Gamma} = H_0^1(\Omega)^2 \ , \tag{75}$$

$$L_0^2(\Omega) = \left\{ q \in L^2(\Omega) \,|\, \int_\Omega q d\vec{x} = 0 \right\} \ , \tag{76}$$

and $\Lambda(t)$ is $H^1(P(t))^2$, with $\langle \cdot, \cdot \rangle_{P(t)}$ denoting an appropriate inner product.

3.4 Computational Scheme

The computational scheme used in this work is a generalization of the DLM finite element scheme [95, 97]. As the problem consists of unsteady flow due to the motion of the particles, it must be analyzed in two aspects: space and time. The DLM and regular finite element method are employed for space discretization. For time discretization, an operator slitting scheme is adopted.

3.4.1 Space Discretization

In this section, the fluid flow equations are solved in the combined fluid-solid domain, and the motion in particle interiors is enforced to be the rigid-body motion using a DLM. The fluid and particle equations of motion are combined into a single weak equation, which helps improving the stability of the time integration.

The solution and variation are required to satisfy the strong forms, which are the governing equations of the constraint of rigid body motion in $P(t)$ [84, 98]. The constraint

is relaxed from the velocity space and enforced weakly as a side constraint using a DLM. Hence, the following weak equations hold in the extended domain.

Find $\vec{u} \in \vec{W}_{u_\Gamma}$, $p \in L_0^2(\Omega), \lambda \in \Lambda(t), \vec{U} \in R^2$ and $\vec{\omega} \in R^2$ that satisfy not only the kinematic equations and initial conditions but also

$$\begin{aligned} &\int_\Omega \rho_m \left[\frac{\partial \vec{u}}{\partial t} + (\vec{u} \cdot \nabla)\vec{u} - \vec{g} \right] \cdot \vec{v}\, dx - \int_\Omega p \nabla \cdot \vec{v} dx + \int_\Omega 2\eta \vec{D}[\vec{u}] : \vec{D}[\vec{v}] dx \\ &\quad + \left(1 - \frac{\rho_m}{\rho_d} \right) \left[m \left(\frac{d\vec{U}}{dt} - \vec{g} \right) \cdot \vec{V} + I \frac{d\vec{\omega}}{dt} \vec{\xi} \right] - \vec{F}' \cdot \vec{V} \\ &\quad = \left\langle \vec{\lambda}, \vec{v} - \left(\vec{V} + \vec{\xi} \times \vec{r} \right) \right\rangle_{P(t)} \qquad \textit{for all } \vec{v} \in \vec{W}_{0,h}, \vec{V} \in R^2, \vec{\xi} \in R, \end{aligned} \tag{77}$$

$$\int_\Omega q \nabla \cdot \vec{u}\, d\vec{x} = 0, \quad \textit{for all } q \in L^2(\Omega), \tag{78}$$

$$\left\langle \mu, \vec{u} - \left(\vec{U} + \vec{\omega} \times \vec{r} \right) \right\rangle_{P(t)} = 0, \quad \textit{for all } \mu \in \Lambda(t), \text{ and} \tag{79}$$

$$\vec{u}\big|_{t=0} = \vec{u}_0 \qquad \textit{in} \quad \Omega\ . \tag{80}$$

Here $\vec{F}'$ is the additional body force used to limit the extent of overlap, λ the distributed Lagrange multiplier, $\langle \cdot, \cdot \rangle_{P(t)}$ the L^2 inner product over the particle, i.e.,

$$\left\langle \vec{\mu}, \vec{v} \right\rangle_{P(t)} = \int_\Omega q(\vec{\mu}, \vec{v})\, d\vec{x}\ . \tag{81}$$

To solve the above equations numerically, the domain is discretized using a regular finite element triangulation mesh T_h for $\vec{u}$, where h is the mesh size, and a regular twice coarser triangulation T_{2h} for p. Then, the following finite dimensional spaces approximating $\vec{W}_{u_\Gamma}, \vec{W}_0, L^2(\Omega), L_0^2(\Omega)$ can be defined as

$$\vec{W}_{u_\Gamma} = \{\vec{v}_h \in C^0(\Omega)^2 \,|\, \vec{v}_h|_T \in P_1 \times P_1 \ \textit{for all}\ T \in \mathrm{T}_h, \vec{v}_h = \vec{u}_{\Gamma,h}\ \textit{on}\ \Gamma\}\ , \tag{82}$$

$$\vec{W}_{u_\Gamma} = \{\vec{v}_h \in C^0(\Omega)^2 \,|\, \vec{v}_h|_T \in P_1 \times P_1 \ \textit{for all}\ T \in \mathrm{T}_h, \vec{v}_h = 0\ \textit{on}\ \Gamma\}\ , \tag{83}$$

$$L_h^2 = \{q_h \in C^0(\Omega) | q_h|_T \in P_1 \ \textit{for all}\ T \in \mathrm{T}_{2h}\} \ \text{ and} \tag{84}$$

$$L_{0,h}^2 = \left\{q_h \in L^2 \,\middle|\, \int_\Omega q_h d\vec{x} = 0\right\}\ . \tag{85}$$

The particle inner product terms in (77) and (79) are obtained using the discrete inner product defined by Glowinski [84]. A coarser triangulation are used to ensure the numerical stability [99]. Here, we choose M points in $\overline{P(t)}$, $\vec{x}_1, \vec{x}_2, ..., \vec{x}_M$, that uniformly cover $\overline{P(t)}$, and define the finite dimensional spaces as

$$\Lambda_h(t) = \left\{\vec{\mu}_h \,\middle|\, \vec{\mu}_h = \sum_{i=1}^{M} \vec{\mu}_{h,i}\delta(\vec{x} - \vec{x}_i),\ \vec{\mu}_h, ..., \vec{\mu}_M \in R^2\right\}\ . \tag{86}$$

By this means, we can use these finite dimensional spaces to discretize Eqs. (77) - (80).

3.4.2 Time Discretization

Most Navier-Stokes solvers are based on operator-splitting algorithm [100-102] in order to enforce the incompressibility condition via a Stokes solver or an L^2-projection method [90, 103]. Eqs. (77) - (80) are systems of partial differential equations coupled through the nonlinear term $(\vec{u} \cdot \nabla)\vec{u}$ and the incompressibility condition $\nabla \cdot \vec{u} = 0$. These equations can be solved by this approach to overcome three primary numerical problems [90]:

1. The incompressibility condition, and the related unknown pressure p_h,
2. The advection and diffusion terms,
3. The constraint of rigid-body motion in $p_h(t)$, and the related distributed Lagrange multiplier $\vec{\lambda}_h$.

Each of these corresponds to a specific operator. In this work, the Marchuk operator-splitting scheme [104] is applied to an initial value problem of the form

$$\frac{d\phi}{dt} + A_1(\phi) + A_2(\phi) + A_3(\phi) = f \quad \text{and} \tag{87}$$

$$\phi(0) = \phi_0 \ , \tag{88}$$

where the operators A_1, A_2, A_3 can be multiple-valued.

Although this approach is only first-order accurate, it is compensated by good stability and robustness properties. If Δt denotes the time step and $\vec{u}^{\,0} = \vec{u}_{0,h}, \vec{U}^{\,0} = \vec{U}_0, \vec{X}^{\,0} = \vec{X}_0, \vec{\omega}^{\,0} = \vec{\omega}_0.$, and assume $\vec{u}^{\,n}, \vec{U}^{\,n}, \vec{X}^{\,n}$ and $\vec{\omega}^{\,n}$ are known (n = 0, 1, 2, 3, …), the (n+1) time step can be solved in the following steps.

Step 1, find $\vec{u}^{\,n+1/3} \in \vec{W}^{\,n+1}_{u_\Gamma,h}$ and $p^{n+1/3} \in L^2_{0,h}$ satisfying

$$\begin{aligned} &\int_\Omega \rho_m \frac{\vec{u}^{\,n+1/3} - \vec{u}^{\,n}}{\Delta t} \cdot \vec{v}\, d\vec{x} - \int_\Omega p^{n+1/3} \nabla \cdot \vec{v}\, d\vec{x} \\ &\quad + \alpha \int_\Omega 2\eta \vec{D}[\vec{u}^{\,n+1/3}] : \vec{D}[\vec{v}]\, d\vec{x} = 0 \quad \textit{for all } \vec{v} \in \vec{W}_{0,h}, \end{aligned} \tag{89}$$

$$\int_\Omega q \nabla \cdot \vec{u}^{\,n+1/4}\, d\vec{x} = 0, \quad \textit{for all } q \in L^2_h \ . \tag{90}$$

Step 2, find $\vec{u}^{n+2/3} \in \vec{W}_{u_\Gamma,h}^{n+1}$ satisfying

$$\int_\Omega \rho_m \frac{\vec{u}^{n+1/3} - \vec{u}^n}{\Delta t} \cdot \vec{v}\, d\vec{x} - \int_\Omega p^{n+1/3} \nabla \cdot \vec{v}\, d\vec{x} + \alpha \int_\Omega 2\eta \vec{D}[\vec{u}^{n+1/3}] : \vec{D}[\vec{v}]\, d\vec{x} = 0 \qquad \text{for all } \vec{v} \in \vec{W}_{0,h}. \tag{91}$$

Step 3, compute $\vec{U}^{n+2/3}$ and $\vec{X}^{n+2/3}$ using the prediction procedure as follows.

Set $\vec{u}^0 = \vec{u}_{0,h}, \vec{U}^0 = \vec{U}_0, \vec{X}^0 = \vec{X}_0, \vec{\omega}^0 = \vec{\omega}_0.$

Do k = 1, K

$$\vec{U}^{*n,k} = \vec{U}^{n,k-1} + \left(\vec{g} + \left(1 - \frac{\rho_m}{\rho_d} \right)^{-1} M^{-1} \vec{F}'(\vec{X}^{n,k-1}) \right) \frac{\Delta t}{K} \tag{92}$$

$$\vec{X}^{*n,k-1} = \vec{X}^{n,k-1} + \left(\frac{U^{n,k} + U^{*n,k}}{2} \right) \frac{\Delta t}{K} \tag{93}$$

$$\vec{U}^{n,k} = \vec{U}^{n,k-1} + \left(\vec{g} + \left(1 - \frac{\rho_m}{\rho_d} \right)^{-1} M^{-1} \frac{\vec{F}'(\vec{X}^{n,k-1}) + \vec{F}'(\vec{X}^{*n,k-1})}{2} \right) \frac{\Delta t}{K} \tag{94}$$

$$\vec{X}^{n,k} = \vec{X}^{n,k-1} + \left(\frac{U^{n,k-1} + U^{n,k}}{2} \right) \frac{\Delta t}{K} \tag{95}$$

End Do

Then, set $\vec{U}^{n+2/3} = \vec{U}^{n,k}$ and $\vec{X}^{n+2/3} = \vec{X}^{n,k}$. Find $\vec{u}^{n+1} \in \vec{W}_{u_\Gamma,h}^{n+1}, \vec{U}^{n+1} \in R^2, \vec{\omega} \in R,$ and $\lambda^{n+1} \in \Lambda_h^{n+2/3}$ satisfying

$$\int_\Omega \rho_m \frac{\vec{u}^{n+1}-\vec{u}^{n+2/3}}{\Delta t}\cdot\vec{v}\,dx$$
$$+\left(1-\frac{\rho_m}{\rho_d}\right)\left[M\frac{\vec{U}^{n+1}-\vec{U}^{n+2/3}}{\Delta t}\cdot\vec{V}+I\frac{\vec{\omega}^{n+1}-\vec{\omega}^{n+2/3}}{\Delta t}\vec{\xi}\right] \tag{96}$$
$$=\left\langle\vec{\lambda}^{n+1},\vec{v}-\left(\vec{V}+\vec{\xi}\times\vec{r}^{\,n+2/3}\right)\right\rangle_{P((n+2/3)\Delta t)}$$
$$\textit{for all } \vec{v}\in\vec{W}_{0,h},\vec{V}\in R^2,\vec{\xi}\in R,$$

$$\left\langle\mu,\vec{u}^{n+1}-\left(\vec{U}^{n+1}+\vec{\omega}^{n+1}\times\vec{r}^{\,n+2/3}\right)\right\rangle_{P_h^{n+2/3}}=0,\quad \textit{for all } \mu\in\Lambda_h^{n+2/3}\ . \tag{97}$$

Then compute $\vec{X}^{n+1}$ with the correction procedure. Set $\vec{X}^{n+1,0}=\vec{X}^{n}$,

Do k = 1, K

$$\vec{X}^{*n+1,k}=\vec{X}^{n+1,k-1}+\left(\frac{\vec{U}^{n}+\vec{U}^{n+1}}{2}\right)\frac{\Delta t}{K} \tag{98}$$

$$\vec{X}^{n,k}=\vec{X}^{*n,k}+\left(1-\frac{\rho_m}{\rho_d}\right)^{-1}M^{-1}\frac{\vec{F}'(\vec{X}^{n+1,k-1})+\vec{F}'(\vec{X}^{*n+1,k-1})}{2}\frac{(\Delta t)^2}{K} \tag{99}$$

End Do

Then set $\vec{X}^{n+1}=\vec{X}^{n+1,k}$.

That is to say, the particle center-of-mass position is predicted in Eqs. (92) - (95) and used in Eqs. (96) and (97). Then the particle center-of-mass position is corrected in Eqs. (98) and (99). Using this operator splitting scheme, we can use a small time step in these prediction and correction procedures. In the current work, we use K=10 in the Eqs. (92) - (95), (98), and (99). Also, in this step, we account for the electric forces that arise due to the dielectrophoretic effect.

3.5 Computational Treatment of Particle Collisions

In order to prevent the particles from penetrating each other or passing over the boundaries of the domain, the following collision strategy is introduced [84]. The particle equation of motion for the *i*-th particle, Eq. (44), is to be replaced by

$$m_i \frac{d\vec{U}_i}{dt} = m_i \vec{g} + \vec{F}_i + \vec{F}_i^{'} \ , \tag{100}$$

where

$$\vec{F}_i^{'} = \sum_{j=1, j\neq i}^{N} \vec{F}_{i,j}^{P} + \sum_{j=1}^{4} \vec{F}_{i,j}^{W} \ . \tag{101}$$

Here $\vec{F}_i^{'}$ is a short-range repulsive force acting on the *i*-th particle by the other particles and by the boundary walls. The particle-particle repulsive force can be expressed as

$$\vec{F}_{i,j}^{P} = \begin{cases} 0, & d_{i,j} \geq R_i + R_j + \rho, \\ \dfrac{1}{\varepsilon_p}\left(\vec{X}_i - \vec{X}_j\right)\left(R_i + R_j + \rho - d_{i,j}\right)^2, & d_{i,j} \leq R_i + R_j + \rho, \end{cases} \tag{102}$$

where $d_{i,j} = \left|\vec{X}_i - \vec{X}_j\right|$ is the distance between the centers of the *i*-th and *j*-th particle, R_i is the radius of the *i*-th particle, ρ is the force range, and ε_p is a small positive stiffness parameter. The particle-wall repulsive force is given by

$$\vec{F}_{i,j}^{P} = \begin{cases} 0, & d_{i,j}^{'} \geq R_i + R_j + \rho, \\ \dfrac{1}{\varepsilon_W}\left(\vec{X}_i - \vec{X}_{i,j}^{'}\right)\left(2R_i + \rho - d_{i,j}^{'}\right)^2, & d_{i,j}^{'} \leq R_i + R_j + \rho, \end{cases} \tag{103}$$

where $d'_{i,j} = \left| \vec{X}_i - \vec{X}_j \right|$ is the distance between the centers of the *i*-th and an imaginary particle $P'_{i,j}$, located on the other side of the boundary as shown in Figure 9 and ε_W is a small positive stiffness parameter.

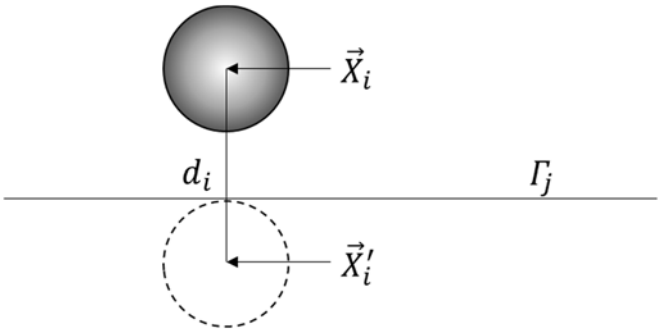

Figure 9. Imaginary particle used for particle-wall repulsion model.

Chapter 4 Directed Self-Assembly of Particles into Chain Lattice Structures

4.1 Introduction

Nanowires and nanotubes, represent the smallest dimension for efficient transport of electrons, are ideal building blocks for hierarchical assembly of functional nanoscale electronic and photonic structures [13, 105, 106], that could overcome fundamental and economic limitations of conventional lithography-based fabrication [107]. Several approaches have been proposed to assemble the nanowires and nanotubes into functional nanostructures and devices, including chemical biding [14], magnetic field directed assembly [108], electro-optical assisted assembly [109] and dielectrophoresis directed self-assembly [65, 110]. Particularly, the electric field directed self-assembly method in aqueous solutions makes it possible to control the structure of the patterns that are to be formed in a convenient and precise manner [110]. While the building blocks, i.e., the nanowires and nanotubes, are traditionally synthesized by chemical or electrochemical means [14, 111, 112], they have been fabricated in recent years by using nanoparticles to enable further scale-down and reconfiguration of the manufacturing process. For instance, it was demonstrated that micro/nanowires can be assembled from individual gold nanoparticles by dielectrophoresis effect [15, 113-116]. In the existing studies, the key underlying physical process is known as "pearl chaining" in the literature of dielectrophoresis, during which the constituent dielectric particles attract to each other and align with the direction of the applied electric field, forming a one-dimensional (1D) chain lattice structure [23, 70, 72, 117].

Pearl chaining process is primarily driven by the attractive DEP force between neighboring particles, which is, however, short-ranged, i.e., it decays rapidly as a function of R^{-4} where R is the inter-particle distance [118]. Therefore, disturbances in the surrounding fluid medium can easily affect the quality and even destabilize the morphological structure of the chain lattice formed. Unfortunately, current understanding of the pearl chaining process is limited to the electrostatic aspect of the particle-particle interactions, whereas the fluid-particle hydrodynamic interactions and their possible impact on the self-assembly of 1D chain lattice have been largely neglected. Hence, there is a significant gap between the present fundamental knowledge of pearl chaining and the future technological development of DEP directed self-assembly of nanoparticles.

To provide the missing piece of knowledge, the DLM/FD method and the MST approach are used together in this chapter to simulate the DEP directed self-assembly of nanoparticles into chain lattice structures in a uniform external electric field. The DEP force and torque acting on the particles are calculated by integrating Maxwell stress tensor over the surface of the each particle. Then, the DLM/FD method is applied to solve the particle-particle and particle-fluid hydrodynamic interactions. In addition, microfluidic experiments are conducted to observe the directed self-assembly process of three model systems consisting of two, three and six microparticles with diameter of 3.2 μm, respectively, under a uniform AC electric field. The numerical simulation results of the trajectory and the final pattern of the particles are compared to the experimental data, and very good agreements have been found.

4.2 Pearl Chaining

To elucidate the key features of pearl chaining, a simple model system consisting of two particles (shown in Figure 10(a)) is firstly analyzed in this work. A pair of spherical particles of radius *a* are marked by their center positions, P1 and P2, respectively. They are placed in a uniform electric field, which is along the horizontal direction (the applied electrostatic potential is $\phi = \phi_1$ on AB and $\phi = \phi_2$ on CD), with an intitial inter-particle distance of R. The angle between the electric field and the line connecting the centers of the two particles is θ. After the electric field is actuated, the two paricles experience DEP particle-particle interaction forces and tend to align with the external field.

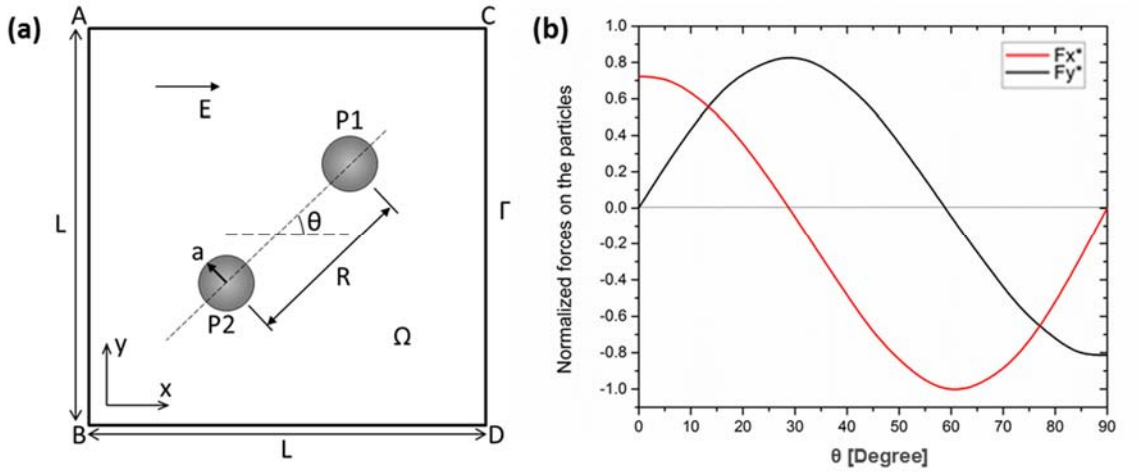

Figure 10. Illustration of the computation domain (a) and force analysis (b).

The particle-particle interaction and the resulting motion of the pair of particles can be analyzed as follows. Here we consider the dielectric interaction and the resulting relative motion of two spherical particles submerged in an electrolyte medium in which a uniform electric field of E is applied. The two particles have the same electric properties and radius a. Application of electric field can raise the temperature of the medium due to

Joule heating, resulting in change of material properties. Here, the material properties are assumed fixed, i.e., without being affected by Joule heating.

To determine the trajectory of the particles, Kang and Li [82] assume that the Stokes drag force counteracts the dielectric force. Then the velocity of a particle is determined by

$$\vec{u} = \vec{F}_E / (6\pi\mu a) \ , \tag{104}$$

where μ is the dynamic viscosity of the fluid and $\vec{F}_E$ is the dielectric force acting on the particle. Yariv [119] proposed an approximation for the dielectric force as an analytical solution for the trajectory

$$\vec{F}_E \cong -\frac{6\pi\varepsilon E_\infty^2 a^2}{(R/a)^4}\left[\hat{\vec{x}}\left(\cos^2\theta - \frac{1}{2}\cos^2\theta\right) + \hat{\vec{y}}\sin\theta\cos\theta\right] , \tag{105}$$

where E_∞ is the applied electric field. $\hat{\vec{x}}$ and $\hat{\vec{y}}$ are the unit vector in x and y direction, respectively. By using the force balance between the dielectric force and the Stokes force, the velocity is obtained in dimensionless form with $R^* = R/a$ as

$$\vec{u}^* \cong -\frac{1}{R^{*4}}\left[\hat{\vec{x}}\left(\cos^2\theta - \frac{1}{2}\cos^2\theta\right) + \hat{\vec{y}}\sin\theta\cos\theta\right] . \tag{106}$$

Accordingly, we can obtain the motion equations in a (R, θ) polar coordinate system:

$$\frac{dR^*}{dt^*} = -\frac{2\cos^2\theta - \sin^2\theta}{R^{*4}} \quad \text{and} \tag{107}$$

$$\frac{d\theta^*}{dt^*} = -\frac{2\sin\theta\cos\theta}{R^{*5}} \quad . \tag{108}$$

From Eq. (107), it is obvious that the sign (direction) of the force will be changed at θ = 63.4°, at which the right-hand side becomes zero. According to Eq. (108), the dielectric force always tends to align the particles in parallel direction to the electric field. For example, if we consider the range $0 \le \theta \le \pi/2$, the right-hand side of Eq. (108) is always negative. That is, the angle θ is always decreasing to zero. It means that the stable configuration is formed only when the particles are in the parallel orientation.

To better understand the particle motion during pearl chaining, the DEP forces on the particles can be derived using the MST method. Due to symmetry considerations, the two particle experience DEP forces with the same magnitude but of opposite directions. Figure 10(b) illustrates the x- and y-components of the DEP force on particle P2 (normalized by the maximum force experienced) with respect to their relative orientations, i.e., as a function of θ. Clearly, a positive value indicates an attractive force whereas a negative value corresponds to a repulsive force. When $\theta = 0°$, the centerline connecting the particles is aligned with the field direction, $F_x^* = 0.7$ and $F_y^* = 0$. Thus, the two particles only experience attractive forces in the *x* direction and tend to move towards each other. Consequently, the equilibrium configuration for this two-particle system will be two touching particles with their centerline lying along the x-direction. When θ deviates slightly from the equilibrium value, e.g., $0° < \theta < 28°$, both force components are positive, suggesting that the field tends to bring the particles back to the equilibrium positions. When θ falls in the interval of $28° < \theta < 63.4°$, F_x^* becomes negative, which will push the

two particles away from each other in x direction; however, the positive force F_y^* will pull the particles closer along the y direction, thereby offseting the effect of F_x^* and decreasing θ. Hence, the particles will eventually be attracted to each other. As θ futher increases to over 63.4°, $F_x^* < 0$ and $F_y^* < 0$, the particles are repelled from each other in both x and y directions. This critical angle $\theta = 63.4°$ is also verified theoretically by Kang [82] as the threshold to distinguish the attraction and repulsion zones. If the two particles are released from an initial orientation, $63.4° < \theta < 90°$, F_x^* and F_y^* are both negative, but F_x^* is always greater than F_y^* in magnitude. Accordingly, the repulsive DEP forces will cause them to rotate outward orbitally with respect to the middle point between the centers of the particles. At $\theta = 90°$, which indicates a perpendicular orietation to the external electric field, the induced particle-particle interaction force F_y^* is repulsive while the force in x direction is $F_x^* = 0$. Under such circumstance, the particles keep pushing each other away unless they are stopped by other external forces. In reality, two particles can not maintain the angle at exactly $\theta = 90°$ due to the inevitable Bownian motion of the particles. Therefore, the DEP particle-particle interaction forces always tend to attract and align particles in a chain parallel to the applied electric field.

Figure 11(a) shows an electric field when two particles are positioned close to each other. The most intensified field occurs in the gap between the two particles because the electric permittivity of the particle is greater than the fluid. Under such circumstance, particles tend to move to stronger electric field region. Also, it is obvious that the local electric field in the vicinity of each particle is distorted by the other particle.

Based on the local electric field, Maxwell stress tensor is calculated on the surface of the particles and shown in Figure 11(b). Forces and torques are obtained by integrating the MST over the surface of the particles. The particles motion induced fluid flow is shown in Figure 11(c) including the flow vector field and the pressure contour.

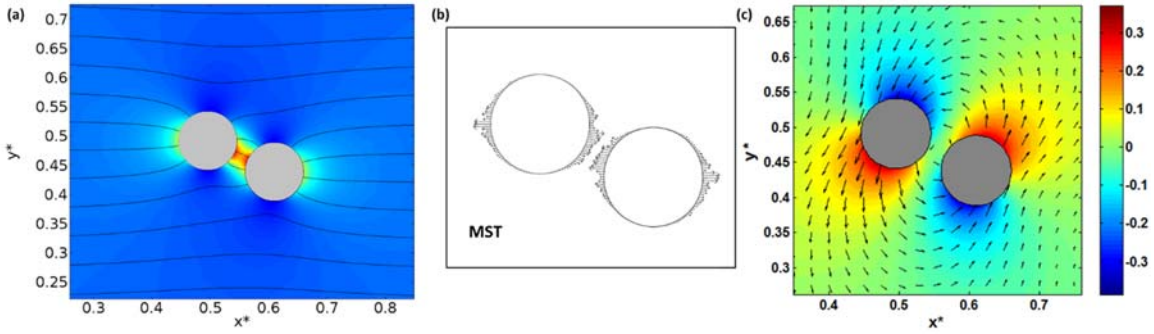

Figure 11. The electric field intensity (a), MST (b), and fluid pressure/velocity field (c).

4.2.1 Particle-Fluid Interactions

The fluid-particle hydrodynamic interactions have been discussed in details in Chapter 2, and will not be repeated here for the sake of brevity. In the numerical simulation work of this chapter, no-slip boundary conditions are applied on the walls AC and BD in Figure 10(a), and periodic boundary conditions on AB and CD.

4.2.2 Brownian Motion

Brownian motion is the random motion of small colloidal particles suspended in a liquid or gas medium, caused by collisions between these particles and the medium's molecules with the particles. Even at room temperature, the effect of Brownian motion of nanoparticles on DEP-directed self-assembly may not be neglected. The importance of Brownian motion with respect to the DEP motion can be evaluated by the Péclet number

$$Pe = \frac{aU}{D_f}, \tag{109}$$

where a, U, D_f are the particle radius, particle velocity due to DEP and the diffusion coefficient, respectively [120]. The physical significance of the Péclet number can be revealed by rewriting Eq. (109) as

$$Pe = \frac{aU}{D_f} = \frac{a^2 / D_f}{a / U} = \frac{t_{diff}}{t_{DEP}}. \tag{110}$$

Therefore, the Péclet number can be interpreted as the ratio of time that is needed for the particle to travel a distance of a due to Brownian motion and DEP, respectively. When Pe >> 1, the effect of Brownian motion can be safely neglected; otherwise, it must be taken into consideration in the DEP-directed self-assembly process.

The DEP velocity of the particle can be obtained from

$$U = \frac{F_{DEP}}{6\pi\mu a}, \tag{111}$$

where F_{DEP} is the DEP force and μ is the fluid viscosity. In the case of two spherical particles aligned perfectly with the electric field, the DEP force can be estimated as [82]

$$F_{DEP} = \frac{3\pi\varepsilon_f E^2 a^2}{\left(R/a\right)^4}, \tag{112}$$

where ε_f and E are the dielectric permittivity of the fluid and the electric field strength.

The diffusion coefficient of the particle is expressed as [120]

$$D_f = \frac{KT}{3\pi\mu a} \ , \tag{113}$$

where K and T are the Boltzmann constant and the temperature, respectively.

Accordingly, the Péclet number can be recast as [66]

$$Pe = \frac{3\pi\varepsilon_f E^2 a^3}{2KT(R/a)^4} \ . \tag{114}$$

As an example, for E = 10 kV/m, a = 3.2 μm, $\varepsilon_f = 7.09 \times 10^{-10}$ F/m, and T = 300 K, if two particles are located at a distance of R = 4a, the corresponding Péclet number is 10.3; if R increases to 7.17a, then Pe ≈ 1. Therefore, the Brownian motion must be considered during the early stage of DE-directed self-assembly when the inter-particle distance is relatively large.

4.2.3 Numerical Simulation

Numerical simulations are conducted to compute the trajectories of multiple particles during the DEP-directed fluidic self-assembly. The computation domain is shown in Figure 10(a), where the dimensionless width of the square domain is L = 1, and the dimensionless radius of the particle is a = 0.05. In the simulations, 65536 nodes are used to discretize the domain and 475 nodes are used for each particle. The time step is chosen to be Δt = 0.001 s. Electric potentials are applied to the boundaries AB and CD as Φ_{AB} = 20 V and Φ_{CD} = 0 V. For fluid flow, no slip boundary conditions are specified for AB and CD. Periodic boundary conditions are assumed on the boundaries AC and BD.

4.3 Experiments

In order to validate the numerical simulation results, an experimental apparatus is designed and constructed to perform DEP-directed fluidic self-assembly of microparticles. The setup illustrated in Figure 12 consists of a microfluidic chip, a fluorescent microscope, and an imaging system.

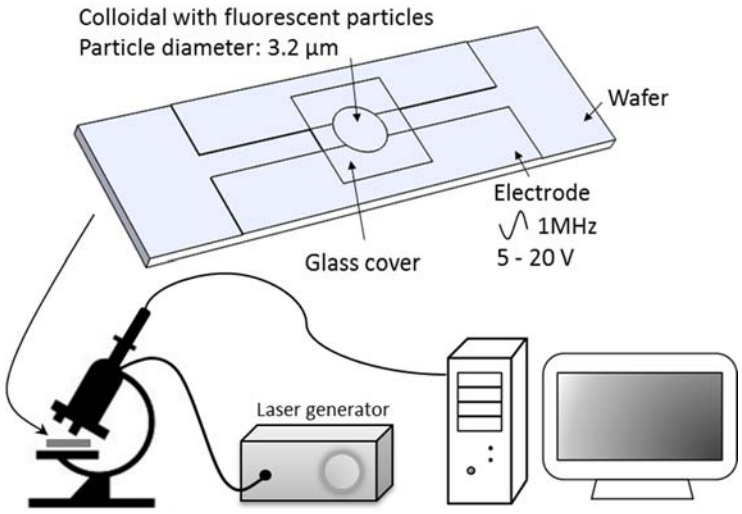

Figure 12. Sketch of experiment setup to observe and record particle motion.

The microfluidic chip consists of an array of two electrodes fabricated using photolithography. With a glass wafer as a substrate, the device is comprised of two layers: the parallel electrodes on the bottom and an isolation layer on the top. At the bottom, a layer of 400 nm copper on top of 100 nm silver layer was deposited with a sputtering system (AJA UHV six-source sputtering system) on a glass wafer. This layer is then deposited with AZ 1512 and photolithography followed by wet-etching. The top layer is comprised of SU-8 layer used as a dielectric layer to protect the metal electrodes from oxidation and corrosion. A layer of 0.6 µm SU-8 is deposited with a spin coater (Brewer

Cee 200 Spin Coater). Then the wafer was baked to make sure its resistance to heat, electricity, or liquid.

The colloidal solution is prepared by mixing fluorescent polystyrene particles of 3.2 μm diameter (Thermo Scientific, CA) with deionized (DI) water. The conductivities of polystyrene and DI water are measured to be 5×10^{-5} S/m and 5.5×10^{-6} S/m; while the relative dielectric permittivity are 2.8 and 78.4, respectively. The colloidal solution contains 0.2 wt% solids, resulting in a mixture density of 1.05 g/cm^3.

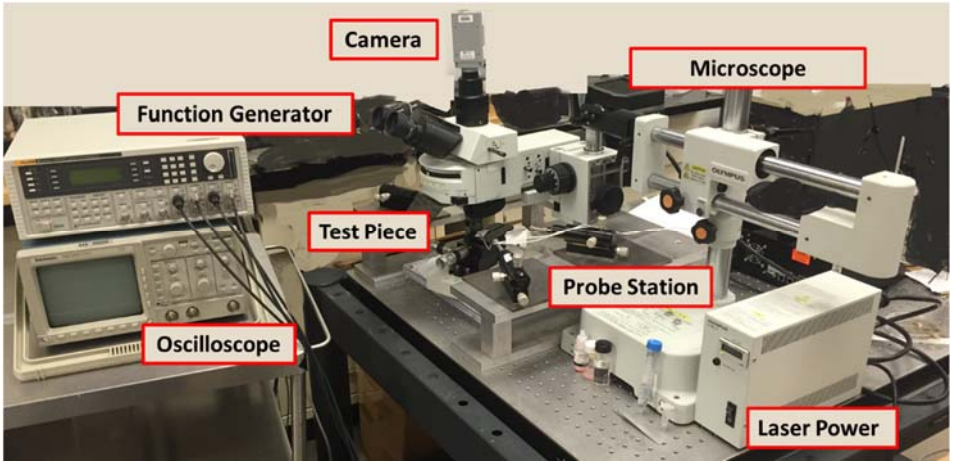

Figure 13. Experiment Setup.

During the experiments, the microfluidic chip is mounted to a probe station, and the electrodes are connected to an AC arbitrary waveform function generator (FLUKE 294), as shown in Figure 13. Sinusoidal wave signals are generated and applied to the electrodes. The applied voltage is 20 V and the frequency is 1 MHz. A digital oscilloscope (Tektronix TDS 310) is used to monitor the voltage, frequency and waveform of the electric signal applied. The particle motion is captured by a CCD camera (PixeLINK PL-B742U) installed on the microscope. An Olympus LMPLFLN 50 × objective lens (N.A. = 0.5,

W.D. = 10.6 mm, F.N. = 26.5 mm) is used for visualization. Positions of the particles will be recorded via the imaging system at a frame rate of 7 frame per second (fps), and an in-house Matlab code is used to extract the stationary images and for further image processing and analysis.

Figure 14(a) shows the initial random distribution of the particles in the colloidal solutions. After the AC electric field (V = 20 V, f = 1 MHz) is switched on, positive DEP occurs, and the particles interact with each other and spontaneously self-assemble into multiple chain lattices along the direction of the electric field. Figure 14(b) shows the ordered chain structures after the field is applied for 30 seconds. This process is reversible, i.e., if the electric field is revoked, the lattices will disassemble and the particles will gradually resume their random distribution under the influence of Brownian motion.

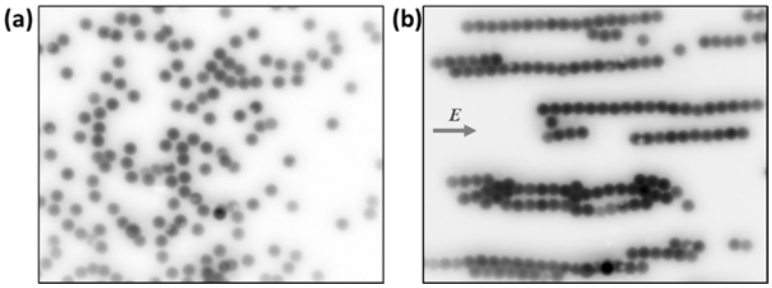

Figure 14. Images of the aqueous suspension captured at (a) t=0s and (b) t=30s.

4.4 Results and Discussion

In this section, the numerical and experimental results will be presented for DEP-directed self-assembly of two, three and six polystyrene particles suspended in DI water, respectively. Both the patterns and the trajectories of the particles will be compared and discussed.

4.4.1 Directed Assembly of Two Particles

For the experiments, two particles, which are at sufficient distance from all the surrounding particles, have been carefully selected to ensure that they are isolated from the hydrodynamic and electrical interactions with their closest neighbors. In Figure 15(a), the initial positions of the two particles are (24.85, 37.33) and (52.48, 19.28) in terms of pixels. This indicates the initial angle between the line connecting the centers of the particles and the electric field is about $\theta = 33.17°$. According to the forgoing analysis in Section 4.2, these two particles experience a repulsive force in the x direction and an attractive force in the y direction. To examine the subsequent motion of the partiecles, their trajectories are illustrated in Figure 16, where both the measured instaneous particle locations and the simulated trajectories are shown as circles and dash lines, respectively. It can be seen that the two particles are at first pushed out in the x direction but pulled toward the equilibrium positions in the y direction. As θ decreases, both x- and y-direction DEP force components become attractive (see Figure 10). Hence, the two particles will eventually move towarch each other, as evidenced by the image sequences after t = 0.43 s in Figure 15. From the comparison in Figure 16, it can be concluded that the particle trajectories obtained from from the numerical simulations agree fairly well with the experimental measurements.

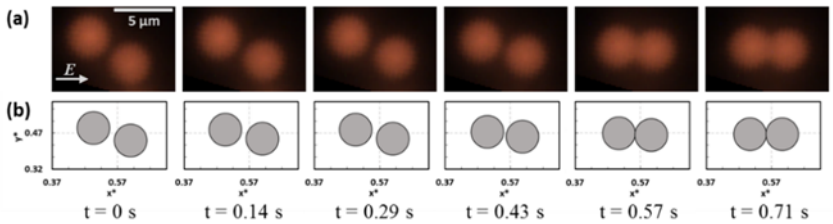

Figure 15. Experimental (a) and Numerical (b) results of DEP assembly of two particles.

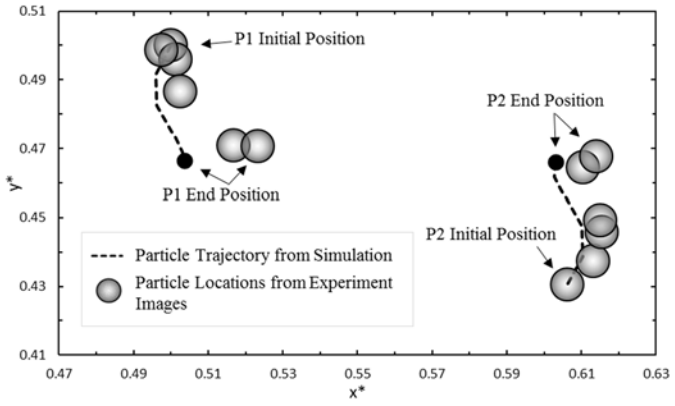

Figure 16. Comparison of trajectories of two particles from experiments and simulation.

4.4.2 Directed Assembly of Three Particles

Similarly to the case of two particles, DEP-directed self-assembly of three particles is also investigated to validate the numerical models. As shown in Figure 17(a), at t = 0 s, three particles (P1, P2 and P3) are located at (15.86, 30.26), (58.92, 54.40) and (91.40, 48.14), respectively, from left to right. Since P2 and P3 are closer to each other than P1, the stronger DEP interactions between them leads to a faster assembly process: the two particles P2 and P3 quickly come into contact and form a dumb-bell structure that aligns to the electric field. Afterwards, the P2-P3 conjugate travels slightly to the left while P1 is attracted to it and eventually joins the entity to form a chain lattice. Both the experimental and the numerical simulation results show the self-assembly process accomplishes and the particle chain becomes stable at around t = 0.86 s. The trajectories of the three particles during the assembly process are depicted in Figure 18. A very good agreement can be found between the experimental data and the numerical simulation results.

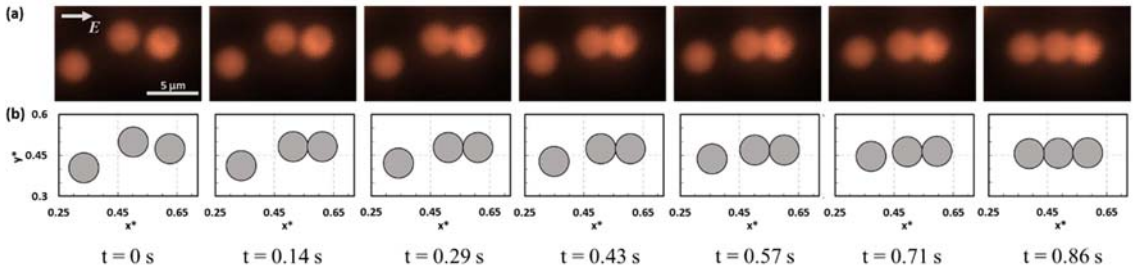

Figure 17. Experimental (a) and Numerical (b) results of DEP assembly of three particles.

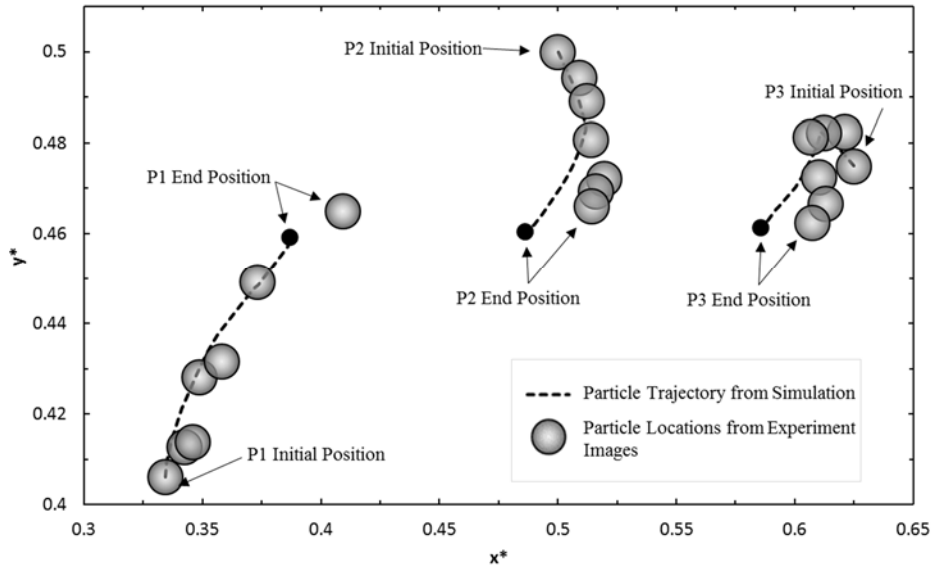

Figure 18. Comparison of trajectories of three particles from experiments and simulation.

4.4.3 Directed Assembly of Six Particles

Figure 19 shows the DEP-directed self-assembly of six particles in DI water. Initially, the particles are located at (28.36, 62.00), (79.18, 60.16), (87.07, 21.02), (115.64, 48.05), (135.04, 29.84) and (155.20, 62.49), from left to right. The particles are named as P1, P2, …, P6, according to the sequence of increasing x value.

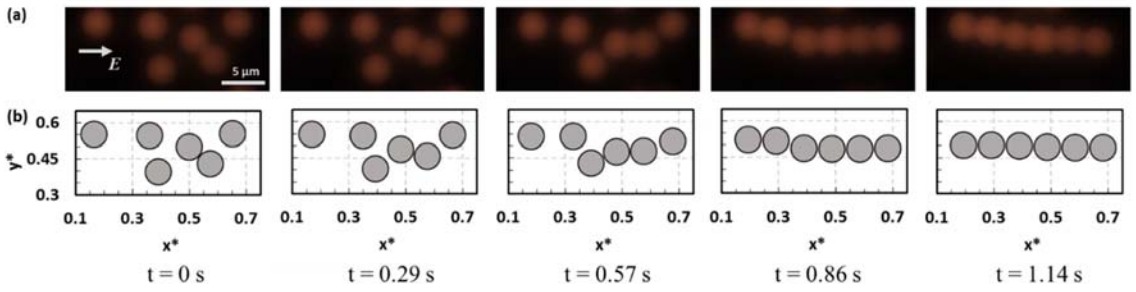

Figure 19. Experimental (a) and Numerical (b) results of DEP assembly of six particles.

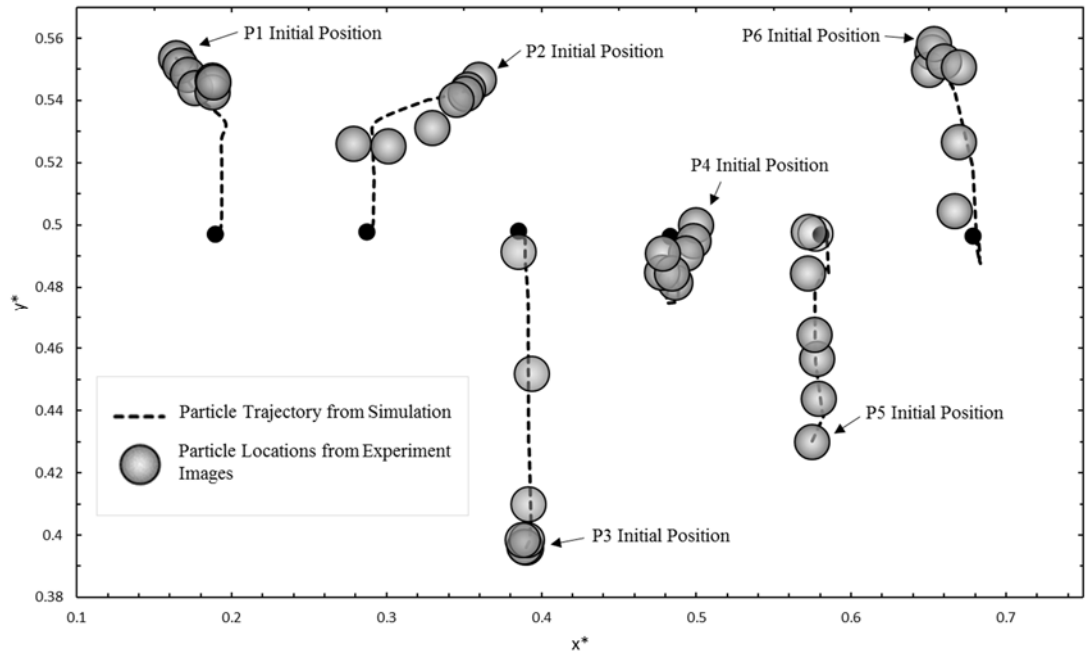

Figure 20. Comparison of trajectories of three particles from experiments and simulation.

Figure 19 shows that, in the initial configuration, particles P4 and P5 have the smallest inter-particle distance compared to all other particles. After the electric field is switched on, P4 and P5 attract to each other instantaneously, giving rise to a dumb-bell entity similar to that in Figure 15. After this two-particle structure is formed, the neighboring particles P3 and P6 will join it and enlarge it into a four-particle chain. This

process then recurs to particles P1 and P2. Finally, at t = 1.14 s, all six particles are lined up into a linear chain in the direction parallel to the external electric field. The trajectories of the six particles during the assembly process are depicted in Figure 20. A very good agreement can be found between the experimental data and the numerical simulation results.

4.5 Conclusions

In this Chapter, the DEP-induced particle-particle interactions are analyzed in details, and it is found that the particles will attract to each other if the relative orientation angle $\theta < 63.4°$, and repel otherwise. Furthermore, DEP-directed self-assembly of multiple particles (two, three and six particles) into linear chain lattices is investigated both experimentally and numerically. The particle-fluid and particle-particle interactions are accurately captured by the numerical simulation with the Distributed Lagrange-multiplier based fictitious-domain method (DLM/FD). Numerical simulations show good agreement with experiments, in terms of both the particle patterns for each time frame and the trajectory of each single particle.

Chapter 5 Traveling-Wave Dielectrophoresis

5.1 Introduction

Dielectrophoresis has been employed extensively as a powerful tool for manipulating particles in biological research, such as in separation [20, 44, 56, 121-126], trapping [21], sorting [22, 34, 52, 127, 128] and translation [23, 129-131] of cells, viruses, proteins and DNA. However, DEP research to date has focused on controlling the electromechanical response of the solid particles, while largely neglecting the hydrodynamic interactions between the particles and the surrounding fluid, *i.e.*, the motion of the surrounding fluid induced by drag from the dielectrophoretic particle motion due to viscous effects. In spite of the advances in colloid science and electromechanics [70, 132, 133], a gap still persists in the application of advances in the science of particle dynamics and low Reynolds-number hydrodynamics to the DEP technique. This gap must be bridged to facilitate the implementation of DEP in a broader range of applications. In particular, the potential of traveling-wave DEP (twDEP) as an effective means for micro/nanoparticle manipulation and microfluidic flow actuation has not yet been explored.

In this Chapter, the fundamentals of twDEP are explored by examining the particle-particle and particle-fluid interactions in colloidal solutions flowing through a microchannel. Numerical methods using the DLM/FD and MST models are employed to probe the particle motion and flow distribution under AC electric fields with various driving frequencies. Model systems consisting one, two and one hundred particles are investigated. In addition, an interdigitated microelectrode array is fabricated on a silicon wafer to generate the four-phase traveling-wave field, and micro-particle image

velocimetry (μPIV) experiments are performed to measure the velocity field produced by twDEP.

5.2 Theory of Traveling-Wave Dielectrophoresis

Figure 21 depicts the cross-section view of the test device for the study of twDEP. A four-phase planar electrode array is fabricated at the bottom surface of the flow channel. The width of the electrodes and the interspacing between neighboring electrodes are $d_1 = d_2 = 40$ μm. The height of the channel is h = 80 μm. The channel is confined by a glass cover at the top, which also acts as an electric insulator.

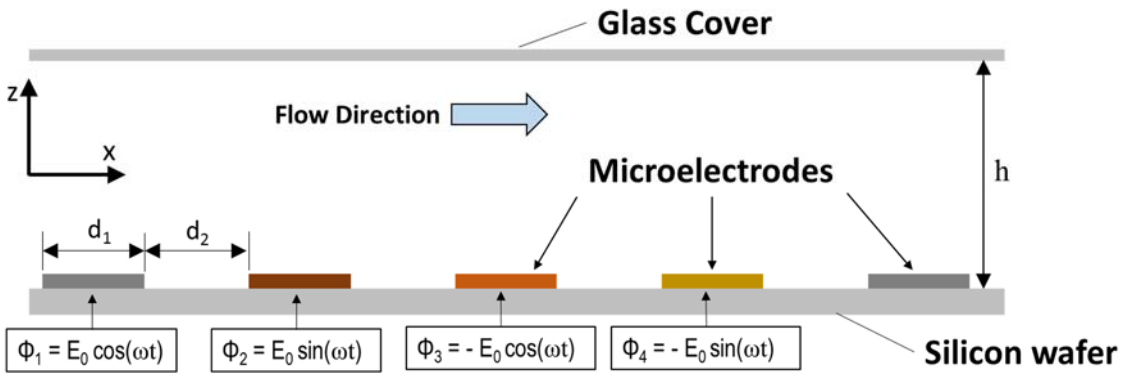

Figure 21. Cross-section view of the microchannel.

The fluid and particles are assumed to be homogeneous linear dielectric materials, so that the electric field in the particle suspension in the flow channel can be solved using Laplace's equation [123]

$$\nabla \cdot \left[\left(\sigma + j\omega\varepsilon \right) \nabla \tilde{\phi} \right] = 0 \ , \tag{115}$$

where the phasor expression of the field is $\tilde{\phi} = \phi_R + j\phi_I$, and the real component ϕ_R and the imaginary component ϕ_I satisfy $\nabla^2\phi_R = 0$ and $\nabla^2\phi_I = 0$, respectively. In the time domain, the electric potential for an AC field of angular frequency ω is given by

$$\phi(\vec{x},t) = \phi_R \cos(\omega t) + \phi_I \sin(\omega t). \tag{116}$$

Specifically, when a four-phase traveling-wave field is applied, the voltages on consecutive electrodes are phase-shifted by 90°, such that $\phi_I(x,y) = \phi_R(x-\lambda/4,y)$, where the wavelength $\lambda = 4(d_1+d_2)$.

Figure 22(a) shows the contour of the real component of the electric potential ϕ_R, and Figure 22(b) shows the imaginary component ϕ_I. It is seen that the electric potential decreases rapidly with increasing distance from the electrodes. Since the density of the field lines is proportional to the strength of the electric field $E = \sqrt{\left|\nabla\phi_R{}^2\right| + \left|\nabla\phi_I{}^2\right|}$, the maxima of the electric field E appears at the edges of the electrodes and decay exponentially with increasing distance from the edges, as shown in Figure 23.

Following the discussions in Chapter 2, the dielectrophoretic force is [70]

$$\vec{F}_{DEP} = 2\pi a^3 \varepsilon_m \left(\mathrm{Re}[f_{CM}]\overline{\nabla}^2 \left|\vec{E}\right|^2 + 2\,\mathrm{Im}[f_{CM}]\left(E_x{}^2\overline{\nabla}\varphi_x + E_y{}^2\overline{\nabla}\varphi_y\right)\right), \tag{117}$$

where Re[f_{CM}] and Im[f_{CM}] denote the real and imaginary parts of f_{CM}, and E_x and E_y are components of the electric field vector; φ_x and φ_y are the phase angles since the electric field is spatially phase-shifted. It is noted that the DEP force depends on the spatial non-uniformities in both the field strength ($\nabla\left|\vec{E}\right|^2$) and the phase ($\nabla\varphi$). In fact, the first term

on the RHS of Eq. (117) determines the alignment of the DEP force with respect to the maxima/minima of the electric field and is the regular DEP force component in DC DEP. The second term on the RHS of Eq. (117) only appears if the electric field has a spatially varying phase, such as in a traveling-wave field, and therefore is the traveling-wave DEP force component. When Im[f_{CM}] is not trivial, the resulting twDEP force in propels the particles along or against the propagating traveling-wave field depending on the sign of Im[f_{CM}]. The twDEP force is generally oriented in parallel to the electrode plane.

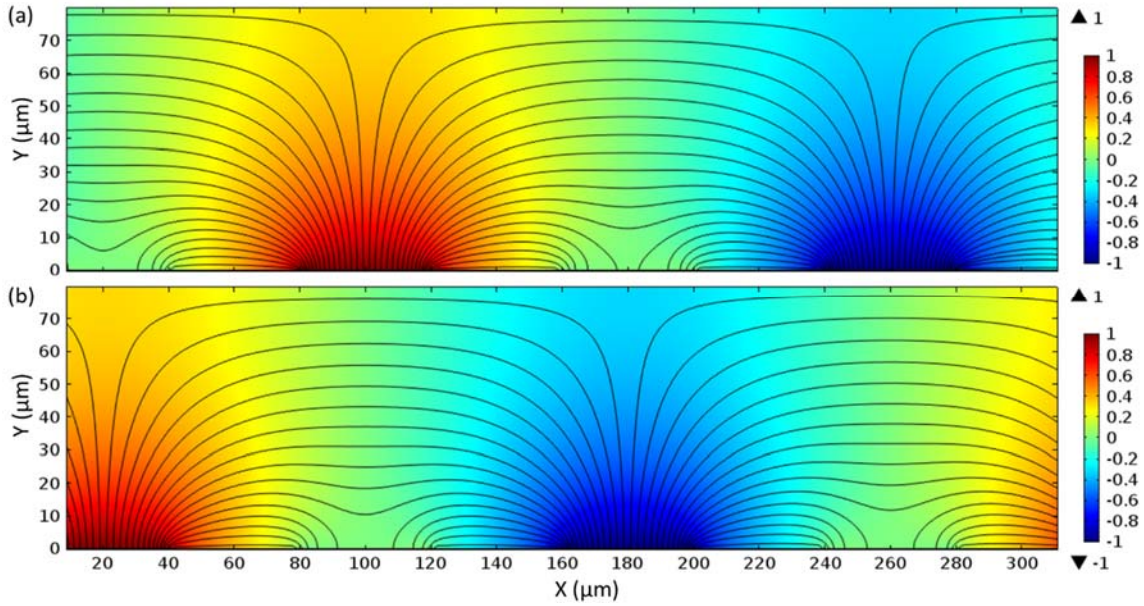

Figure 22. Distribution of the electric potential and field lines (a) ϕ_R and (b) ϕ_I.

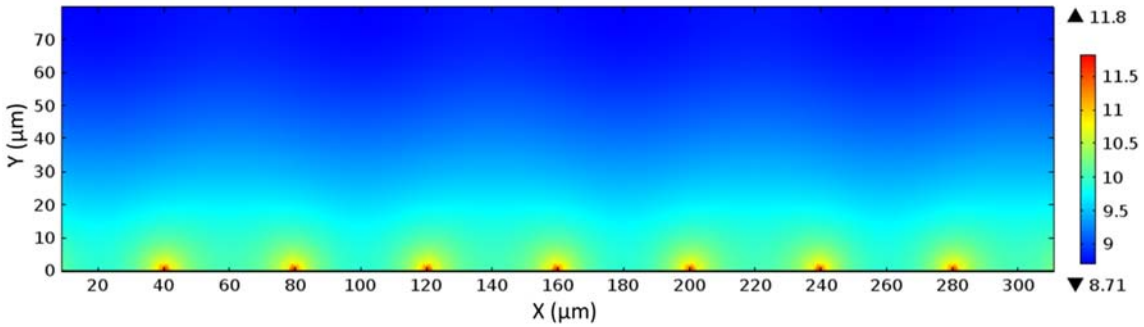

Figure 23. Magnitude of the electric field using logarithmic scale.

The alignment of the twDEP force with the applied field is contingent upon the Clausius-Mossotti factor f_{CM}, which is frequency-dependent. Figure 24 illustrates the real and imaginary parts of f_{CM} as a function of the frequency of the applied field for polystyrene particles suspended in water. Clearly, Re[f_{CM}] is positive in the low-frequency range ($f <$ 1 kHz) in which the particles are more polarizable than the surrounding fluid, and crosses over to negative values as the frequency increases ($f >$ 100 kHz) and the particles become less polarizable than the fluid. If Re[f_{CM}] > 0, the regular DEP force component aligns favorably with the field strength gradient, as indicated by Eq. (117). As a result, the particles move towards the maxima of the electric field, which are usually located at the edges of the electrodes that are used to generate the electric field, and positive DEP occurs. In the opposite situation, a negative Re[f_{CM}] brings negative DEP where the particles move away from the maxima of the electric field, distancing themselves from the electrodes.

The imaginary component of the Clausius-Mossotti factor, f_{CM}, plays an important role in twDEP and electrorotation. Im[f_{CM}] vanishes at both extremes of the frequency spectrum but assumes non-zero values in the mid-range around the cross-over frequency. When Im[f_{CM}] is not trivial, the resulting twDEP force in Eq. (117) propels the particles along or against the propagating traveling-wave field depending on the sign of Im[f_{CM}]. Traveling-wave DEP can be exploited to achieve long-range transport of nanoscale components to desired on-chip sites for assembly. The twDEP force is generally oriented in parallel to the electrode plane. However, in practice, twDEP does not occur in isolation without the companion negative DEP, since the particles must be levitated from the electrode surface. As such, the criteria for effective twDEP are Re[f_{CM}] < 0 and Im[f_{CM}] ≠ 0.

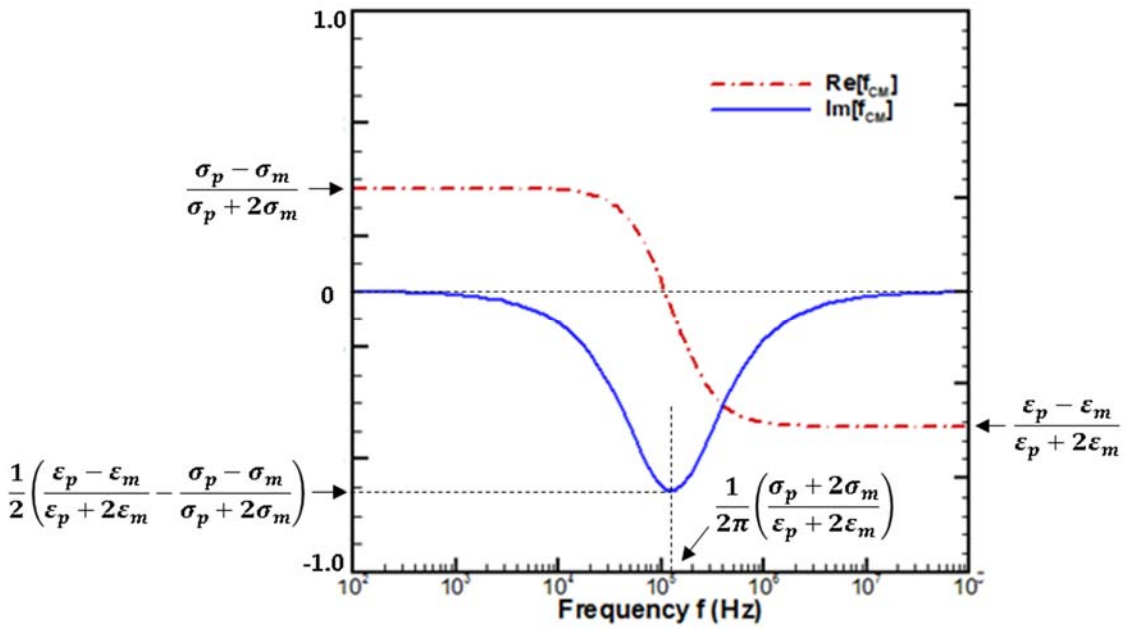

Figure 24. Real and imaginary components of Clausius-Mossotti factor as a function of frequency.

The Re[f_{CM}] and Im[f_{CM}] terms related components of the DEP force at different driving frequencies can be distinguished in Figure 25. It shows the vector fields of the DEP force at (a) low, (b) moderate and (c) high frequency range. Clearly, Figure 25(a) and (c) present the positive DEP and negative DEP, respectively. As shown in the vector plots, the direction of the forces are towards or outwards the electrodes edges, and the magnitude of the force increases exponentially near the edges.

Figure 25(b) represents the twDEP force at the frequency of 10 kHz. At this mid-range frequency, the imaginary part of the Clausius-Mossotti factor dominates. The DEP force in the region at certain height becomes nearly uniform and acts against the propagating traveling wave in the horizontal direction. At a lower height near the edges of the electrodes, the forces are much greater in magnitude and the direction depends on the local electric field. The normalized traveling-wave DEP torque is shown in Figure 26.

The maximum of the torque occurs around the electrodes edges and decays as the height increases. The sign of the torque is positive in most regions. A particle suspending in the fluid under such an electric field is expected to spin counterclockwise around the center of the particle.

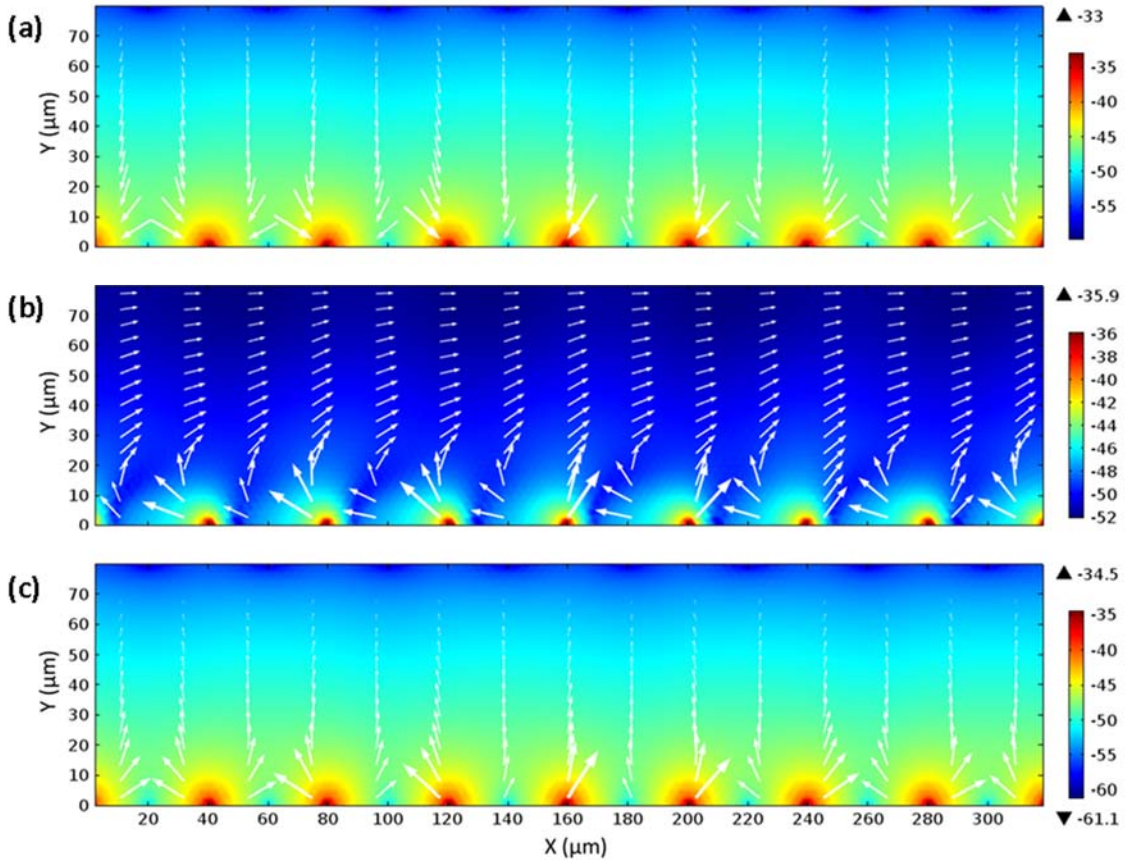

Figure 25. Magnitude of the DEP force at different frequencies using logarithmic scale.

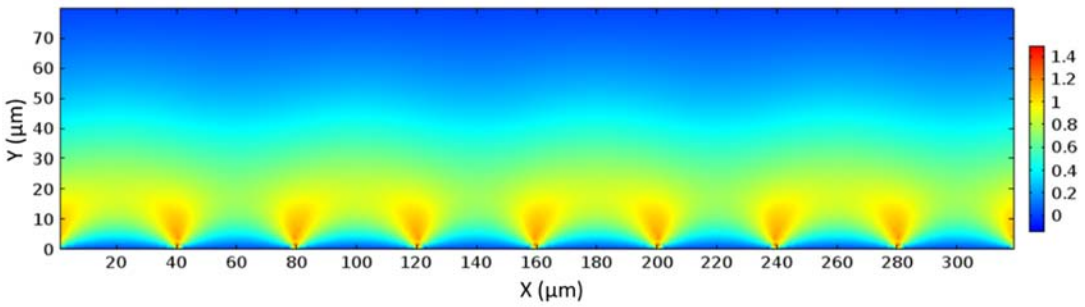

Figure 26. Normalized traveling wave DEP torque.

5.3 Numerical Simulations

In this section, numerical simulations are conducted for model systems consisting of one, two and one hundred particles under various driving frequencies to study their dynamics in twDEP. The case with one hundred particles are analyzed in details in terms of flow patterns and velocity field. The velocity profile along the height of the microchannel from this case will be compared with experimental measurement.

5.3.1 twDEP of a Single Particle

First, the motion of a single particle undergoing twDEP is simulated. The computational domain is shown in Figure 27 where the coordinates are normalized with respect to the channel height, i.e., x* = x/h and y* = y/h. Hence, the dimensionless domain size is 4 in width by 1 in height.

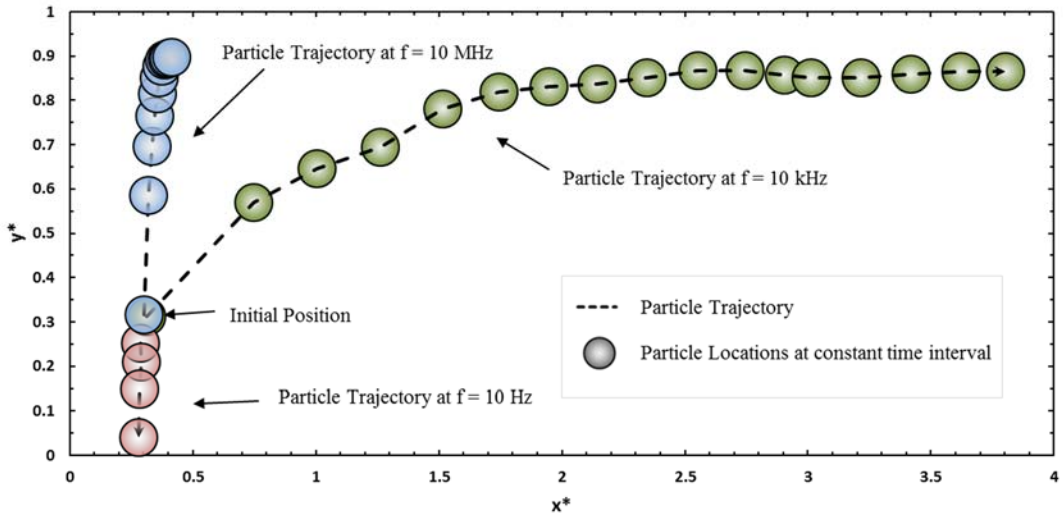

Figure 27. Particle positions and trajectories at different electric frequencies.

Initially, the particle located at (0.3, 0.3) is at rest. Once applying an electric field of a specific frequency, e.g., 10 Hz, 10 kHz and 10 MHz, to the electrodes, the particle will experience positive, negative or traveling-wave DEP forces, accordingly. At the low frequency f = 10 Hz, the particle is attracted to the electrode, as shown by the particle trajectory in Figure 27.

The positive DEP force increases rapidly when the particle approaches the electrode. Hence, as the particle moves towards the electrodes, it accelerates till it impact on the electrodes at t = 0.62 s. At the high frequency f = 10 MHz, the particle is repelled away from the electrode while the repulsive force decreases exponentially with the distance from the electrodes. Consequently, the particle decelerates as it moves away. At the moderate frequency f = 10 kHz, the particle experiences a significant twDEP force as well as a negative DEP force. The particle is pushed away from the electrode while being pushed forward against the direction of the propagation of the electric field. At t = 0.6 s, the particle travels to the location of (0.746, 0.570). Then, the particle is further pushed forward and elevated to (2.346, 0.852) at t = 4.82 s. After that, the particle stays at an approximately constant height. The equilibrium state of the particle is reached as the particle travels to $y^* \approx 0.86$ and the velocity remains at 0.32/s in the x direction.

5.3.2 twDEP of Two Particles

The numerical simulations are extended to study the different DEP modes of a pair of particles, P1 and P2, that are released from above an electrode. The electric field is applied at the time instant t = 0, and then the particles motion driven by the electric field are recorded.

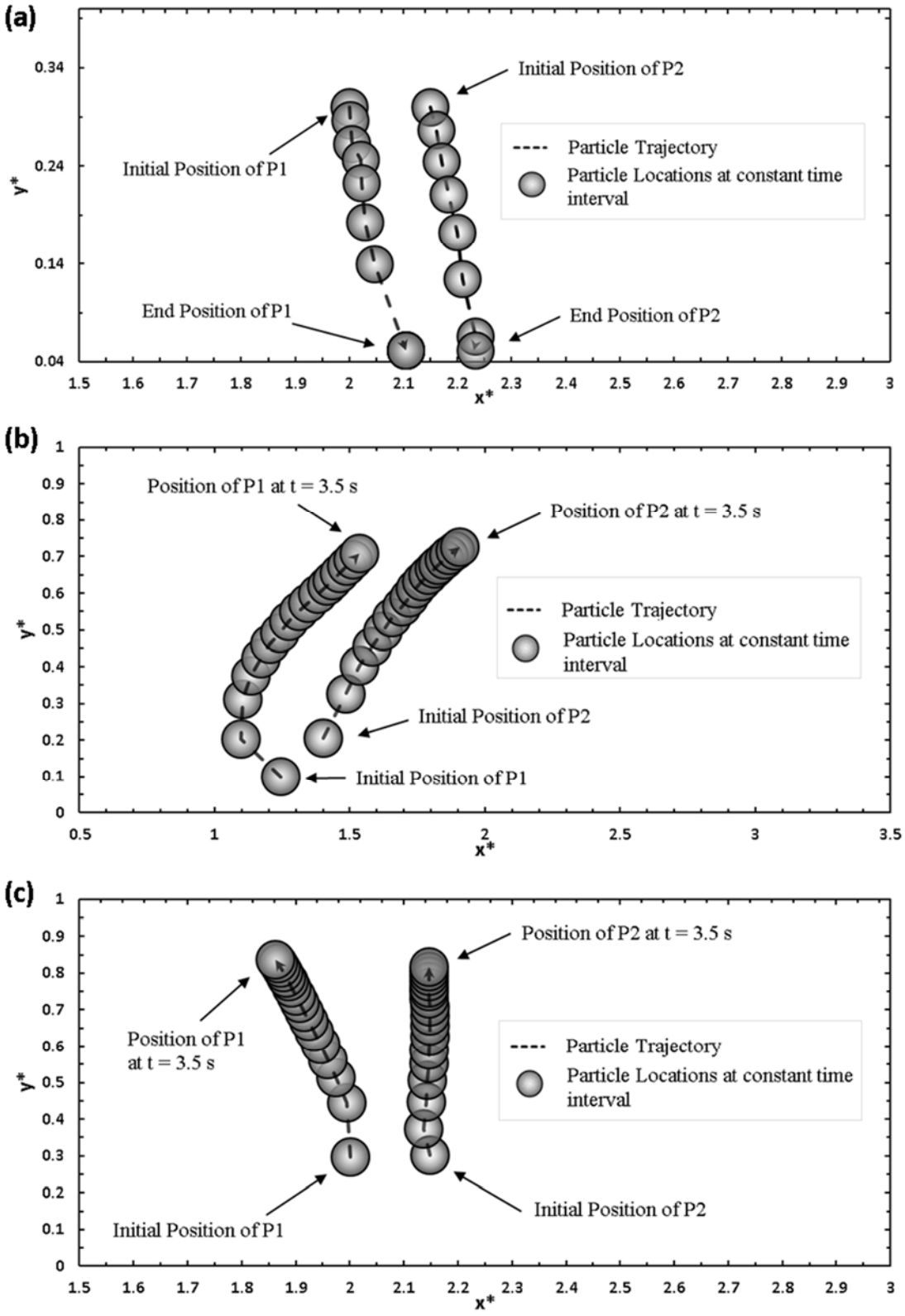

Figure 28. Positions and trajectories of two particles at f = 10 Hz (a), 10 kHz (b), and 10 MHz (c).

At the frequency f = 10 Hz, the centers of the particles are initially located at (2.00, 0.30) and (2.15, 0.30), as shown in Figure 28(a). Since the twDEP force on the particles is negligible at this frequency, the motion of the particles is dominated by positive DEP. Thus, the two particles are attracted to and eventually land on the electrodes. Similarly, when the driving frequency is increased to f = 10 MHz, the particles experience negative DEP. As presented in Figure 28(c), the two particles are repelled away and levitated to a certain height above the electrode array.

At f = 10 kHz, the conventional DEP and the twDEP force components are equivalently important. Two particles are released from two adjacent locations (1.25, 0.10) and (1.40, 0.20), and they are pushed away from the electrodes as the real part of the Clausius-Mossotti factor, Re[f_{CM}], is negative, i.e., negative DEP occurs. After levitation, both particles move against the propagation direction of the traveling-wave electric field due to the twDEP force.

5.3.3 twDEP of 100 Particles

The twDEP dynamics of 100 particles is discussed in this section with emphasis on the flow actuation effect, i.e., "pumping", generated by the collective motion of the particles. Since the numerical simulation results will be compared with the experimental measurements, the applied frequency of the electric field is set to be f = 6.9 kHz.

The spatial distribution of the DEP force is presented in Figure 29 where the magnitude of the force is color coded. From the contour and the vector field, it is seen that the twDEP force is in the negative direction at $y \geq 0.25$ and vortex occurs at $y \leq 20$ μm.

Also, the magnitude of the force reaches local minima at y ≈ 15 μm, which is the dark blue region.

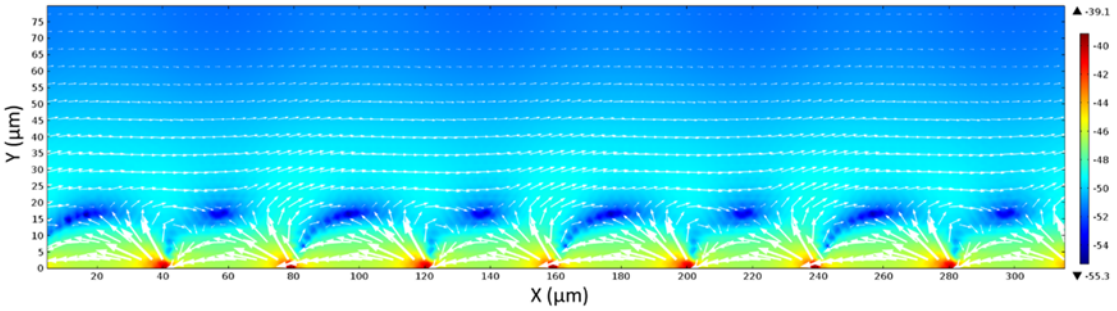

Figure 29. Distribution of the DEP force at f = 6.9 kHz using logarithmic scale.

Figure 30(a) shows that, at t = 0 s, 100 particles are uniformly distributed in the flow channel with an inter-particle spacing of 0.2 in both the vertical and horizontal directions. The orientation of each individual particle is indicated by the red dot marked on the particle. The subsequent positions of the 100 particles at t = 0.02 s and 3.0 s are shown in Figure 30(b) and (c). After applying the electric field, the particles start spinning, as evidenced by the orientation of the red markers, because of the DEP torques acting on them. As shown by the DEP torque distribution in Figure 26, the torque decreases with increasing height from the electrode array. Consequently, the particles located near the electrodes exhibit faster spinning than those at higher positions. The positions of the particles at t = 3.0 s are shown in Figure 30(c), where some are levitated after the electric signal is actuated while some near the bottom are attracted to the local maxima of the electric field.

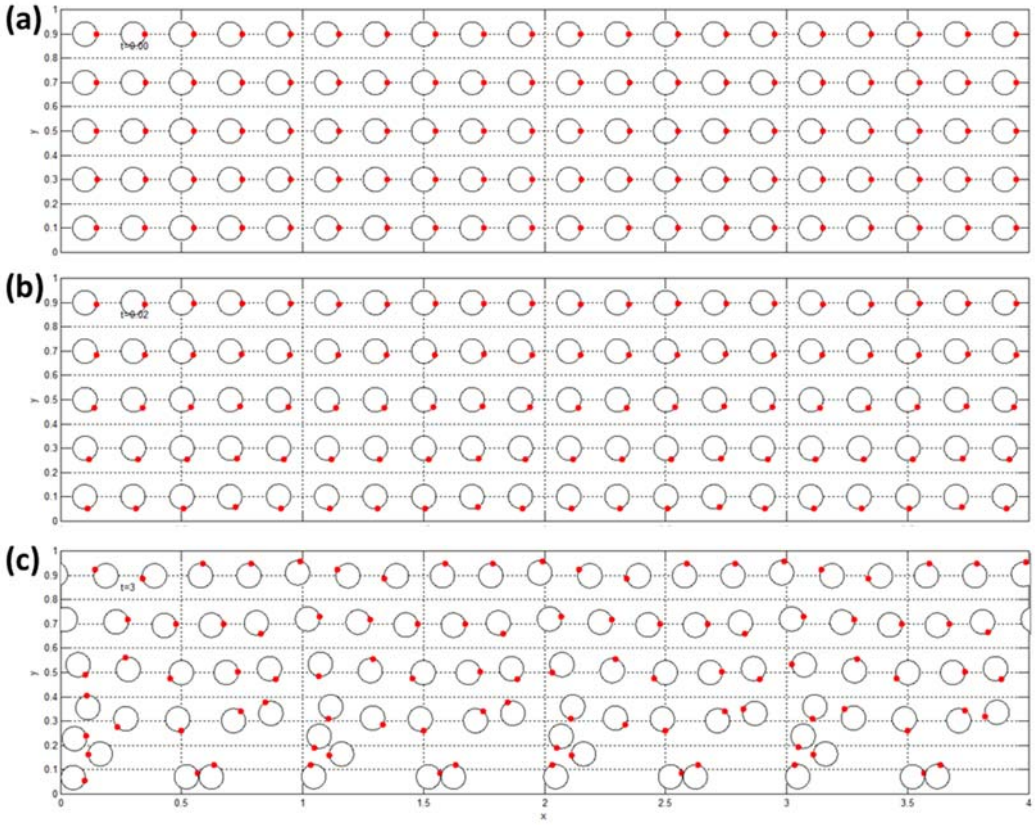

Figure 30. Particle locations at t = 0 s (a), t = 0.02 s (b), and t = 3.0 s (c).

While the particle travels via DEP in a surrounding fluid, it suffers a retarding drag force if the fluid is either moving slower than the particle or otherwise stationary. The fluid surrounding the particle is in turn dragged by viscous effects to accelerate in the same direction as the particle. The momentum exchange between the particle and the fluid reduces the velocity lag between the phases and eventually leads to an equilibrium state. A steady flow field is then established around the particle in the fluid as a result of this hydrodynamic interaction. In a particle suspension, a large collection of particles are present and the particles further interact hydrodynamically with neighbors. Consequently, the induced flow field is intensified and an appreciable net flow is produced by the collective pumping action. Figure 31 illustrates the velocity field generated by this

mechanism where a nearly parabolic velocity profile can be found in the microchannel. It is noteworthy that the velocity profile changes slightly with time. In the next section, the velocity profile at t = 0.5 s and t = 1.2 s will be compare with the μPIV measurements.

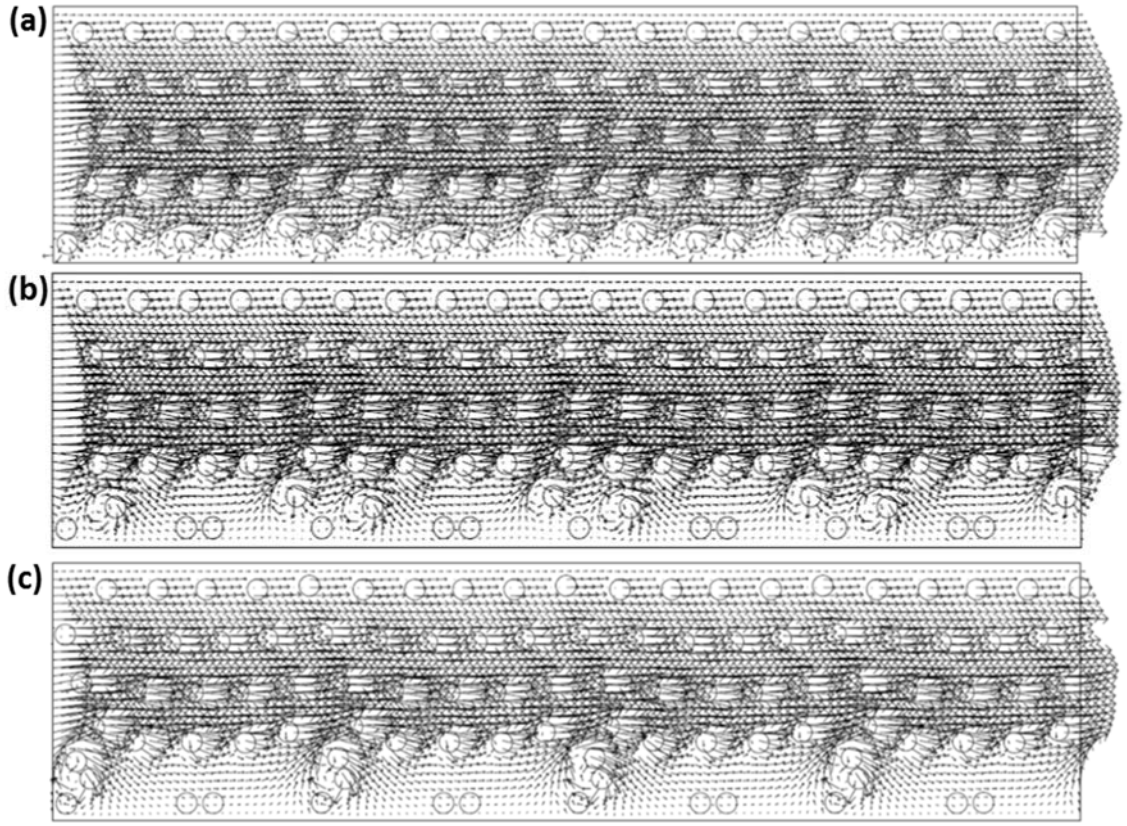

Figure 31. Velocity field at t = 0.5s (a), t = 1.2s (b), t = 3.7s (c).

5.4 Experiments

In order to verify the results from the numerical simulations, an experiment setup is constructed and μPIV is used to obtain the instantaneous velocity field induced by twDEP. The setup includes an interdigitated microelectrode array fabricated on a silicon wafer, a fluorescent microscope, a function generator and an image acquisition system.

5.4.1 Microfabrication

A twDEP test device was designed and fabricated. The device consists of an array of interdigitated microelectrodes fabricated using photolithography. With a silicon wafer as a substrate, the device is comprised of four distinct layers. The four layers, from the bottom to top, are an array of a bus bar sublayer, a dielectric film, the parallel electrodes and a top layer. At the bottom layer, two parallel bus bars representing Phase 2 and 3 of the traveling-wave are created by depositing 0.3 μm of Al with a sputtering system (AJA UHV six-source sputtering system) on a 3" silicon wafer. This layer is then deposited with AZ 1512 and photolithography followed by wet-etching. The second layer is comprised of SU-8 layer used as a dielectric layer to separate the electrode array and bus bar layer. A layer of 0.6 μm SU-8 is deposited directly on top of the bus bar layer with a spin coater (Brewer Cee 200 Spin Coater). Then a mask and photolithography is used to create the windows of electrical contact between the electrodes and the underlying bus bars.

Then, another layer of 0.5 μm Aluminum is deposited via the same sputtering system as used in the bottom layer. The aluminum oxide can form easily on the underlying layer of Al, which can increases the electric contact resistance between the two layers. Hence, a brief Ar sputter-etch is performed under vacuum before the deposition in order to remove the aluminum oxide. Then this layer of Al is patterned by wet-etching with AZ 1512 photolithography as before. The top dielectric layer is then deposited over the previous parallel electrodes layer to protect the metal electrodes from oxidation and corrosion. Then the wafer was baked to make sure its resistance to heat, electricity, or liquid. The detailed fabrication process is summarized in Table 2. The microfabrication is conducted in the Nanofabrication Facility at the University of Houston.

Table 2. Microfabrication procedures of four-phase electrodes.

1. Start with 3” silicon wafer
2. Solvent clean
3. Evaporate (or sputter deposit) Al ~0.3 μm thick
4. Solvent clean
5. Hard bake wafer in oven for 5 min at 120 °C
6. Spin coat with AZ 1518
7. Soft bake wafer in oven for 5 min at 90 °C
8. Expose photoresist with mask
9. Develop AZ 1512 photoresist
10. Rinse with DI water and dry with N2
11. Hard bake wafer in oven for 5 min at 120 °C
12. Aluminum wet etch exposed metallized regions
13. Strip AZ 1512 photoresist with solvent clean
14. Check for shorting with electrical isolation tests across different pads
15. Solvent clean
16. Rinse with DI water and dry with N2
17. Hard bake wafer in oven for 5 min at 120 °C
18. Spin coat a layer of SU-8 0.6um
19. Solvent clean
20. Soft bake wafer in oven for 5 min at 90 °C
21. Expose photoresist with mask
22. Develop SU-8 photoresist
23. Hard bake wafer in oven for 5 min at 120 °C
24. Sputter etch in Ar plasma
25. Sputter deposit Al 0.5 μm thick
26. Solvent clean
27. Repeat steps 7 -18 with another mask
28. Spin coat a layer of SU-8 0.6um
29. Hard bake wafer in oven for 5 min at 120 °C
30. Check for shorting across phases

The details of the twDEP device are shown in Figure 32. The array contains 50 sets of the electrodes, with each set consists of four electrodes, which are assigned to four electric phases. Each electrode measures 40 μm in width and is separated by 40 μm from the neighboring electrodes.

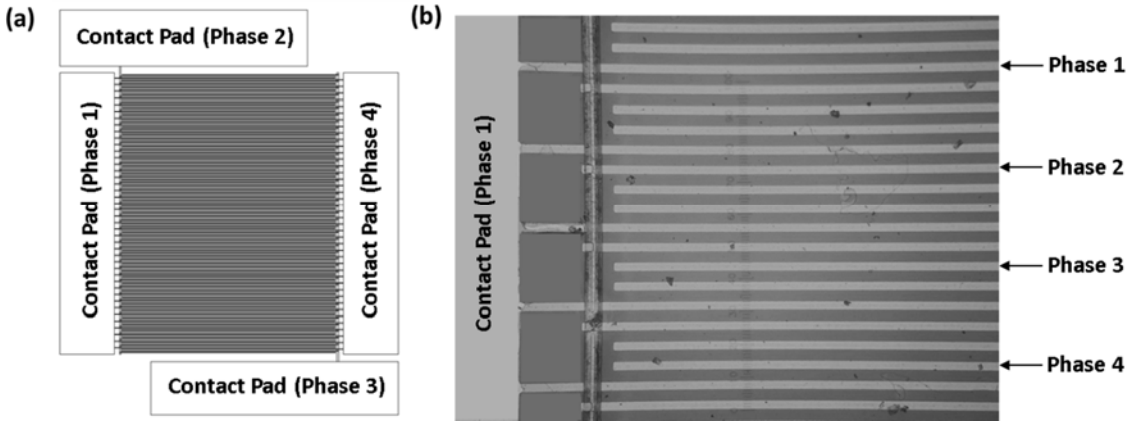

Figure 32. Prototype traveling wave DEP device with electrodes on a silicon wafer.

5.4.2 Experimental Procedure

In the experiments, the silicon wafer is mounted to a probe station with the electrodes connecting to an AC arbitrary waveform function generator (FLUKE 294), as shown in Figure 33. Spacers and a glass cover slide are placed on top the wafer to create a recirculating channel flow path which is 80 μm deep. The function generator is used to electrically activate each of the four phases on the fabricated circuit. The applied voltage is 20 V and the frequency is 6.9 kHz. A digital oscilloscope (Tektronix TDS 310) is used to monitor the voltage, frequency and waveform of the sinusoidal signal applied.

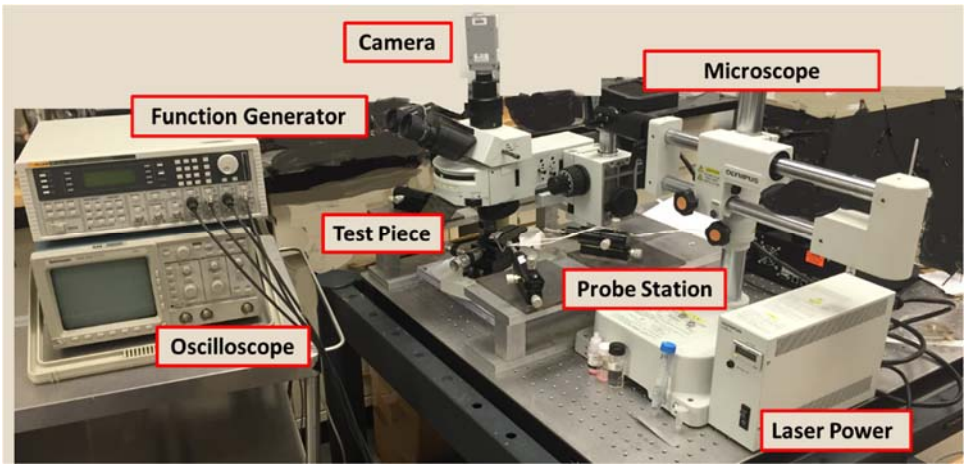

Figure 33. Experiment apparatus for traveling wave DEP.

Time-resolved images for particle image velocimetry (PIV) are captured through an Olympus microscope with a 50× objective lens (N.A. = 0.5, W.D. = 10.6 mm, F.N. = 26.5 mm) and a high speed CCD camera (PixeLINK PL-B742U). The camera can provide 24 fps at a full pixel resolution of 1280×1024 and up to 7200 fps at 724×8. The colloidal solution is prepared by mixing fluorescent polystyrene particles of 780 nm diameter (Thermo Scientific, CA) with DI water. The conductivity of the polystyrene particles and the DI water are measured to be 5×10^{-5} S/m and 5.5×10^{-6} S/m, respectively, while the relative dielectric permittivity are 2.8 and 78.4.

5.4.3 Experiment Results

The motion of the particles in the twDEP is recorded and presented in Figure 34 at three different heights: (a) h = 0, (b) h = 20 μm and (c) h = 70 μm. The consecutive images of the particle positions are recorded at 25 fps with an applied AC electric field (V = 20 V, f = 6.9 kHz).

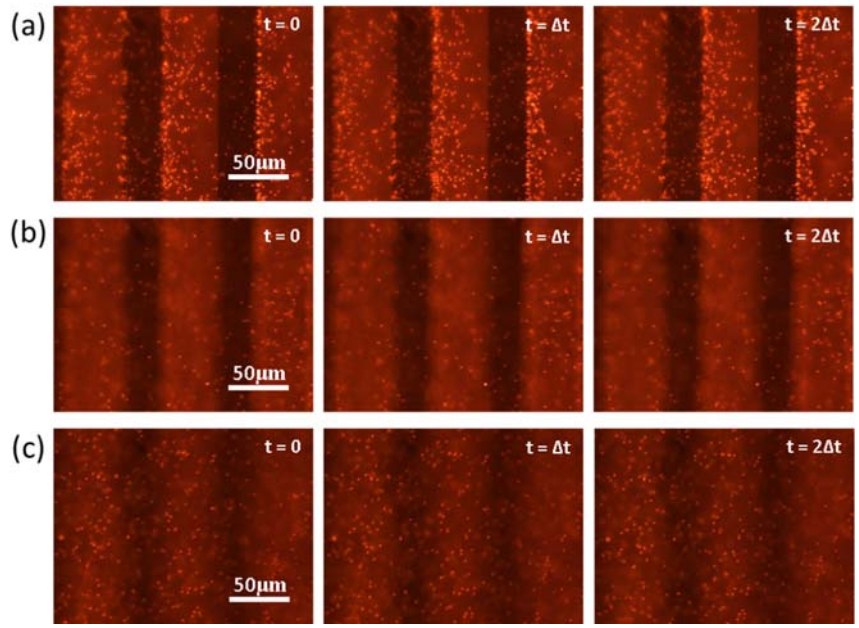

Figure 34. Snapshots of particle motion with twDEP at (a) h = 0, (b) h = 20 µm, and (c) h=70 µm.

Microparticle image velocity (µPIV) software EDPIV is then used to analyze all the images to obtain the quantitative measurements of the spatial velocity field at those heights. The results are shown in Figure 35. Figure 35(a) shows that at h = 0, the velocity is positive in most regions and the velocity is strong near the edges of the electrodes. This observation matches the dielectrophoretic force distribution in Figure 29 and the velocity profile in Figure 31. At h = 20 µm, Figure 35(b) shows that the average velocity is around 65 µm/s, which is approximately the maximum velocity along the height of the microchannel. When the height further increases to h = 70 µm, the average velocity reduces to 20.5 µm/s, almost half of that at h = 20 µm, as shown in Figure 35(c). This is not surprising since the twDEP force decays exponentially with the distance from the electrodes.

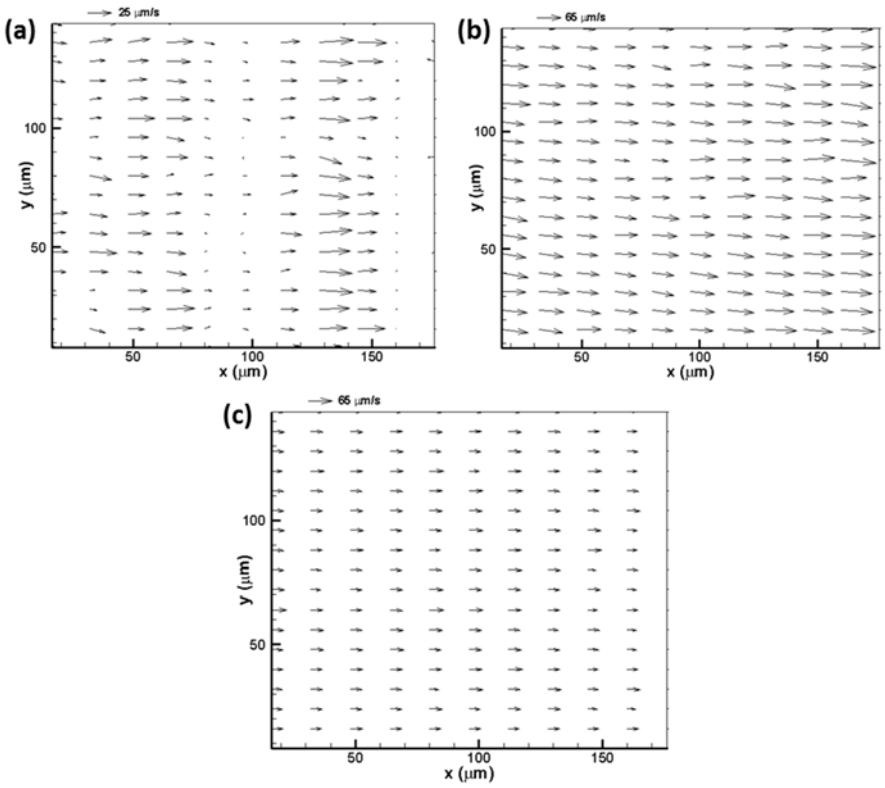

Figure 35. Velocity field with μPIV measurement at height h = 0 (a), h=20μm (b), h=70μm (c).

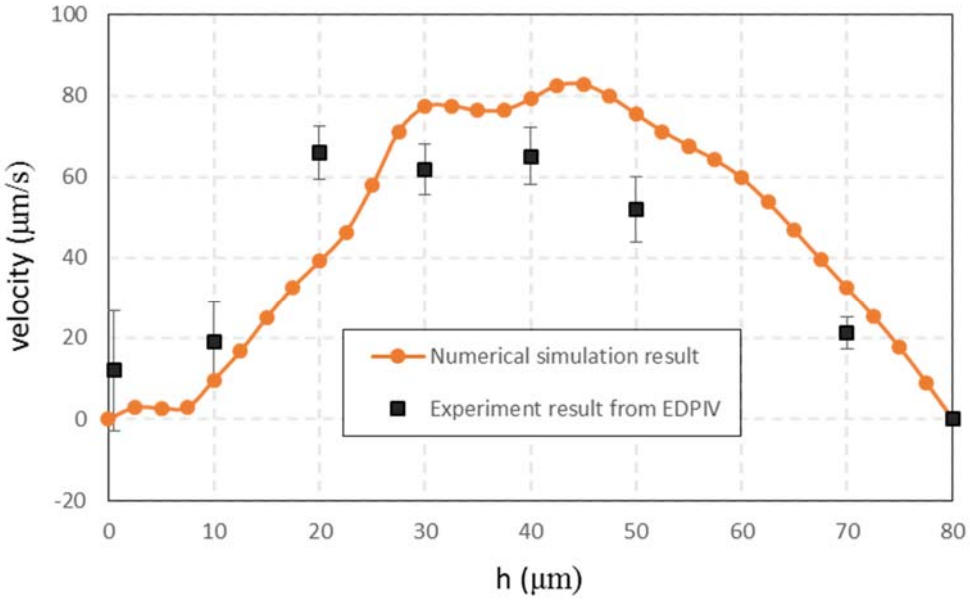

Figure 36. Comparison of velocity profile between the experiments and numerical simulations.

The mean velocity at each height of the channel is then obtained by averaging all the velocity data at that height from the μPIV measurement. In Figure 36, the velocities are plotted as a function of the height of the microchannel (from h = 0 to 80 μm). The velocity profile from numerical simulation at a steady flow state is also included. From the comparison, it can be concluded that the experiment data and the simulation results show a satisfactory agreement.

5.5 Conclusions

In this chapter, both numerical simulations and experimental measurements are undertaken to investigate the twDEP motion of particles and the collective fluid flow in a microchannel. The particle motion and trajectory are first studied numerically using model systems consisting of one, two and a hundred particles. The effects of the driving frequency of the applied electric field on DEP are investigated in great detail. A four-phase microelectrode test piece is fabricated, and μPIV measurements are conducted to obtain the instantaneous velocity field induced by the twDEP of nanoparticles suspended in a colloidal solution. The measured velocity profile is compared with the numerical results.

Chapter 6 Electrohydrodynamics vs Traveling Wave DEP

6.1 Introduction

In this Chapter, we discuss another phenomena, called electrohydrodynamics, which comes along with traveling wave dielectrophoresis, when a temperature gradient is introduced in the colloidal solutions by Joule heating effect. This effect could interfere, synergistically or competitively, the flow induced by traveling wave dielectrophoresis. This work has been published [134].

The ability to generate fluid flow in small amounts with high precision is critical to the continued growth of microfluidic technology, which is now widely applied in drug delivery [135], chemical synthesis [136], biological diagnostics [137] and electronics cooling [138]. Conventional pumping methods driven by mechanical means are proven unsuitable for microfluidic applications due to their limits in miniaturization and lack of precision and flexibility in controlling low flow rates [139, 140]. Among the alternative solutions, a particularly attractive scheme is to exploit the AC electrokinetic effects, i.e., to generate the flow by inducing electrical forces in the fluid with an applied traveling-wave electric field. Based on the origin of the electrical forces, electrokinetic micropumps can be classified as the induced-charge electroosmotic (ICEO) micropump [141, 142], dielectrophoretic (DEP) micropump [57], and electrohydrodynamic (EHD) micropump [143-145], etc.

In ICEO micropumps, the electrical double layer (EDL) is formed by the normal component of the traveling wave field at the interface between the electrode and the electrolyte solution. The tangential component of the field then acts on the mobile charges

accumulated in the EDL, pulling the fluid along the direction of the traveling wave. The EHD micropumps are also generated through the interaction of an electric field with induced charges (ions). However, the charge induction usually occurs in the bulk of a fluid medium by the presence of a temperature gradient through anisotropic heating. The induced ions can be attracted or repelled by the traveling-wave field, so that the fluid moves together with the ions owing to viscous drag. Although both ICEO and EHD micropumps involve a traveling-wave field, they can be discerned without ambiguity because they operate at very different frequency range [57, 146]. For instance, the maximum effect of EHD occurs near the charge relaxation frequency $f_c = \sigma_m/(2\pi\varepsilon_m)$ [147], while the optimal frequency of ICEO is around $f_{ICEO} = [\sigma_m/(2\pi\varepsilon_m)]/(\lambda_D/L)$, where λ_D is the Debye length and L is the characteristic length of the system, and f_{ICEO} is several orders of magnitude smaller than f_c.

Traveling-wave DEP (twDEP) is the sustained motion of dielectric particles in a fluid when exposed to a multi-phase (> 2 phases) traveling-wave field [9]. The driving force is derived from the interaction of the field with the induced electric dipole in the particles. When the moving particles drag the surrounding fluid together with them, an appreciable net flow, i.e., the twDEP micropumping, is generated [9]. The maximum twDEP is expected to take place near the Maxwell-Wagner relaxation frequency, $f_{M\text{-}W}$,

$$f_{M-W} = \frac{1}{2\pi}\left(\frac{\sigma_p + 2\sigma_m}{\varepsilon_p + 2\varepsilon_m}\right). \tag{118}$$

This frequency is of the same order of magnitude of the charge relaxation frequency of EHD (f_c) at which the maximum EHD pumping occurs. In fact, they can coincide for

certain particle-fluid combinations. For instance, if $\sigma_p << 2\sigma_m$ and $\varepsilon_p << \varepsilon_m$, $f_{M\text{-}W}$ will reduce to f_c. Furthermore, the velocity fields produced by twDEP micropumping and EHD micropumping are typically comparable in magnitude, however, their flow directions may be totally opposite (as will be discussed below). Consequently, when a traveling-wave electric field is applied to transport colloidal suspensions, where the subject of interest can be either the particles or the carrier liquid, the twDEP-induced flow and EHD-induced flow are simultaneously present. These two pumping mechanisms may cooperate or compete with each other, depending on their relative flow directions with respect to the applied electric field. Thus it is important to analyze the EHD-twDEP coupled flow and its potential variations in order to ensure satisfactory liquid/particle delivery capability of a microfluidic system that employs the AC electrokinetic effects [57, 148-150].

In this Chapter, the coupled EHD and twDEP electrokinetic flow is studied numerically in a microchannel which has an interdigitated microelectrode array fabricated at the bottom surface. The EHD flow is induced by the Joule heating effect in the electrolyte solution. Both the repulsion-type and the attraction-type EHD were considered. The flow field due to twDEP is solved using an equivalent mixture. The results show, depending on the frequency range of the traveling-wave field and the thermal boundary condition, the EHD effect and the twDEP effect can work either synergistically or competitively to strengthen or weaken the net flow generated.

6.2 Theory and Analysis

6.2.1 Electrohydrodynamics

Electrohydrodynamic (EHD) flow arises as the result of the interaction of an electric field with free charges induced in a fluid medium. The charge induction occurs when a temperature gradient ∇T exists in the bulk of the liquid, which brings about gradients in the temperature-dependent electrical conductivity and permittivity. Upon the application of an electric field, the electrical force drives the free charges into motion, thereby producing the bulk fluid flow. EHD pumping due to preexisting temperature gradient, e.g., a temperature difference imposed across the boundaries of the fluid, has been studied extensively for heat transfer enhancement applications [147, 151-153]. Under a difference circumstance, when the fluid medium has a non-negligible electrical conductivity, the high electric field normally used in electrokinetics studies can generate appreciable Joule heating, which causes a substantial temperature gradient in the bulk liquid [154]. EHD originating from Joule heating is also termed the electrothermal effect [155], and is considered in this work. The steady-state energy equation for the fluid is given as

$$\rho c_p \left(\vec{u} \cdot \nabla T\right) = k\nabla^2 T + \sigma E^2 \ , \tag{119}$$

where the heat generation source term σE^2 is due to Joule heating.

The electrical force due to EHD is given by [156]

$$\vec{f}_e = \rho_q \vec{E} - \frac{1}{2} E^2 \nabla \varepsilon 2 \ , \tag{120}$$

where ρ_q is the free charge density, and $\vec{E}$ is the electric field. The two terms at the right hand side (RHS) of Eq. (120) represent the Coulomb and dielectric forces, respectively. The free charge density is related to the electric field by Gauss's law

$$\rho_q = \nabla \cdot \left(\varepsilon \vec{E} \right) , \tag{121}$$

and the charge conservation equation is

$$\frac{\partial \rho_q}{\partial t} + \nabla \cdot \vec{J} = 0 , \tag{122}$$

where the current density $\vec{J}$ consists of the convection current, the conduction current and the diffusion current, and is given by

$$\vec{J} = \rho_q \vec{u} + \sigma \vec{E} - D \nabla \rho_q , \tag{123}$$

where D is the diffusivity. The convection and diffusion currents can be neglected in this work since they are much smaller than the conduction current [155, 157].

Assuming small variations in the permittivity and electrical conductivity, the electric field can be written as the sum of the applied component $\vec{E}_0$ and the perturbation component $\vec{E}_1$, where $\vec{E} = \vec{E}_0 + \vec{E}_1$ and $\left|\vec{E}_0\right| \gg \left|\vec{E}_1\right|$. The electrical force becomes

$$\vec{f}_e = \left(\nabla \varepsilon \cdot \vec{E}_0 + \varepsilon \nabla \cdot \vec{E}_1 \right) \vec{E}_0 - \frac{1}{2} {E_0}^2 \nabla \varepsilon . \tag{124}$$

Eqs. (121) and (122) can be combined as

$$\nabla\sigma\cdot\vec{E}_0+\sigma\nabla\cdot\vec{E}_1+\frac{\partial}{\partial t}\left(\nabla\varepsilon\cdot\vec{E}_0+\varepsilon\nabla\cdot\vec{E}_1\right)=0\ . \tag{125}$$

In an applied AC field of angular frequency ω, $\vec{E}_0(t)=\mathrm{Re}\left(\vec{E}_0 e^{i\omega t}\right)$ and $\partial/\partial t=i\omega$, where Re(…) is the real part of a complex quantity. From Eq. (125), it follows

$$\nabla\cdot\vec{E}_1=\frac{-\left(\nabla\sigma+i\omega\nabla\varepsilon\right)\cdot\sigma+i\omega\nabla\varepsilon}{\sigma+i\omega\varepsilon}\ . \tag{126}$$

Putting Eqs. (124) and (126) together, the time-averaged electrical force can be given by

$$\left\langle\vec{f}_e\right\rangle=\frac{1}{2}\mathrm{Re}\left\{\left[\frac{\left(\sigma\nabla\varepsilon-\varepsilon\nabla\sigma\right)\cdot\vec{E}_0}{\sigma+i\omega\varepsilon}\right]\vec{E}_0^{\,*}-\frac{1}{2}E_0{}^2\nabla\varepsilon\right\}\ , \tag{127}$$

where * denotes the complex conjugate. Alternatively, Eq. (127) can be recast as

$$\left\langle\vec{f}_e\right\rangle=\frac{1}{2}\left[\left(\frac{\nabla\varepsilon}{\varepsilon}-\frac{\nabla\sigma}{\sigma}\right)\cdot\vec{E}_0\,\frac{\varepsilon\vec{E}_0}{1+\left(\omega\tau\right)^2}-\frac{1}{2}E_0{}^2\nabla\varepsilon\right]\ , \tag{128}$$

where $\tau=\varepsilon/\sigma$ is the charge relaxation time. The variations in permittivity and conductivity are related to the temperature gradient as

$$\frac{\nabla\sigma}{\sigma}=\frac{1}{\sigma}\left(\frac{\partial\sigma}{\partial T}\right)\nabla T\quad\text{and} \tag{129}$$

$$\frac{\nabla\varepsilon}{\varepsilon}=\frac{1}{\varepsilon}\left(\frac{\partial\varepsilon}{\partial T}\right)\nabla T\ . \tag{130}$$

The EHD-induced flow field can be described by the Navier-Stokes equations for an incompressible fluid

$$\rho\left(\frac{\partial \vec{u}}{\partial t}+\vec{u}\cdot\nabla\vec{u}\right)=-\nabla p+\mu\nabla^2\vec{u}+\vec{f}_b+\vec{f}_e\ , \tag{131}$$

and the continuity equation is

$$\nabla\cdot\vec{u}=0\ , \tag{132}$$

where $\vec{f}_b$ is other body forces if present. Considering the small velocity involved in most microfluidic studies, the inertia term can be omitted from Eq. (131) since the Reynolds number is usually less than unity ($\mathrm{Re}=\rho uL/\mu\le 1$). Further neglecting the body force, Eq. (131) reduces to the Stokes equation

$$0=-\nabla p+\mu\nabla^2\vec{u}+\vec{f}_e\ . \tag{133}$$

6.2.2 Dielectrophoresis

As introduced before, dielectrophoresis (DEP) is the motion of dielectric particles in colloidal suspensions when exposed to non-uniform electric fields [9]. When an electric field is applied, the re-distribution of electrical charges in the particle gives rise to an induced dipole across the particle.

The induced dipole tends to align with the applied field. The induced dipole moment, $\vec{p}$, and the dielectrophoretic force, $\vec{F}$, are given by

$$\vec{p}=4\pi a^3\varepsilon_m\left(\frac{\varepsilon_p-\varepsilon_m}{\varepsilon_p+2\varepsilon_m}\right)\vec{E}\quad\text{and} \tag{134}$$

$$\vec{F}=\left(\vec{p}\cdot\nabla\right)\vec{E}=2\pi a^3\varepsilon_m\left(\frac{\varepsilon_p-\varepsilon_m}{\varepsilon_p+2\varepsilon_m}\right)\nabla\vec{E}^2\ . \tag{135}$$

If the applied field is non-uniform ($\nabla\vec{E} \neq 0$), the particle will experience a net force and move [9, 72]. In a DC field, the particles can either undergo positive DEP, i.e., they are attracted to the maxima of the field, or experience negative DEP, i.e., they are repelled to the field minima.

Sustained particle motion is possible when an AC traveling-wave field is applied with appropriate driving frequencies. The AC dielectrophoretic force on the particle can be expressed using the frequency-dependent permittivity as [72]

$$\vec{F} = 2\pi a^3 \varepsilon_m \left(\frac{\tilde{\varepsilon}_p - \tilde{\varepsilon}_m}{\tilde{\varepsilon}_p + 2\tilde{\varepsilon}_m} \right) \nabla \vec{E}^2 \ , \tag{136}$$

where $\tilde{\varepsilon}$ is $\tilde{\varepsilon} = \varepsilon - i(\sigma / \omega)$ and $i = \sqrt{-1}$. In the time domain, the time-averaged DEP force becomes [150]

$$\left\langle \vec{F}_{DEP} \right\rangle = \pi a^3 \varepsilon_m \, \mathrm{Re}\left(f_{CM} \right) \nabla \left| \vec{E} \right|^2 + 2\pi a^3 \varepsilon_m \, \mathrm{Im}\left(f_{CM} \right) \left(E_x{}^2 \nabla \varphi_x + E_y{}^2 \nabla \varphi_y \right) \ , \tag{137}$$

where the Clausius-Mossotti factor, f_{CM} is a complex parameter, defined as

$$f_{CM} = \frac{\tilde{\varepsilon}_p - \tilde{\varepsilon}_m}{\tilde{\varepsilon}_p + 2\tilde{\varepsilon}_m} \ . \tag{138}$$

Here Re(f_{CM}) and Im(f_{CM}) denote the real and imaginary parts of f_{CM}, E_x, E_y and E_z are the three directional components of the electric field; and φ_x, φ_y and φ_z are the phase angles. The first term on the RHS of Eq. (137) determines the alignment of the DEP force with respect to the maxima/minima of the electric field. The second term appears only in

a traveling-wave field and therefore, is called the traveling-wave DEP (twDEP) force component.

When the particles are driven into motion by twDEP, the viscous drag will pull the surrounding fluid to move together with the particles. Eventually, the twDEP driving force is balanced by the viscous drag force

$$\left\langle \vec{F}_{DEP} \right\rangle = -6\pi \mu_f a \left(\vec{u}_m - \vec{u}_p \right) . \tag{139}$$

Once the equilibrium state is reached, a steady flow field will be established around the particle. In a particle suspension where a large number of particles are present, the particle-particle hydrodynamic interactions take place as the inter-particle distance decreases, which will intensify the induced flow field [158]. Consequently, an appreciable net flow can be produced by the collective pumping action [57].

6.2.3 Interference between EHD and twDEP

The direction of EHD flow with respect to the traveling-wave field is determined by the temperature distribution in the fluid [147]. When the lowest fluid temperature happens to be near or at the electrodes where the electric field is most intense, the induced free charges will be attracted toward the traveling wave and the fluid will follow the electric field in the same direction, resulting in the attraction-type EHD. Conversely, in the case of repulsion-type EHD where the fluid temperature is higher near the electrodes, the induced flow will be opposite to the direction of the traveling wave.

The twDEP motion of particles with respect to the traveling wave field is contingent upon the Clausius-Mossotti factor, f_{CM}, as indicated by Eq. (137). Figure 37 illustrates

Re(f_{CM}) and Im(f_{CM}) as a function of the frequency of the applied field (polystyrene particles suspended in the 2.2×10^{-5} M KCl solution).

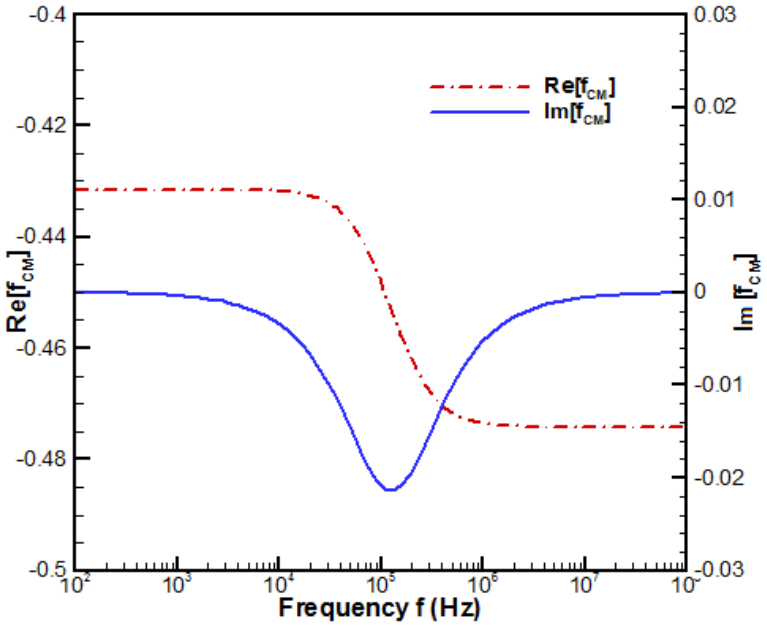

Figure 37. Frequency-dependence of Re(f_{CM}) and Im(f_{CM}).

It is seen Re(f_{CM}) is always negative over the entire frequency range, ensuring the particles can move freely without being immobilized onto the electrodes. Im(f_{CM}) vanishes at both extremes of the frequency spectrum, and only assumes non-zero values in the mid-range around the cross-over frequency ($f_{M\text{-}W}$). When Im(f_{CM}) is not trivial, the resulting twDEP force will propel the particles either along or against the propagation direction of the traveling wave, depending on the sign of Im(f_{CM}). For the particle-fluid combination used in this work, Figure 37 shows Im(f_{CM}) < 0, the particles as well as the twDEP-induced flow always move against the traveling wave. Therefore, when both EHD and twDEP effects are present, the net induced flow can be either enhanced if the EHD-induced flow is repulsion-type (i.e., also against the traveling wave), or diminished if the EHD-induced

flow is attraction-type (i.e., along the traveling wave), depending on the temperature distribution in the fluid.

6.3 Numerical models

The microfluidic system to be modeled consists of an array of three-phase, planar parallel microelectrodes fabricated on a silicon substrate, a microchannel, and a glass cover slide, as shown in Figure 38. The height of the microchannel formed is 50 μm. The electrodes are very thin (~ 100 nm) and are 8 mm long.

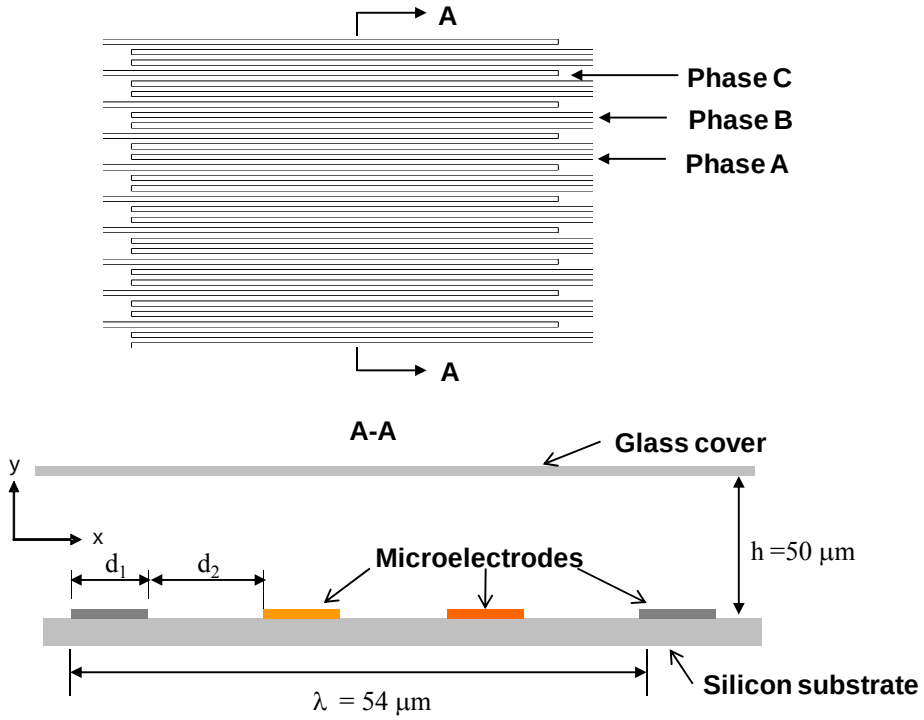

Figure 38. The microfluidic system.

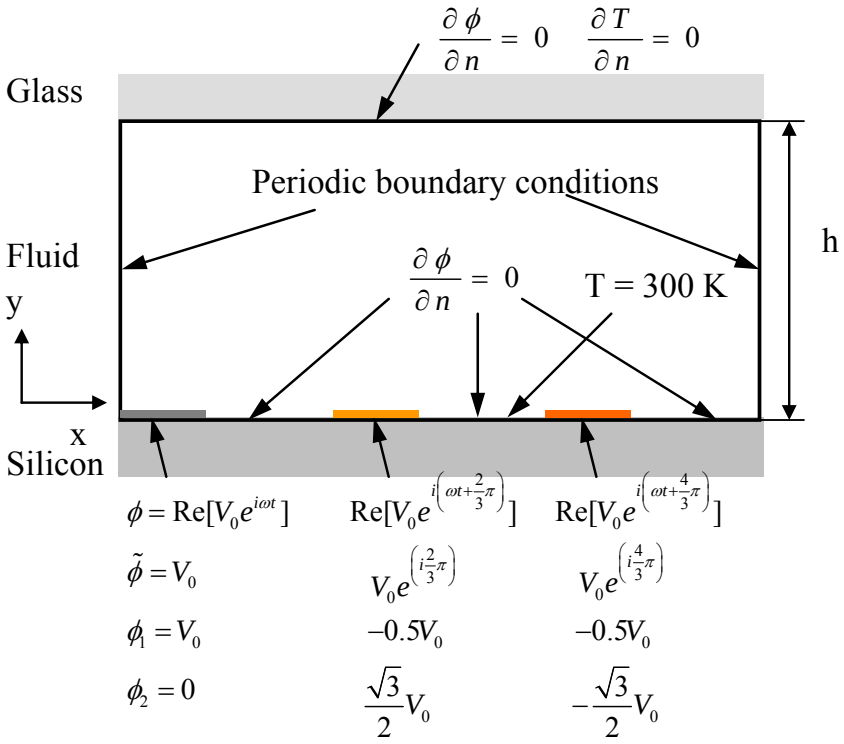

Figure 39. The computational domain and the electrical boundary conditions.

They have a width and a spacing of d_1 = 6 μm and d_2 = 12 μm, which yield a wavelength of $\lambda = 3(d_1 + d_2)$ = 54 μm. The electrode array can be treated as a two-dimensional system because the length (8 mm) along the transverse direction is considered infinite relative to the other two dimensions. The computational domain is shown in Figure 39, for which the electric, temperature and velocity fields will be solved. Due to periodicity consideration, only a distance along the electrodes of one wavelength is modeled that covers three electrodes and their inter-spacing gaps.

A low-concentration KCl solution (2.2×10^{-5} M) is used as the working fluid for both EHD and twDEP simulations. The solution has an electrical conductivity of $\sigma = 5.43 \times 10^{-4}$ S/m, a dielectric constant of $\varepsilon_r = 80$, and the temperature coefficients of 2.11% K^{-1} for σ and – 0.4% K^{-1} for ε [147]. The density, viscosity and thermal conductivity of the

KCl solution are assumed to be the same as water (ρ = 997 kg/m^3, $\mu = 5.28\times10^{-4}$ N s/m^2 and k = 0.7 W/(m K). In the twDEP simulation, polystyrene microparticles of 2.9 μm diameter are dispersed in the KCl solution at a volume fraction of 1%. The electrical conductivity and dielectric constant for polystyrene are $\sigma = 5.2 \times 10^{-5}$ S/m and $\varepsilon_r = 2.8$, respectively.

6.3.1 Electric field

The electric fields are generated by applying a traveling-wave voltage signal to the three-phase electrode arrays. For a harmonic electric field of angular frequency ω, the electrical potential in the computational domain can be written in phasor notation as [62]

$$\phi(\vec{x},t) = \mathrm{Re}[\tilde{\phi}(\vec{x})e^{i\omega t}] \ , \tag{140}$$

where the phasor $\tilde{\phi} = \phi_1 + i\,\phi_2$, and $\omega = 2\pi f$ (f is the frequency of the applied field). The harmonic electric field is obtained from $\vec{E}(\vec{x},t) = \mathrm{Re}[\tilde{\vec{E}}(\vec{x})e^{i\omega t}]$, where $\tilde{\vec{E}}(\vec{x}) = -\nabla\tilde{\phi} = -(\nabla\phi_1 + i\,\nabla\phi_2)$. Since the fluid and the particles are assumed to be homogeneous, linear dielectric materials, both ϕ_1 and ϕ_2 satisfy Laplace's equation $\nabla^2\phi_i = 0$ (i = 1, 2).

The boundary conditions are specified as follows. On the top glass surface, a Neumann condition ($\partial\phi/\partial n = 0$) is assumed, where n is the normal to the boundary [157]. On the bottom surface, three-phase traveling-wave potentials are assigned to the electrodes, as shown in Figure 39. A sinusoidal voltage $\phi(t) = \mathrm{Re}[V_0 e^{i\omega t}]$ is applied to the first electrode, and the signals on consecutive electrodes are phase-shifted by $2/3\pi$. The

corresponding boundary values of ϕ_1 and ϕ_2 on the electrodes are illustrated in Figure 39. For the inter-spacing gaps, the Neumann condition is specified since the neighboring electrodes are isolated from each other by using dielectric films, resulting in zero potential flux in the gaps. Periodic boundary conditions are imposed at the left and right boundaries of the computational domain.

6.3.2 Temperature and velocity fields

Since the thermal conductivities of glass and silicon are two orders of magnitude different (i.e., they are 1.4 W/mK and 148 W/mK, respectively), two kinds of thermal boundary conditions are considered in this work. Under the first thermal boundary condition (BC-1), the top surface is assumed adiabatic ($\partial T / \partial n = 0$), and the bottom surface is assumed to be equal to the room temperature 300 K as a result of good conduction through the silicon substrate. This is the standard thermal boundary condition used in solving heat transfer problems in microchannel flows [159]. When heat losses due to natural convection are considerable, the second kind of thermal boundary condition (BC-2) is possible, where a convective heat transfer coefficient of 30 W/m^2 K is applied to both boundaries [160]. Under steady state, thermally fully developed boundary conditions are assigned to the vertical edges of the computational cell. The boundary conditions for the velocity field calculation are: (1) no-slip conditions for the top and bottom surfaces and (2) periodic conditions for the left and right boundaries, i.e., the flow inlet and outlet.

6.3.3 Numerical methods

A commercial computational fluid dynamics (CFD) software package, FLUENT, is employed to solve the electrothermal and electrohydrodynamic problems [160, 161].

The general solution procedures are as follows. First, the electrical potential (ϕ) and the electric field ($\vec{E}$) are acquired by solving the Laplace's equation $\nabla^2\phi = 0$. Then the solutions are used in conjunction with the user-defined functions to compute the EHD force and DEP force defined in Eqs. (128) and (137). Finally, the Stokes equations are solved to obtain the velocity field.

In the EHD simulation, the velocity and temperature fields are coupled and can be calculated by solving Eqs. (119), (131) and (132) simultaneously. It is noted that if the temperature gradient in EHD is established by a pre-existing constant temperature difference across the boundary of the fluid (∇T = constant), the electrical force can be calculated directly from Eqs. (128) through (130) without having to solve the energy equation.

In the DEP calculation, the electrical force acts on discrete solid particles rather than on the continuous fluid elements. Here, instead of using the two way coupled fluid-particle interactions DLM/FD method, a simplified, equivalent mixture model is adopted here. The DEP force is treated as a continuous body force in the fluid by volume-averaging, i.e., the DEP force on one particle is averaged over the fluid volume surrounding that particle, whose size is determined by the particle volume fraction.

This continuous approach is warranted by the fact that there are ample particles in the suspension and their random passages in space make their presence ergodic [9]. The DEP force is then used as the electric force term in Eq. (131) to solve for the induced flow field. By following this procedure, the complex solid-liquid two-phase flow problem is converted to an equivalent, but more straightforward single-phase fluid flow problem.

In the simulations, the computational domain is discretized using a 106 × 200 (x-y) grid. Simulations with different grids show a satisfactory grid-independence for the results obtained with this mesh size. The simulations are performed for V_0 =10 V and three frequencies of f = 10 kHz, 100 kHz and 1 MHz, respectively.

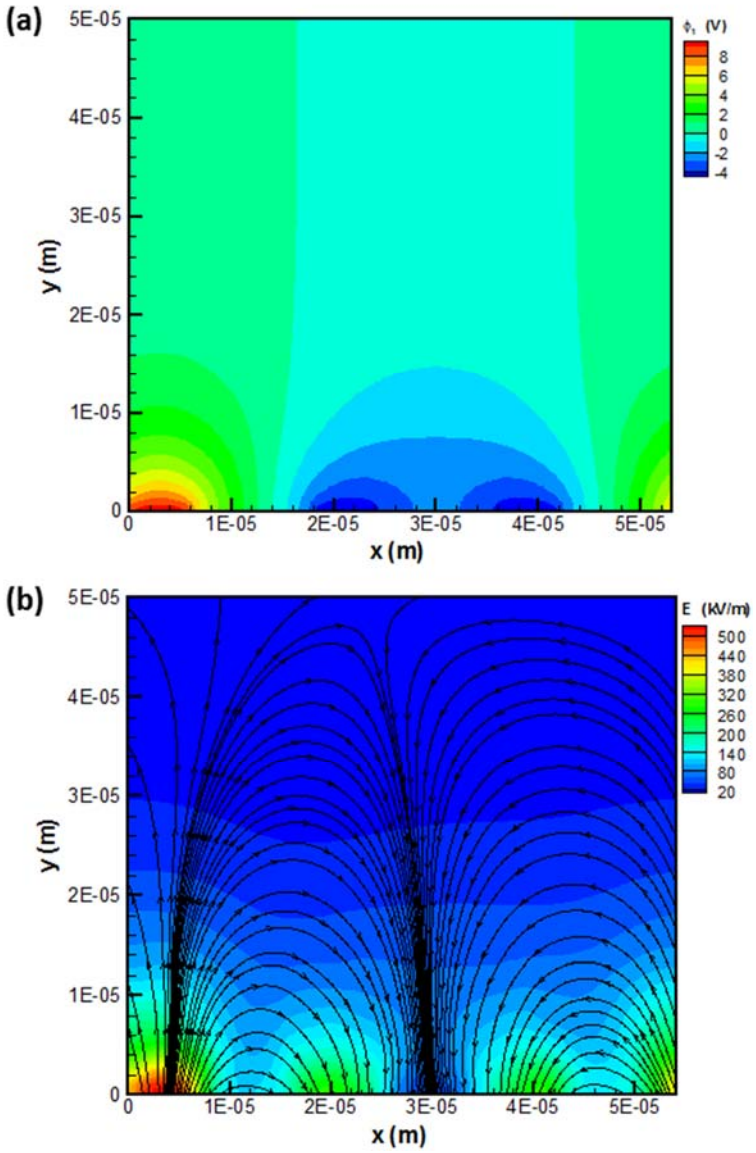

Figure 40. Solution of the electric field: (a) the electric potential ϕ and (b) the electric field E.

6.4 Results and Discussion

6.4.1 Electric field solution

Numerical results for the electric potential and the electric field are illustrated in Figure 40 for $V_0 = 10$ V. Figure 40(a) shows that the electric potential decays rapidly with increasing distance from the electrode surface.

Since the density of the field lines is proportional to the strength of the electric field, Figure 40(b) shows clearly that the field maxima are located near the edges of the electrodes, and the local minima appear in the inter-spacing gaps. In all the simulations, the applied traveling-wave propagates from the left side to the right of the computational domain.

6.4.2 Electrohydrodynamics

Figure 41 presents the temperature distributions in the microchannel under the two different thermal boundary conditions. The frequency of the electric field is f = 100 kHz. In both cases, Joule heating is concentrated near the electrodes where the field strengths are at the maximum. Under BC-1, the maximum temperature is found near the top of the microchannel due to poor thermal conductivity of the glass cover. In contrast, the highest fluid temperature under BC-2 occurs in the region close to the electrodes, since the convection thermal resistances are equal on both the top and the bottom surfaces of the microchannel. It is noted that the temperature variation across the microchannel height is minuscule (~ 0.01 K), however, the resulting temperature gradient is sufficient (200 K/m) to induce EHD flows [157].

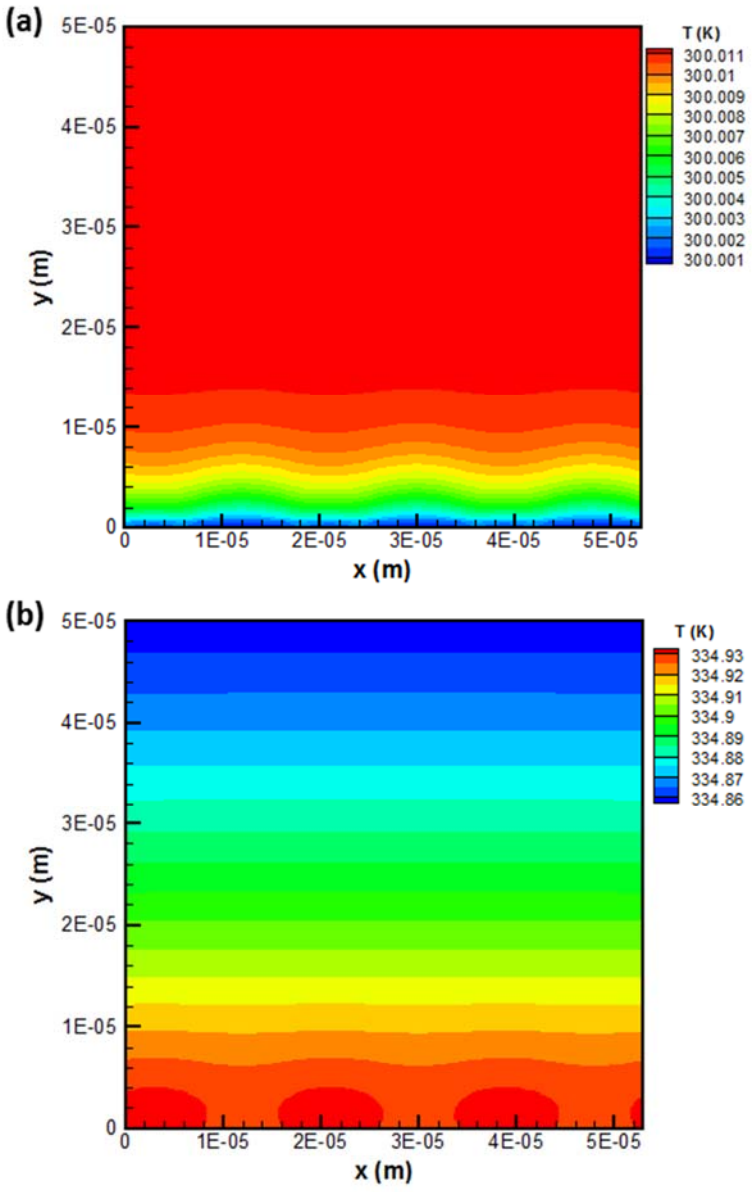

Figure 41. The temperature fields under (a) BC-1 and (b) BC-2 (at V_0 = 10 V and f = 100 kHz).

Figure 42 illustrates the calculated EHD velocity vectors at various streamwise locations. As expected, attraction-type EHD occurs under BC-1 and the flow velocity follows the direction of the traveling wave (Figure 42(a)), i.e., going from the left to right, whereas repulsion-type EHD arises under BC-2 and the flow is against the traveling wave (Figure 42(b)).

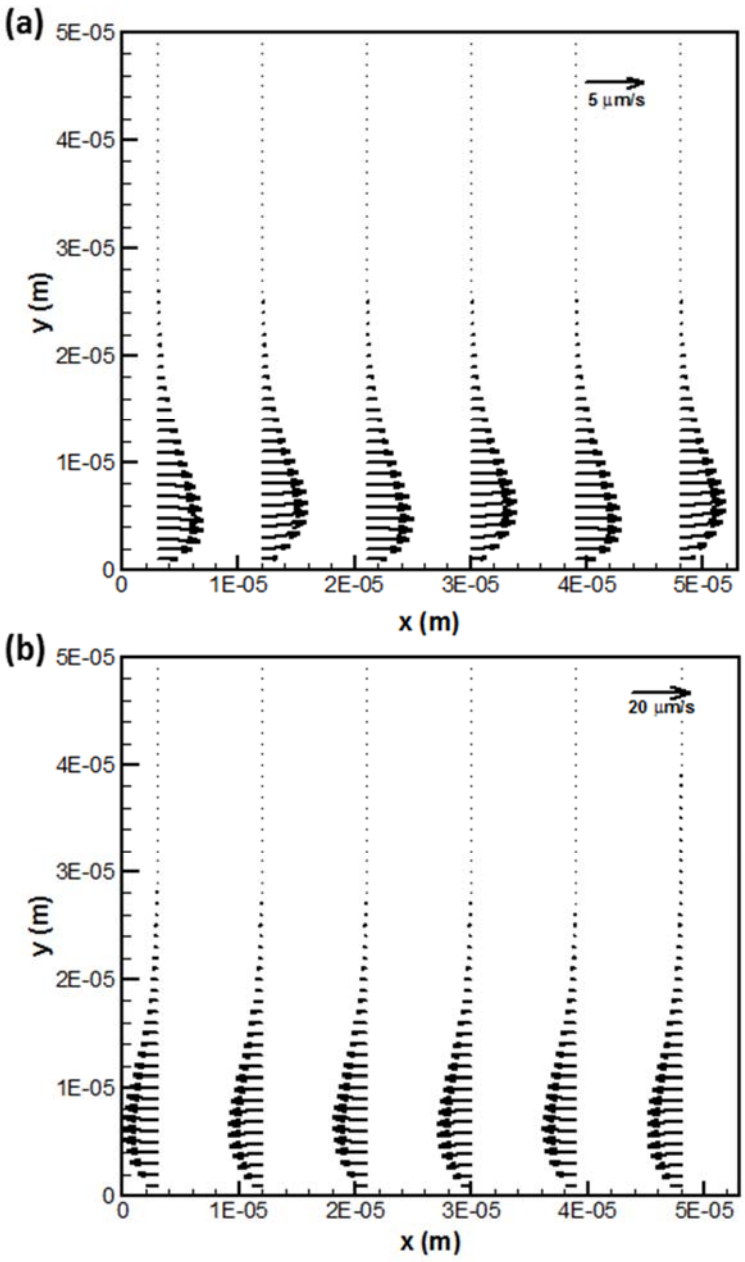

Figure 42. The EHD velocity vectors at various streamwise locations.

Figure 43 illustrates the comparison of the EHD velocity for three different frequencies at the midway location of the flow channel (x = 30 μm). It is known that the maximum EHD effect occurs at the relaxation frequency of the KCl solution, f_c = 122 kHz. At lower frequencies, the induced charges will decay during the long residence time and

the EHD force exerted in the fluid is small. If the frequency is too high, the charges will not be able to fully transit from one electrode to the next before the voltages on the electrodes change, again reducing the EHD force [147].

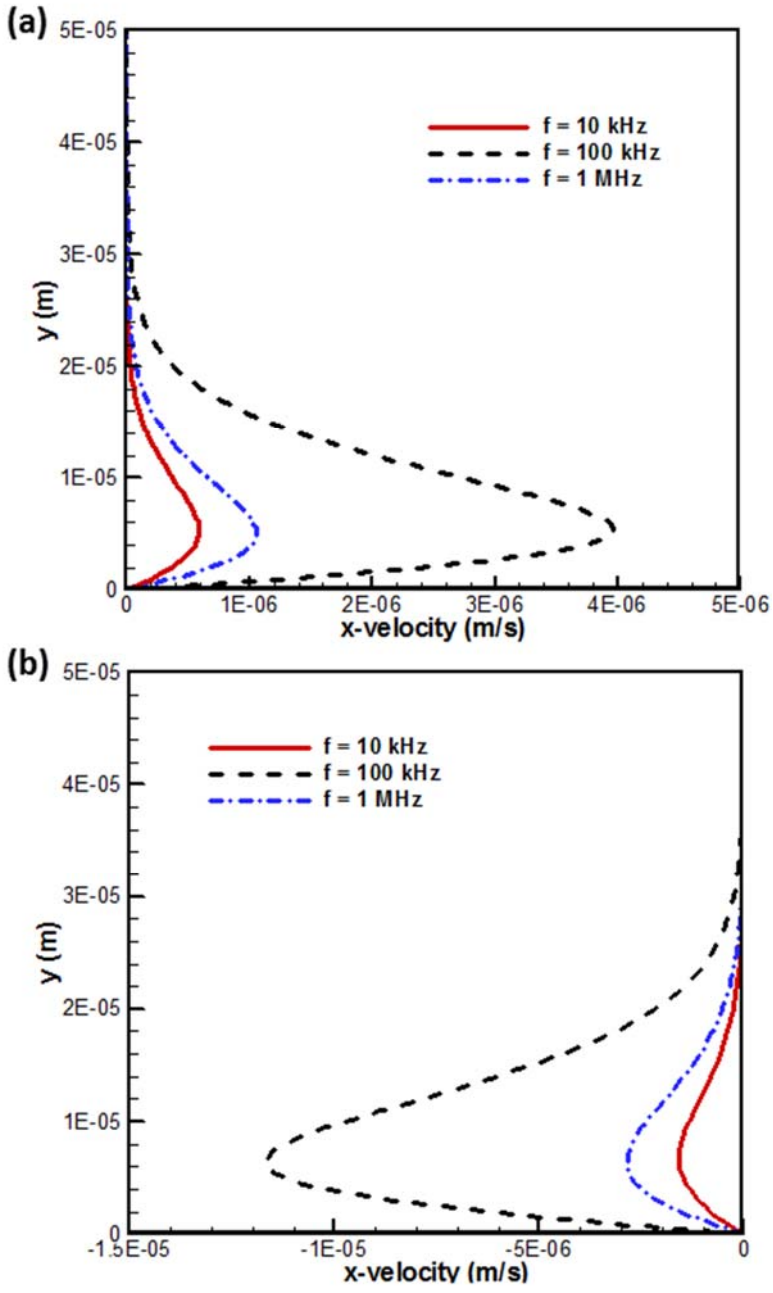

Figure 43. Comparison of the EHD velocity at the streamwise location x = 30 μm.

The results in Figure 43 show that, in both repulsion-type and attraction-type EHD, the fluid velocity rises up drastically when the frequency is increased from 10 kHz to 100 kHz (close to the optimal frequency of 122 kHz), and decreases rapidly with further increasing the frequency to 1 MHz. The maximum velocity in the repulsion-type EHD (~ 12 μm/s) is about three times that in the attraction-type EHD (~ 4 μm/s). This is consistent with the greater temperature gradient observed under BC-2 (as shown in Figure 41), which leads to a stronger EHD driving force.

6.4.3 Dielectrophoresis

The DEP-induced velocity fields in the microchannel are shown in Figure 44(a). Since $\mathrm{Im}(f_{CM}) < 0$, the DEP flow is opposite to the direction of the traveling wave. Velocity profiles at various streamwise locations resemble the asymmetric shape of the EHD flows, however, reverse flows are found in the near-wall area. Flow velocities at x = 30 μm are plotted in Figure 44(b) for the applied frequencies of 10 kHz, 100 kHz and 1 MHz, respectively.

It can be seen that the maximum velocity occurs at f = 100 kHz, which is close to the Maxwell-Wagner relaxation frequency, $f_{M\text{-}W}$ = 126 kHz for the fluid-particle combination used in this work. The velocity reductions at the lower and higher frequencies (10 kHz and 1 MHz) are due to the decreased values of $\mathrm{Im}(f_{CM})$ in both frequency ranges (as shown in Figure 37).

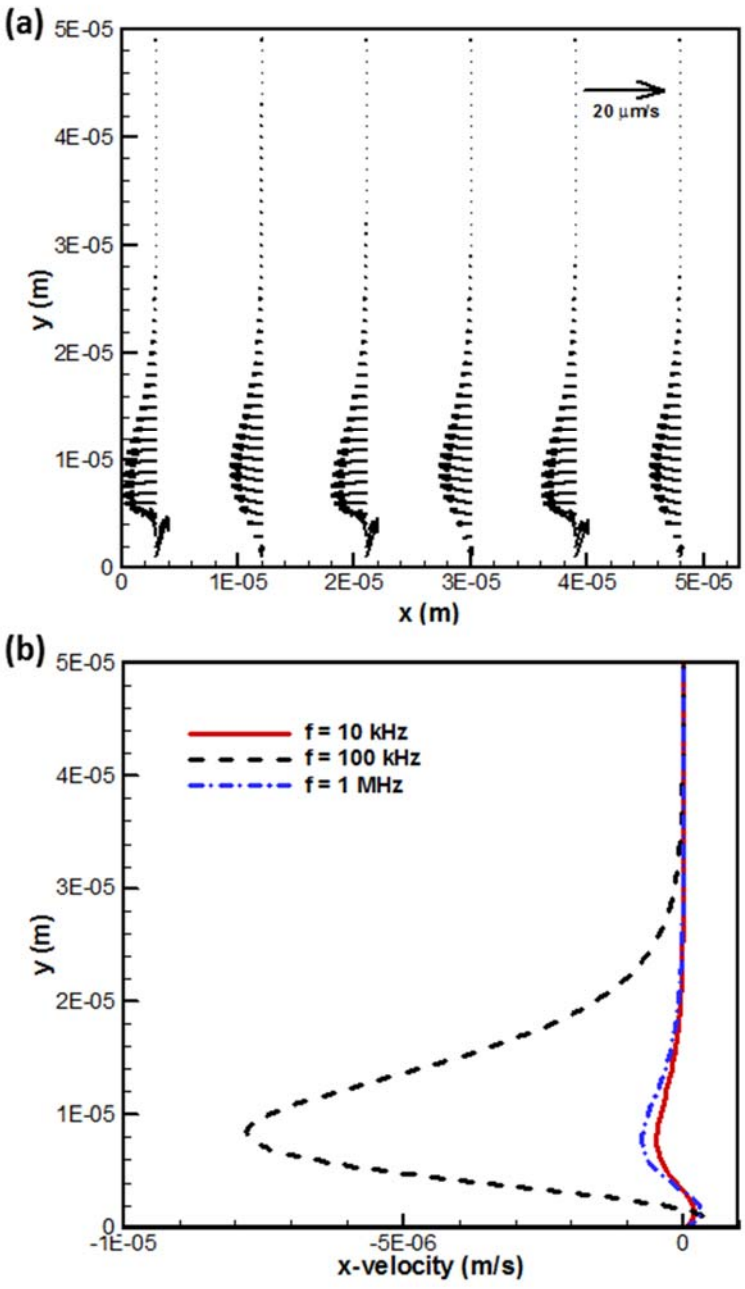

Figure 44. (a) The twDEP velocity vector field and (b) the twDEP velocity profile at x = 30 μm.

6.4.4 EHD and twDEP

The simulation results in Figure 43 and Figure 44 suggest that EHD and twDEP operating in the same frequency range can simultaneously induce flow fields of a comparable velocity magnitude. The direction of the net flow depends on the relative directions of the individual flows with respect to that of the applied field. Figure 45 shows the velocity profile at the streamwise location x = 30 μm when the DEP-induced and EHD-induced flow fields are superimposed. In Figure 45(a), the repulsion-type EHD and the twDEP act in the same direction (from the right to left), both contributing synergistically to the net flow. This is evidenced by the increase in the maximum velocity at all three frequencies.

Figure 45(b) depicts that, when the attraction-type EHD competes with the twDEP, the net flow field will be suppressed. For instance, at f = 100 kHz, the maximum twDEP velocity reduce from 8 μm/s (Figure 44(b)) to 5.5 μm/s; moreover, the twDEP flow directions are totally reversed at f = 10 kHz and 1 MHz. As a consequence, when utilizing twDEP for particle manipulation or micropumping, great caution must be exercised to ensure both the frequency range of the traveling-wave field and the thermal boundary condition of the microfluidic device are appropriate so that the effects of EHD will not interfere obstructively with twDEP.

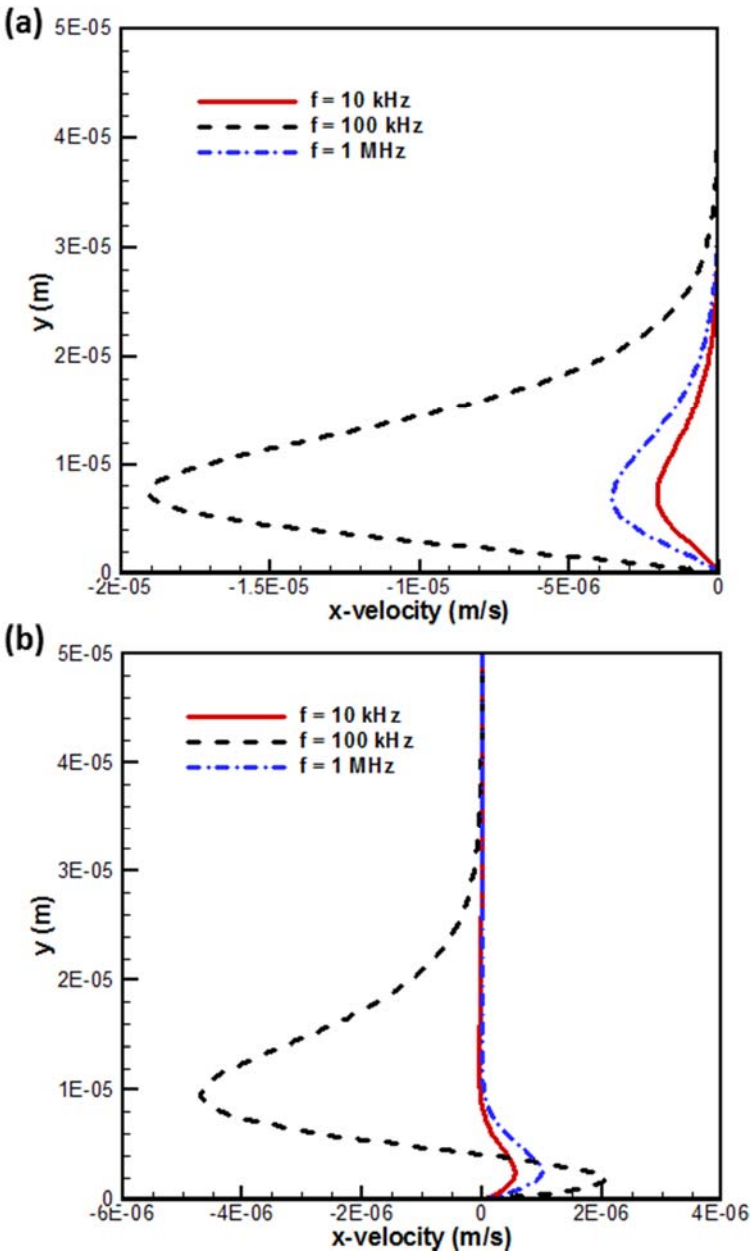

Figure 45. Velocity profile at x = 30 μm when EHD interferes with twDEP.

6.5 Conclusions

In this Chapter, the coupled EHD- and twDEP-driven flows were studied numerically in a microchannel. The EHD flow was caused by the Joule heating effect in the electrolyte solution. Both the repulsion-type EHD and the attraction-type EHD were considered, each determined by the corresponding thermal boundary condition. The flow field due to twDEP was solved using an equivalent mixture model and the calculated flow velocity was compared to that induced by EHD. The results show, depending on the frequency range of the traveling-wave field and the thermal boundary condition, the EHD-induced flow and the twDEP-induced flow can work either synergistically or competitively.

Chapter 7 Electrorotation

7.1 Introduction

In this Chapter, another powerful tool to manipulate micro/nanoparticles with dielectrophoresis, electrorotation (ROT), will be introduced. This technique shares some similarities with traveling-wave dielectrophoresis, except that the phase-shifting electric field is applied to electrodes that arranged in a loop configuration. Electrorotation was firstly discovered in 1892 by Arno [162], who reported that small particles can be made to spin when placed in a rotating electric field. This phenomenon was then named as the Born-Lertes effect [163-165]. Pickard analyzed ROT by using the concepts of dielectric loss and effective conductivity, and constructed a theoretical curve to characterize the relationship between the ROT torque and the frequency of the applied field [166]. The first electrorotation experiment of cells was conducted by Holzapfel [167] to demonstrate the dependence of the speed of rotation of mesophyll protoplast cells of Avena sativa on the field intensity. The cellular rotational speed increases with the square of the electric field.

The electrokinetic method of electrorotation (ROT), where 90-degree phase-shifted fields are applied to four neighboring electrodes to rotate particles in a co-field or counter-field manner, depending on the angle between the induced dipole and the rotating electric field, has been demonstrated as a powerful, nondestructive, and label-free method for determining the dielectric properties of cells from their rotational frequency spectra [52, 168, 169]. Electrorotation has become a very powerful tool to study cells [47], DNA [49, 170] and bioparticles [171] based on the electric polarizability and conductivities [172,

173]. Current studies for electrorotation focus primarily on obtaining analytical solutions of the dynamics of a single particle or collecting experimental data for the separation/concentration of bioparticles. There is very little information on the quantitative understanding of particle dynamics when multiple particles are involved.

Accordingly, in this Chapter, the DLM/FD method and the MST approach are used together to simulate the nanoparticles electrorotation in an external rotating electric field. The DEP force and torque acting on the particles are calculated by integrating Maxwell stress tensor over the surface of each particle. Then, the DLM/FD method is applied to solve the particle-particle and particle-fluid hydrodynamic interactions. In addition, microfluidic experiments are conducted to observe the rotation of two and eight microparticles with diameter of 3.2 μm, respectively, under a rotating electric field. The numerical simulation results of the trajectory and the final steady motion of the particles are compared to the experimental data, and very good agreements have been found.

7.2 Theory of Electrorotation

The theory of electrorotation is very similar to the traveling-wave dielectrophoresis discussed in the previous Chapters. For convenience, we briefly summaries here the theoretical background of the electrorotation motion. As shown in Figure 46, the electrodes are fabricated at the four corners of a silicon wafer. The study only concerns the particle motion in the x-y plane whereas the vertical movement in the z direction will be not considered.

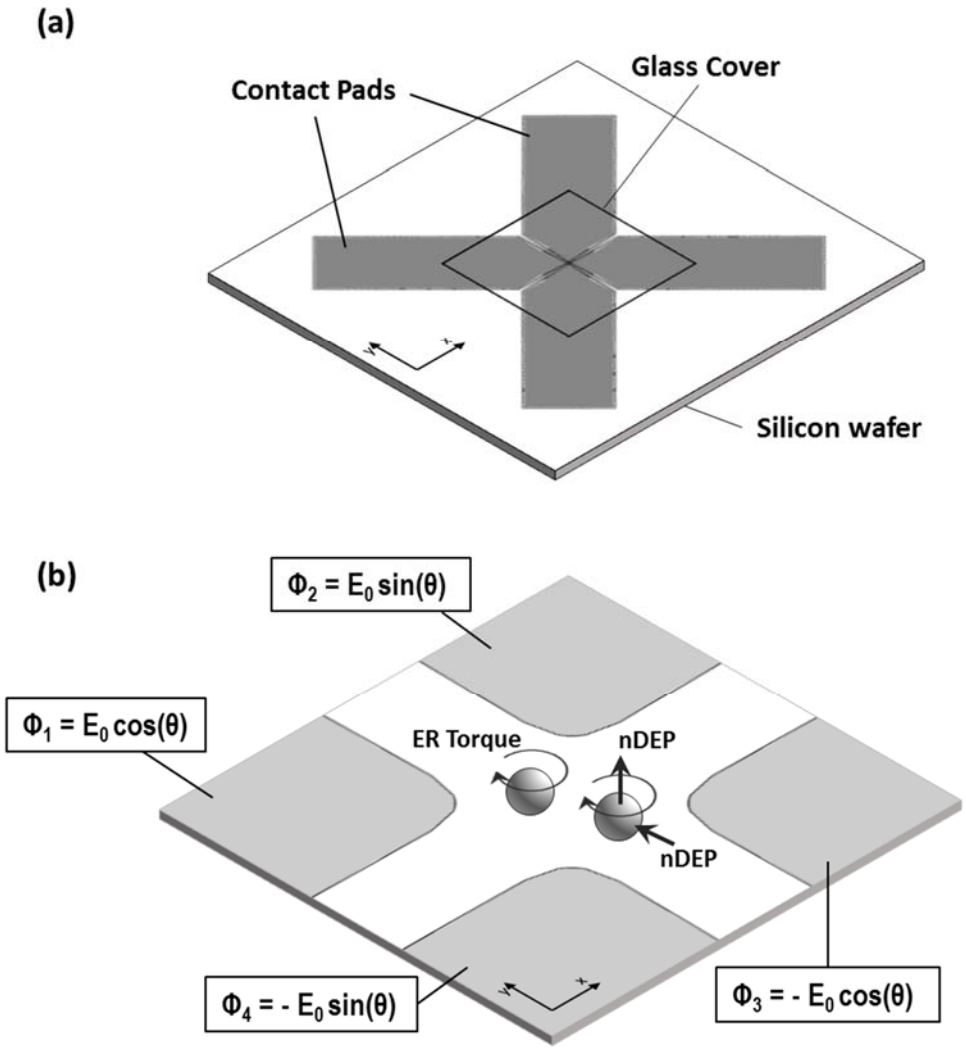

Figure 46. A sketch of the electrorotation device.

As described in previous Chapters, a single dielectric particle suspended in a medium in a non-uniform electric field experiences dielectrophoretic force. The analytical expression of the dipole moment and the dielectrophoretic force are

$$\vec{p} = 4\pi a^3 \varepsilon_m \left(\frac{\tilde{\varepsilon}_p - \tilde{\varepsilon}_m}{\tilde{\varepsilon}_p + 2\tilde{\varepsilon}_m} \right) \vec{E} \quad \text{and} \tag{141}$$

$$\vec{F}_{DEP} = 2\pi a^3 \varepsilon_m \left(\mathrm{Re}[\, f_{CM}\,] \nabla \vec{E}^2 - 2\,\mathrm{Im}[\, f_{CM}\,] \left(\nabla \times \left(\mathrm{Re}[\vec{E}] \times \mathrm{Im}[\vec{E}] \right) \right) \right) , \qquad (142)$$

where the Clausius-Mossotti factor f_{CM} is given by

$$f_{CM} = \frac{\tilde{\varepsilon}_p - \tilde{\varepsilon}_m}{\tilde{\varepsilon}_p + 2\tilde{\varepsilon}_m} \ . \qquad (143)$$

For a polystyrene particle suspended in DI water ($\sigma_p > \sigma_m$ and $\varepsilon_p < \varepsilon_m$), Re[fCM] is positive at low frequencies and negative at high frequencies. In order to observe the sustained electrorotation, the particles should experience negative DEP force in order to be repelled away from the electrodes as shown in Figure 46(b).

As introduced before, the DEP forces and torques are computed through a surface integral of the Maxwell stress tensor

$$\left\langle \vec{F}_{DEP}^{MST} \right\rangle = \frac{1}{4} \mathrm{Re}[\tilde{\varepsilon}] \oint \left(\vec{E}\vec{E}^* + \vec{E}^*\vec{E} - \left|\vec{E}\right|^2 \vec{I} \right) \cdot \vec{n} dA \quad \text{and} \qquad (144)$$

$$\left\langle \vec{\tau}_E \right\rangle = \frac{1}{4} \mathrm{Re}[\tilde{\varepsilon}] \oint \vec{r} \times \left(\vec{E}\vec{E}^* + \vec{E}^*\vec{E} - \left|\vec{E}\right|^2 \vec{I} \right) \cdot \vec{n} dA \ . \qquad (145)$$

The motion of particles and fluid are solved by the DLM/FD method as we discussed before.

7.3 Numerical Simulation

Numerical results of the electric potential are shown in Figure 47. The real components of the electric potential ϕ_R and the imaginary components ϕ_I are shown in Figure 47(a) and (b), respectively. Since the density of the field lines is proportional to the

strength of the electric field $E = \sqrt{\left|\nabla \phi_R{}^2\right| + \left|\nabla \phi_I{}^2\right|}$, the maxima of the electric field E appears at the edges of the electrodes and decay exponentially with increasing distance from the edges, as shown in Figure 48.

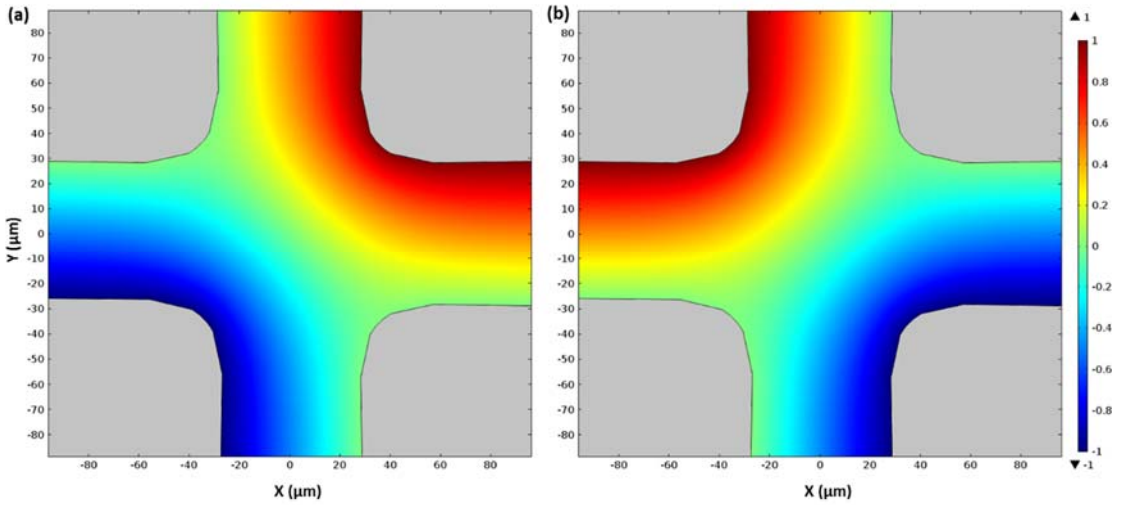

Figure 47. Distribution of the electric potential and field lines (a) ϕ_R and (b) ϕ_I.

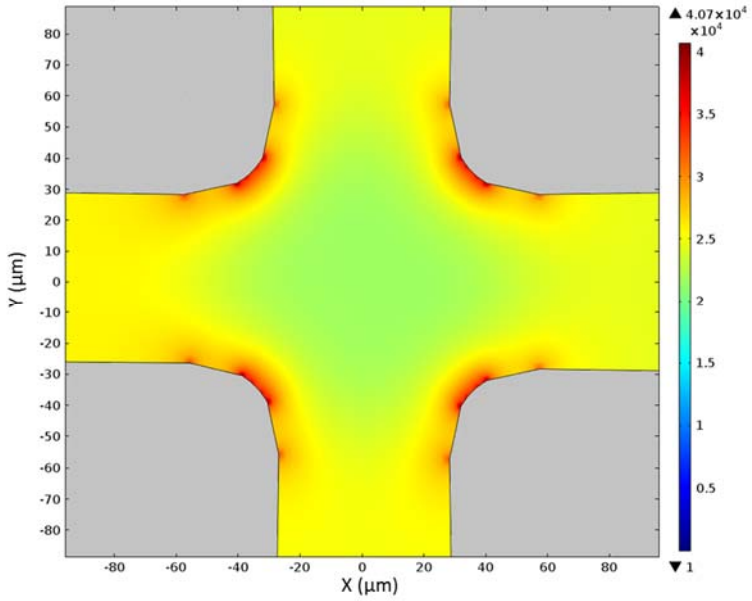

Figure 48. Magnitude of the electric field using logarithmic scale.

As discussed in Chapter 2, the dielectrophoretic force can be expressed as

$$\vec{F}_{DEP} = 2\pi a^3 \varepsilon_m \left(\mathrm{Re}\left[f_{CM} \right] \vec{\nabla}^2 \left| \vec{E} \right|^2 + 2\,\mathrm{Im}\left[f_{CM} \right] \left(E_x{}^2 \vec{\nabla}\varphi_x + E_y{}^2 \vec{\nabla}\varphi_y \right) \right) , \qquad (146)$$

where Re[f_{CM}] and Im[f_{CM}] denote the real and imaginary parts of f_{CM}, and E_x and E_y are components of the electric field vector; φ_x and φ_y are the phase angles since the electric field is spatially phase-shifted. As discussed in Chapter 5, the alignment of the twDEP force with the applied field is contingent upon the Clausius-Mossotti factor f_{CM}, which is frequency-dependent. Re[f_{CM}] is positive in the low-frequency range (f < 1 kHz) in which the particles are more polarizable than the surrounding fluid, and crosses over to negative values as the frequency increases (f > 100 kHz) and the particles become less polarizable than the fluid. If Re[f_{CM}] > 0, the regular DEP force component aligns favorably with the field strength gradient, as indicated by Eq. (146). As a result, the particles move towards the maxima of the electric field, which are usually located at the edges of the electrodes that are used to generate the electric field, and positive DEP occurs. In the opposite situation, a negative Re[f_{CM}] brings negative DEP where the particles move away from the maxima of the electric field, distancing themselves from the electrodes.

Im[f_{CM}] vanishes at both extremes of the frequency spectrum but assumes non-zero values in the mid-range around the cross-over frequency. When Im[f_{CM}] is not trivial, the resulting rotational DEP force in Eq. (146) propels the particles against the rotating electric field.

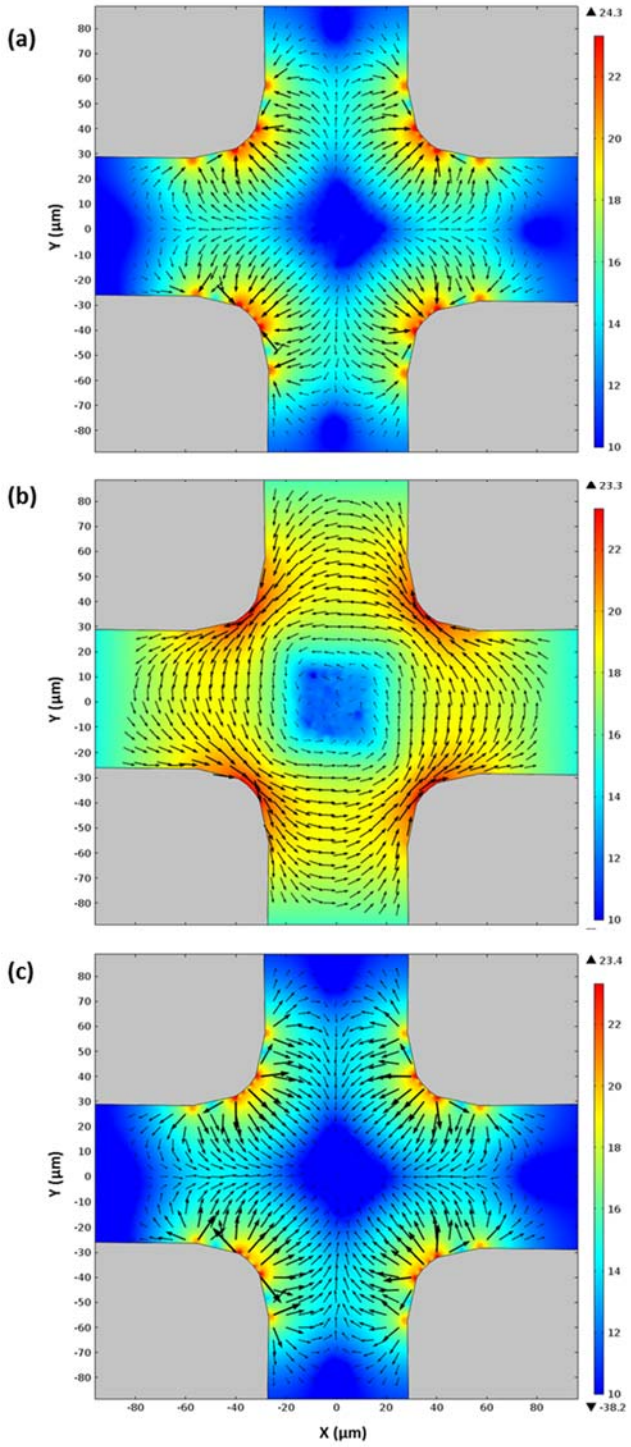

Figure 49. Magnitude of the DEP force at different frequencies using logarithmic scale.

The Re[f_{CM}] and Im[f_{CM}] terms related components of the DEP force at different driving frequencies can be distinguished in Figure 49. It shows the vector fields of the DEP force at (a) low, (b) moderate and (c) high frequency range. Clearly, Figure 49(a) and (c) present the positive DEP and negative DEP, respectively. As shown in the vector plots, the direction of the forces are towards or outwards the electrodes edges, and the magnitude of the force increases exponentially near the edges. Figure 49(b) represents the DEP force field at the frequency of 10 kHz.

The normalized electrorotation torque at 10 kHz is shown in Figure 50. The maximum of the torque occurs uniformly in the center of the domain. The sign of the torques are all positive in Figure 50, suggesting that most of the particles suspended will spin in the same direction with equal speed.

In this work, the DEP force and torque on a particle are obtained via integrating the Maxwell stress tensor over the surface of the particle, as discussed in Chapter 2. Hence, the details are skipped here.

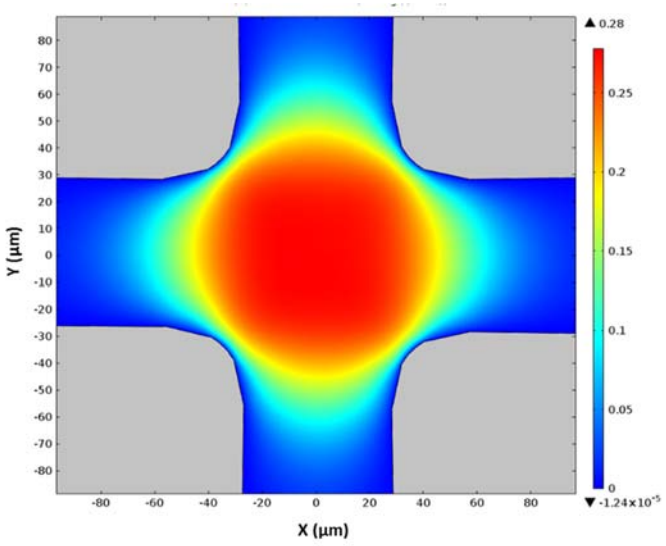

Figure 50. Normalized electrorotation torque at f = 10 kHz.

7.4 Experiments

In order to validate the numerical simulation results, an experimental apparatus is designed and constructed to perform electrorotation directed fluidic self-assembly of microparticles. The setup consists of a microfluidic chip, a fluorescent microscope, and an imaging system, the same as used in Chapter 4. The microfluidic chip consists of an array of four electrodes fabricated using photolithography. The microfabrication process is also the same as introduced in Chapter 4.

The electrodes and the contact pads on the silicon wafer can be seen from top view in Figure 51(a). Under a microscope with 20x magnification, Figure 51(b) clearly shows that the distance between two opposite electrodes is 50 μm. With a 50x magnification, the details of the electrodes is shown in Figure 51(c).

The colloidal solution is prepared by mixing fluorescent polystyrene particles of 3.2 μm diameter (Thermo Scientific, CA) with deionized (DI) water. The conductivities of polystyrene and DI water are measured to be 5×10^{-5} S/m and 5.5×10^{-6} S/m; while the relative dielectric permittivity are 2.8 and 78.4, respectively. The colloidal solution contains 0.2 wt% solids, resulting in a mixture density of 1.05 g/cm^3.

During the experiments, the microfluidic chip is mounted to a probe station, and the electrodes are connected to an AC arbitrary waveform function generator (FLUKE 294). Sinusoidal wave signals are generated and applied to the electrodes. The applied voltage is set to be 5 V to 10 V and the frequency to be 10 kHz, so that the particles rotate at a reasonable angular speed. Refer to Chapter 4 for other devices.

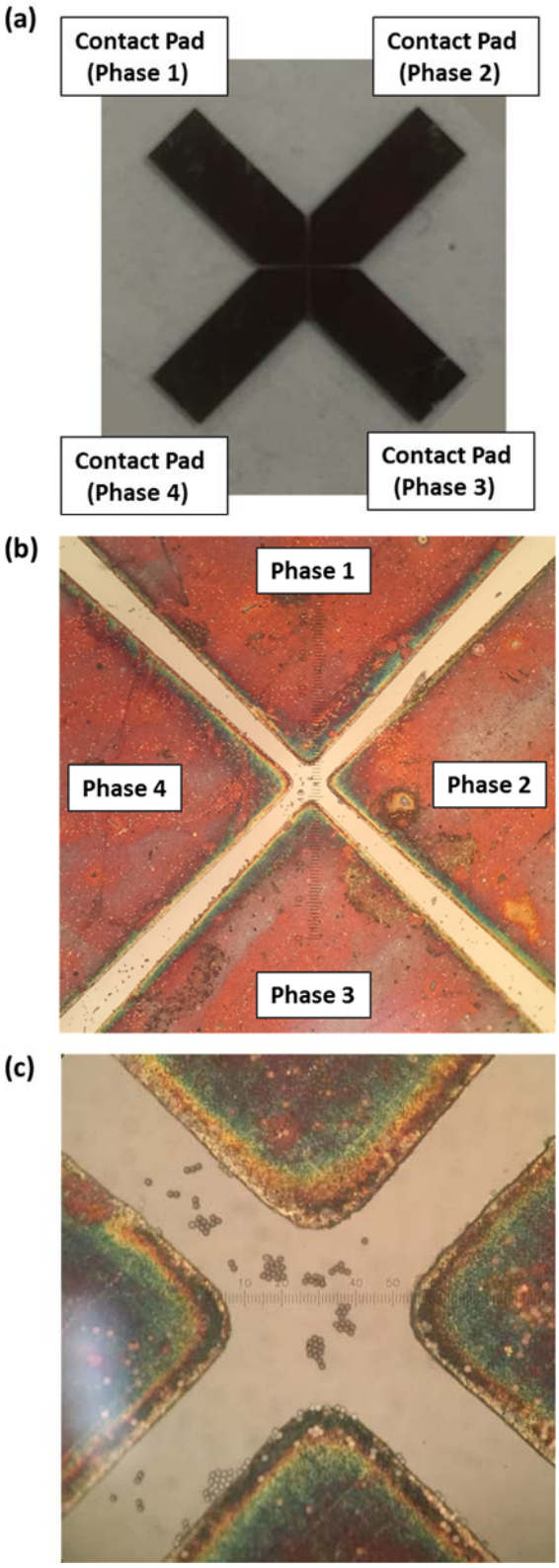

Figure 51. Prototype electrorotation device with electrodes on a silicon wafer.

7.5 Results and Discussion

In this section, the numerical and experimental results will be presented for electrorotation directed self-assembly of two and eight polystyrene particles suspended in DI water, respectively. Both the patterns and the trajectories of the particles will be compared and discussed.

7.5.1 Electrorotation Assembly of Two Particles

For the experiments, two particles, which are at sufficient distance from all the surrounding particles, have been carefully selected to ensure that they are isolated from the hydrodynamic and electrical interactions with their closest neighbors. In Figure 52(a), the initial positions of the two particles are (22.71, 30.79) and (9.62, 17.84) in terms of pixels. This indicates the initial angle between the line connecting the centers of the particles and the horizontal line is $\theta = 44.7°$. According to the forgoing analysis in Section 7.3, these two particles experience a rorational force along the direction of the rotating electric field and a torque. To examine the subsequent motion of the partiecles, their trajectories are illustrated in Figure 53, where both the measured instaneous particle locations and the simulated trajectories are shown as circles and dash lines, respectively. After $t = 1.9$ s, the two particles touch each other and then rotate as a unity at a constant angular speed. From the comparison in Figure 53, it can be concluded that the particle trajectories obtained from from the numerical simulations agree perfectly with the experimental measurements.

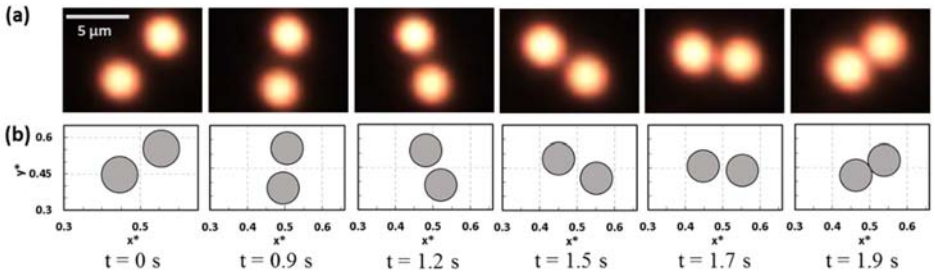

Figure 52. Experimental (a) and Numerical (b) results of electrorotation assembly of two particles.

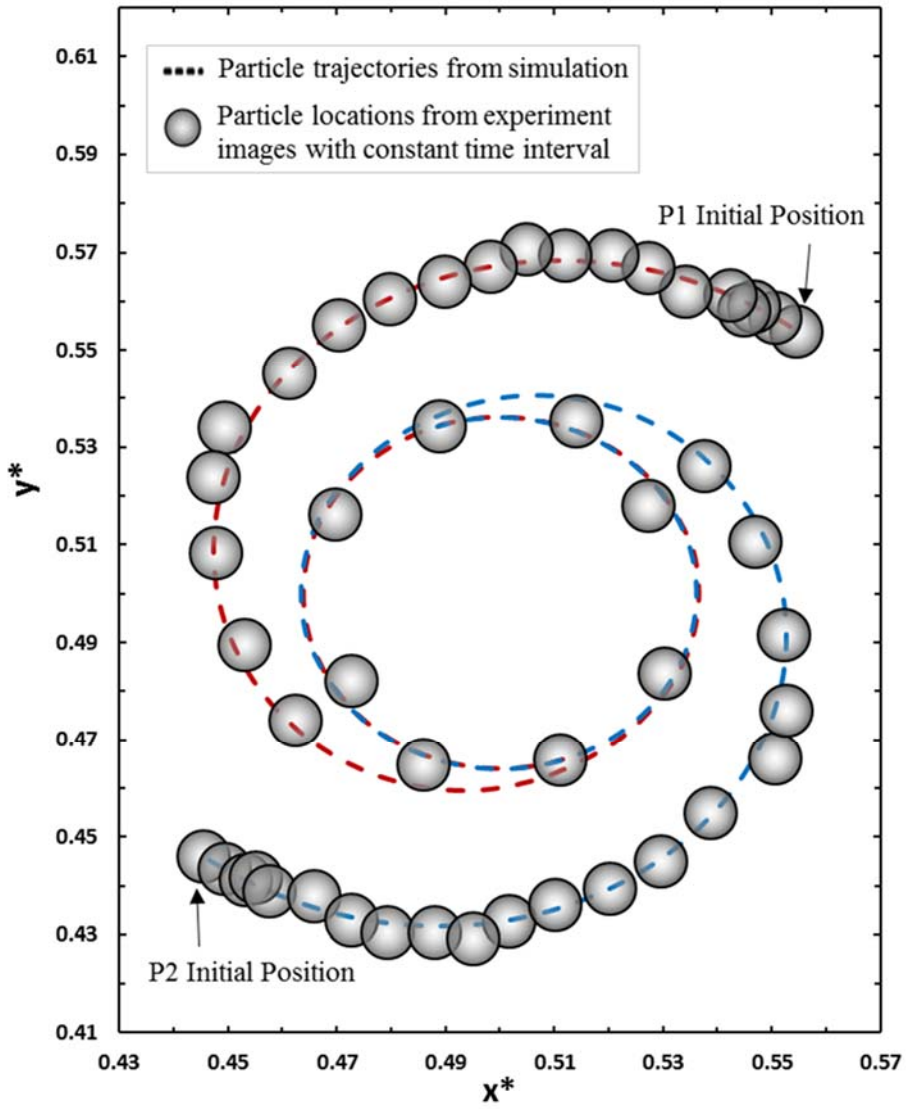

Figure 53. Comparison of trajectories of two particles from experiments and simulation.

7.5.2 Electrorotation Assembly of Eight Particles

Similarly to the case of two particles, electrorotation directed self-assembly of eight particles is also investigated to validate the numerical models. The reason to select this combination is that when the particle aggregation is completed, there exists an outer particle, which indicates the direction of the particle aggregation.

As shown in Figure 54(a), at t = 0 s, the eight particles are located at are (37.0, 55.1), (45.0, 32.0), (52.4, 73.5), (59.2, 52.9), (68.5, 29.0), (76.9, 70.0), (84.6, 46.9) and (101.0, 64.9), respectively. At this moment, the angle of the outer particle with reference to the center point (0.5, 0.5) is $\theta = -16.0°$. After 0.2 s, the aggregation rotates to $\theta = 32.2°$. As a result of a constant rotating speed, at t = 1.0 s, this aggregation rotated $\Delta\theta = 336°$, compare to the initial position. The trajectories of the outer particle in experiments and numerical simulations can be observed in Figure 55. A very good agreement can be found between the experimental data and the numerical simulation results.

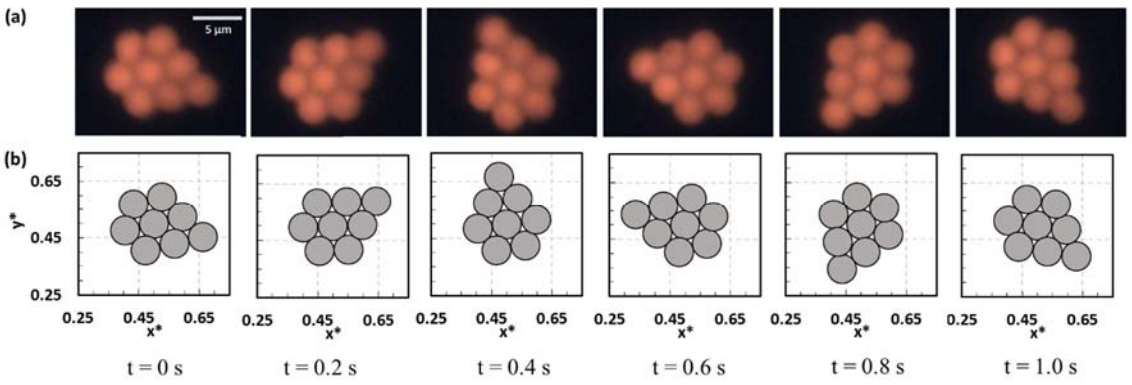

Figure 54. Experimental (a) and Numerical (b) results of electrorotation assembly of eight particles.

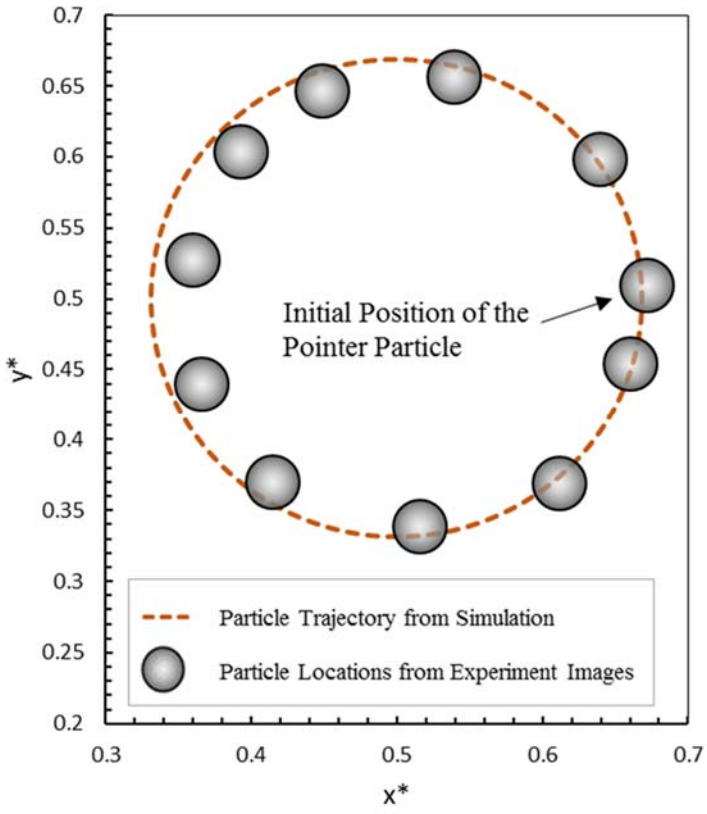

Figure 55. Comparison of trajectories of the outer particle from experiments and simulation.

7.6 Conclusions

In this Chapter, the rotating electric field induced electrorotation is analyzed in details. Electrorotation directed self-assembly of multiple particles (two and eight particles) into a constantly rotating aggregation is investigated both experimentally and numerically. The particle-fluid and particle-particle interactions are accurately captured by the numerical simulation with the Distributed Lagrange-multiplier based fictitious-domain method (DLM/FD). Numerical simulations show good agreement with experiments, in terms of both the particle patterns for each time frame and the trajectory of each single particle.

Chapter 8 Conclusions and Future Work

8.1 Conclusions

To cope with challenges arising from the dielectrophoresis-directed fluidic assembly of nanoparticles, the fundamentals of the fluid-particle electrohydrodynamic interactions are investigated in this dissertation.

First, an accurate and efficient numerical framework is established to simulate the movement and aggregation of multiple particles undergoing DEP and to investigate the effect of various system parameters on the DEP-directed fluidic assembly. The numerical models are developed by combining the Maxwell Stress Tensor (MST) approach and the Distributed Lagrange Multiplier/Fictitious Domain (DLM/FD) method. As compared to the existing methods, the MST approach ensures the DEP forces/torques on the particle are correctly calculated even in regions with strong gradients such as in the vicinity of the electrodes, and can be easily applied to model particles of irregular shapes. The DLM/FD method solves the hydrodynamics by reformulating the fluid-particle problem in the fictitious domain and adopting structured, regular meshes to significantly improve the computational efficiency. Subsequently, three major fluidic assembly mechanisms, namely, pearl chaining, twDEP and electrorotation, are studied in details with the numerical models developed. The key features, such as the particle motion and the equilibrium pattern structure, of the DEP-directed fluidic assembly process are characterized. To verify the numerical results, microfluidic experiments are also conducted in this work with colloidal suspensions, in which the DEP motion of particles is recorded, analyzed and compared with the numerical simulations.

In conclusion, the numerical framework developed in this work provides a powerful tool to further investigate the motion and interaction of micro/nanoparticles in DEP-directed fluidic assembly applications. It will help to lay the scientific foundation for large-scale parallel manufacturing of functional micro/nanostructures for engineering applications.

8.2 Future Work

The direct numerical simulation framework developed in this work shows great promise for studying DEP-directed fluidic assembly of micro/nanoparticles, however, the current results are restricted to 2D configurations of the modeling system. In future work, this numerical framework can be extended to more realistic 3D simulations. In addition, it is expected that the numerical scheme can be applied to simulate DEP of soft particles, which represents another important application in biological and biomedical engineering. Lastly, innovative experiments with improved device design can provide enormous possibilities to manipulate particles of various shape and material origin.

REFERENCES

1. Martel, R., T. Schmidt, H.R. Shea, T. Hertel, and P. Avouris, *Single- and multi-wall carbon nanotube field-effect transistors.* Applied Physics Letters, 1998. **73**(17): p. 2447-2449.

2. Duan, X.F., Y. Huang, Y. Cui, J.F. Wang, and C.M. Lieber, *Indium phosphide nanowires as building blocks for nanoscale electronic and optoelectronic devices.* Nature, 2001. **409**(6816): p. 66-69.

3. Zheng, G.F., W. Lu, S. Jin, and C.M. Lieber, *Synthesis and fabrication of high-performance n-type silicon nanowire transistors.* Advanced Materials, 2004. **16**(21): p. 1890-+.

4. Bachtold, A., P. Hadley, T. Nakanishi, and C. Dekker, *Logic Circuits with Carbon Nanotube Transistors.* Science, 2001. **294**(5545): p. 1317-1320.

5. Javey, A., Q. Wang, A. Ural, Y.M. Li, and H.J. Dai, *Carbon nanotube transistor arrays for multistage complementary logic and ring oscillators.* Nano Letters, 2002. **2**(9): p. 929-932.

6. Kaul, A.B., E.W. Wong, L. Epp, and B.D. Hunt, *Electromechanical Carbon Nanotube Switches for High-Frequency Applications.* Nano Letters, 2006. **6**(5): p. 942-947.

7. Cha, S.N., J.E. Jang, Y. Choi, G.A.J. Amaratunga, D.J. Kang, D.G. Hasko, J.E. Jung, and J.M. Kim, *Fabrication of a nanoelectromechanical switch using a suspended carbon nanotube.* Applied Physics Letters, 2005. **86**(8).

8. Vijayaraghavan, A., S. Blatt, D. Weissenberger, M. Oron-Carl, F. Hennrich, D. Gerthsen, H. Hahn, and R. Krupke, *Ultra-large-scale directed assembly of single-walled carbon nanotube devices.* Nano Letters, 2007. **7**(6): p. 1556-1560.

9. Pohl, H., *The motion and precipitation of suspensoids in divergent electric fields.* Journal of Applied Physics, 1951. **22**: p. 869.

10. Morgan, H., M.P. Hughes, and N.G. Green, *Separation of submicron bioparticles by dielectrophoresis.* Biophysical Journal, 1999. **77**(1): p. 516-525.

11. Pethig, R., *Dielectrophoresis: An assessment of its potential to aid the research and practice of drug discovery and delivery.* Advanced Drug Delivery Reviews, 2013. **65**(11-12): p. 1589-1599.

12. Gangwal, S., O.J. Cayre, and O.D. Velev, *Dielectrophoretic Assembly of Metallodielectric Janus Particles in AC Electric Fields.* Langmuir, 2008. **24**(23): p. 13312-13320.

13. Huang, Y., X.F. Duan, Q.Q. Wei, and C.M. Lieber, *Directed assembly of one-dimensional nanostructures into functional networks.* Science, 2001. **291**(5504): p. 630-633.

14. Rao, S.G., L. Huang, W. Setyawan, and S.H. Hong, *Large-scale assembly of carbon nanotubes.* Nature, 2003. **425**(6953): p. 36-37.

15. Hermanson, K.D., S.O. Lumsdon, J.P. Williams, E.W. Kaler, and O.D. Velev, *Dielectrophoretic assembly of electrically functional microwires from nanoparticle suspensions.* Science, 2001. **294**(5544): p. 1082-1086.

16. Wang, X.J., X.B. Wang, and P.R.C. Gascoyne, *General expressions for dielectrophoretic force and electrorotational torque derived using the Maxwell stress tensor method.* Journal of Electrostatics, 1997. **39**(4): p. 277-295.

17. Zhang, L., A. Gerstenberger, X. Wang, and W.K. Liu, *Immersed finite element method.* Computer Methods in Applied Mechanics and Engineering, 2004. **193**(21–22): p. 2051-2067.

18. Liu, Y.L., J.H. Chung, W.K. Liu, and R.S. Ruoff, *Dielectrophoretic assembly of nanowires.* Journal of Physical Chemistry B, 2006. **110**(29): p. 14098-14106.

19. Liu, Y., W.K. Liu, T. Belytschko, N. Patankar, A.C. To, A. Kopacz, and J.H. Chung, *Immersed electrokinetic finite element method.* International Journal for Numerical Methods in Engineering, 2007. **71**(4): p. 379-405.

20. Gascoyne, P.R.C. and J. Vykoukal, *Particle separation by dielectrophoresis.* Electrophoresis, 2002. **23**(13): p. 1973-1983.

21. Hughes, M.P. and H. Morgan, *Dielectrophoretic trapping of single sub-micrometre scale bioparticles.* Journal of Physics D-Applied Physics, 1998. **31**(17): p. 2205-2210.

22. Fiedler, S., S.G. Shirley, T. Schnelle, and G. Fuhr, *Dielectrophoretic sorting of particles and cells in a microsystem.* Analytical Chemistry, 1998. **70**(9): p. 1909-1915.

23. Suehiro, J. and R. Pethig, *The dielectrophoretic movement and positioning of a biological cell using a three-dimensional grid electrode system.* Journal of Physics D-Applied Physics, 1998. **31**(22): p. 3298-3305.

24. Pohl, H.A., *Dielectrophoresis*. 1987: Cambridge university press.

25. Chen, C.S. and H.A. Pohl, *Biological Dielectrophoresis - Behavior of Lone Cells in a Nonuniform Electric-Field.* Annals of the New York Academy of Sciences, 1974. **238**(Oct11): p. 176-185.

26. Gvozdiak, P.I. and T.P. Chekhovckaia, *Electroretention of microorganisms.* Mikrobiologiya, 1976. **45**(5): p. 5.

27. Fomcenkov, V.M. and B.K. Gajriljuk, *Dielectrophoresis of Cell-Suspensions.* Studia Biophysica, 1977. **65**(1): p. 35-46.

28. Fomchenkov, V.M. and B.K. Gavrilyuk, *The study of dielectrophoresis of cells using the optical technique of measuring.* Journal of Biological Physics, 1978. **6**(1-2): p. 29-68.

29. Jones, T.B. and G.A. Kallio, *Dielectrophoretic Levitation of Spheres and Shells.* Journal of Electrostatics, 1979. **6**(3): p. 207-224.

30. Pohl, H.A. and K. Pollock, *Dielectrophoretic Cell Sorting.* Journal of the Electrochemical Society, 1983. **130**(3): p. C121-C121.

31. Groth, I., H.E. Jacob, W. Kunkel, and H. Berg, *Electrofusion of Penicillium Protoplasts after Dielectrophoresis.* Journal of Basic Microbiology, 1987. **27**(6): p. 341-344.

32. Glassy, M., *Creating hybridomas by electrofusion.* Nature, 1988. **333**(6173): p. 579-580.

33. Sukharev, S.I., I.N. Bandrina, A.I. Barbul, L.I. Fedorova, I.G. Abidor, and A.V. Zelenin, *Electrofusion of Fibroblasts on the Porous Membrane.* Biochimica Et Biophysica Acta, 1990. **1034**(2): p. 125-131.

34. Arnold, W.M. and U. Zimmermann, *Electro-Rotation - Development of a Technique for Dielectric Measurements on Individual Cells and Particles.* Journal of Electrostatics, 1988. **21**(2-3): p. 151-191.

35. Gherardi, L., E.R. Mognaschi, and A. Savini, *The Dielectrophoretic Motion of a Lossy Dielectric Sphere in a Liquid of Non-Zero Conductivity.* Ieee Transactions on Electrical Insulation, 1985. **20**(2): p. 385-388.

36. Henry, F.S. and T. Ariman, *NUMERICAL CALCULATION OF PARTICLE COLLECTION IN ELECTRICALLY ENHANCED FIBROUS FILTERS.* Particulate Science and Technology, 1986. **4**(4): p. 455-477.

37. Adamson, R.J. and K.V.I.S. Kaler, *An Automated Stream-Centered Dielectrophoretic System.* Ieee Transactions on Industry Applications, 1988. **24**(1): p. 93-98.

38. Masuda, S., M. Washizu, and T. Nanba, *Novel Method of Cell-Fusion in Field Constriction Area in Fluid Integrated-Circuit.* Ieee Transactions on Industry Applications, 1989. **25**(4): p. 732-737.

39. Washizu, M. and O. Kurosawa, *Electrostatic Manipulation of DNA in Microfabricated Structures.* Ieee Transactions on Industry Applications, 1990. **26**(6): p. 1165-1172.

40. Washizu, M., T. Nanba, and S. Masuda, *Handling Biological Cells Using a Fluid Integrated-Circuit.* Ieee Transactions on Industry Applications, 1990. **26**(2): p. 352-358.

41. Gascoyne, P.R.C., Y. Huang, R. Pethig, J. Vykoukal, and F.F. Becker, *Dielectrophoretic Separation of Mammalian-Cells Studied by Computerized Image-Analysis.* Measurement Science & Technology, 1992. **3**(5): p. 439-445.

42. Wang, X.B., Y. Huang, J.P.H. Burt, G.H. Markx, and R. Pethig, *Selective Dielectrophoretic Confinement of Bioparticles in Potential-Energy Wells.* Journal of Physics D-Applied Physics, 1993. **26**(8): p. 1278-1285.

43. Pethig, R., Y. Huang, X.B. Wang, and J.P.H. Burt, *Positive and Negative Dielectrophoretic Collection of Colloidal Particles Using Interdigitated Castellated Microelectrodes.* Journal of Physics D-Applied Physics, 1992. **25**(5): p. 881-888.

44. Wang, X.B., Y. Huang, R. Holzel, J.P.H. Burt, and R. Pethig, *Theoretical and Experimental Investigations of the Interdependence of the Dielectric, Dielectrophoretic and Electrorotational Behavior of Colloidal Particles.* Journal of Physics D-Applied Physics, 1993. **26**(2): p. 312-322.

45. Wang, X.B., R. Pethig, and T.B. Jones, *Relationship of Dielectrophoretic and Electrorotational Behavior Exhibited by Polarized Particles.* Journal of Physics D-Applied Physics, 1992. **25**(6): p. 905-912.

46. Ying, H., R. Holzel, R. Pethig, and X.B. Wang, *Differences in the Ac Electrodynamics of Viable and Nonviable Yeast-Cells Determined through Combined Dielectrophoresis and Electrorotation Studies.* Physics in Medicine and Biology, 1992. **37**(7): p. 1499-1517.

47. Pethig, R., *Review Article-Dielectrophoresis: Status of the theory, technology, and applications.* Biomicrofluidics, 2010. **4**(2).

48. Pethig, R., A. Menachery, S. Pells, and P. De Sousa, *Dielectrophoresis: A Review of Applications for Stem Cell Research.* Journal of Biomedicine and Biotechnology, 2010.

49. Chou, C.F., J.O. Tegenfeldt, O. Bakajin, S.S. Chan, E.C. Cox, N. Darnton, T. Duke, and R.H. Austin, *Electrodeless dielectrophoresis of single- and double-stranded DNA.* Biophysical Journal, 2002. **83**(4): p. 2170-2179.

50. Jones, T.B., *Basic theory of dielectrophoresis and electrorotation.* Ieee Engineering in Medicine and Biology Magazine, 2003. **22**(6): p. 33-42.

51. Holzel, R., *Electrorotation of single yeast cells at frequencies between 100 Hz and 1.6 GHz.* Biophysical Journal, 1997. **73**(2): p. 1103-1109.

52. Rohani, A., W. Varhue, Y.H. Su, and N.S. Swami, *Electrical tweezer for highly parallelized electrorotation measurements over a wide frequency bandwidth.* Electrophoresis, 2014. **35**(12-13): p. 1795-1802.

53. Korlach, J., C. Reichle, T. Muller, T. Schnelle, and W.W. Webb, *Trapping, deformation, and rotation of giant unilamellar vesicles in octode dielectrophoretic field cages.* Biophysical Journal, 2005. **89**(1): p. 554-562.

54. Batchelder, J.S., *Dielectrophoretic Manipulator.* Review of Scientific Instruments, 1983. **54**(3): p. 300-302.

55. Fuhr, G., T. Schnelle, and B. Wagner, *Traveling Wave-Driven Microfabricated Electrohydrodynamic Pumps for Liquids.* Journal of Micromechanics and Microengineering, 1994. **4**(4): p. 217-226.

56. Fuhr, G., S. Fiedler, T. Muller, T. Schnelle, H. Glasser, T. Lisec, and B. Wagner, *Particle Micromanipulator Consisting of 2 Orthogonal Channels with Traveling-Wave Electrode Structures.* Sensors and Actuators a-Physical, 1994. **41**(1-3): p. 230-239.

57. Liu, D. and S.V. Garimella, *Microfluidic Pumping Based on Traveling-Wave Dielectrophoresis.* Nanoscale and Microscale Thermophysical Engineering, 2009. **13**(2): p. 109-133.

58. Sher, L.D., *Dielectrophoresis in Lossy Dielectric Media.* Nature, 1968. **220**(5168): p. 695-&.

59. Jones, T.B., *Dielectrophoretic Force Calculation.* Journal of Electrostatics, 1979. **6**(1): p. 69-82.

60. Liu, R.M. and J.P. Huang, *Theory of the dielectrophoretic behavior of clustered colloidal particles in two dimensions.* Physics Letters A, 2004. **324**(5-6): p. 458-464.

61. Leonardi, A., G. Medoro, N. Manaresi, M. Tartagni, and R. Guerrieri, *Simulation methodology for dielectrophoresis in microelectronic lab-on-a-chip.* Iccn 2002: International Conference on Computational Nanoscience and Nanotechnology, 2002: p. 107-110.

62. Green, N.G., A. Ramos, and H. Morgan, *Numerical solution of the dielectrophoretic and travelling wave forces for interdigitated electrode arrays using the finite element method.* Journal of Electrostatics, 2002. **56**(2): p. 235-254.

63. Kadaksham, A., P. Singh, and N. Aubry, *Dielectrophoresis of nanoparticles.* Electrophoresis, 2004. **25**(21-22): p. 3625-3632.

64. Kadaksham, J., P. Singh, and N. Aubry, *Dynamics of electrorheological suspensions subjected to spatially nonuniform electric fields.* Journal of Fluids Engineering-Transactions of the Asme, 2004. **126**(2): p. 170-179.

65. Liu, W.K., Y.L. Liu, D. Farrell, L. Zhang, X.S. Wang, Y. Fukui, N. Patankar, Y.J. Zhang, C. Bajaj, J. Lee, J.H. Hong, X.Y. Chen, and H.Y. Hsu, *Immersed finite element method and its applications to biological systems.* Computer Methods in Applied Mechanics and Engineering, 2006. **195**(13-16): p. 1722-1749.

66. Ai, Y. and S.Z. Qian, *DC dielectrophoretic particle-particle interactions and their relative motions.* Journal of Colloid and Interface Science, 2010. **346**(2): p. 448-454.

67. House, D.L., H.X. Luo, and S.Y. Chang, *Numerical study on dielectrophoretic chaining of two ellipsoidal particles.* Journal of Colloid and Interface Science, 2012. **374**: p. 141-149.

68. Kang, S. and R. Maniyeri, *Dielectrophoretic motions of multiple particles and their analogy with the magnetophoretic counterparts.* Journal of Mechanical Science and Technology, 2012. **26**(11): p. 3503-3513.

69. Hossan, M.R., R. Dillon, A.K. Roy, and P. Dutta, *Modeling and simulation of dielectrophoretic particle-particle interactions and assembly.* Journal of Colloid and Interface Science, 2013. **394**: p. 619-629.

70. Jones, T.B., *Electromechanics of particles*. 2005: Cambridge University Press.

71. Morgan, H., A.G. Izquierdo, D. Bakewell, N.G. Green, and A. Ramos, *The dielectrophoretic and travelling wave forces generated by interdigitated electrode arrays: analytical solution using Fourier series.* Journal of Physics D-Applied Physics, 2001. **34**(10): p. 1553-1561.

72. Morgan, H. and N.G. Green, *AC Electrokinetics: colloids and nanoparticles*. 2003: Research Studies Press Ltd

73. Wang, X.J., X.B. Wang, F.F. Becker, and P.R.C. Gascoyne, *A theoretical method of electrical field analysis for dielectrophoretic electrode arrays using Green's theorem.* Journal of Physics D-Applied Physics, 1996. **29**(6): p. 1649-1660.

74. Clague, D.S. and E.K. Wheeler, *Dielectrophoretic manipulation of macromolecules: The electric field.* Physical Review E, 2001. **64**(2).

75. Garcia, M. and D. Clague, *The 2D electric field above a planar sequence of independent strip electrodes (vol 33, pg 1747, 2000).* Journal of Physics D-Applied Physics, 2000. **33**(20): p. 2669-2669.

76. Washizu, M. and T.B. Jones, *Multipolar Dielectrophoretic Force Calculation.* Journal of Electrostatics, 1994. **33**(2): p. 187-198.

77. Jones, T.B. and M. Washizu, *Multipolar dielectrophoretic and electrorotation theory.* Journal of Electrostatics, 1996. **37**(1-2): p. 121-134.

78. Washizu, M. and T.B. Jones, *Generalized multipolar dielectrophoretic force and electrorotational torque calculation.* Journal of Electrostatics, 1996. **38**(3): p. 199-211.

79. Nili, H. and N.G. Green, *Higher-order dielectrophoresis of nonspherical particles.* Physical Review E, 2014. **89**(6).

80. Green, N.G. and T.B. Jones, *Numerical determination of the effective moments of non-spherical particles.* Journal of Physics D-Applied Physics, 2007. **40**(1): p. 78-85.

81. Ryan, H.M. and C.A. Walley, *Field Auxiliary Factors for Simple Electrode Geometries.* Proceedings of the Institution of Electrical Engineers-London, 1967. **114**(10): p. 1529-&.

82. Kang, K.H. and D.Q. Li, *Dielectric force and relative motion between two spherical particles in electrophoresis.* Langmuir, 2006. **22**(4): p. 1602-1608.

83. Lee, K.H., J. Chung, and J. Lee, *Superimposed AC- and DC electric field guided deposition of a single DNA molecule along a microfabricated gap.* 2003 Third Ieee Conference on Nanotechnology, Vols One and Two, Proceedings, 2003: p. 729-732.

84. Glowinski, R., T.W. Pan, T.I. Hesla, and D.D. Joseph, *A distributed Lagrange multiplier fictitious domain method for particulate flows.* International Journal of Multiphase Flow, 1999. **25**(5): p. 755-794.

85. Johnson, A.A. and T.E. Tezduyar, *3D simulation of fluid-particle interactions with the number of particles reaching 100.* Computer Methods in Applied Mechanics and Engineering, 1997. **145**(3-4): p. 301-321.

86. Choi, H.G. and D.D. Joseph, *Fluidization by lift of 300 circular particles in plane Poiseuille flow by direct numerical simulation.* Journal of Fluid Mechanics, 2001. **438**: p. 101-128.

87. Aidun, C.K. and J.R. Clausen, *Lattice-Boltzmann Method for Complex Flows.* Annual Review of Fluid Mechanics, 2010. **42**: p. 439-472.

88. Wu, J.S. and C.K. Aidun, *Simulating 3D deformable particle suspensions using lattice Boltzmann method with discrete external boundary force.* International Journal for Numerical Methods in Fluids, 2010. **62**(7): p. 765-783.

89. Glowinski, R., T.W. Pan, T.I. Hesla, D.D. Joseph, and J. Periaux, *A distributed Lagrange multiplier/fictitious domain method for the simulation of flow around moving rigid bodies: application to particulate flow.* Computer Methods in Applied Mechanics and Engineering, 2000. **184**(2-4): p. 241-267.

90. Glowinski, R. and O. Pironneau, *Finite-Element Methods for Navier-Stokes Equations.* Annual Review of Fluid Mechanics, 1992. **24**: p. 167-204.

91. Pan, T.W. and R. Glowinski, *Direct simulation of the motion of neutrally buoyant circular cylinders in plane Poiseuille flow.* Journal of Computational Physics, 2002. **181**(1): p. 260-279.

92. Pan, T.W. and R. Glowinski, *Direct simulation of the motion of neutrally buoyant balls in a three-dimensional Poiseuille flow.* Comptes Rendus Mecanique, 2005. **333**(12): p. 884-895.

93. Huang, H.B., Z.T. Li, S.A.S.A. Liu, and X.Y. Lu, *Shan-and-Chen-type multiphase lattice Boltzmann study of viscous coupling effects for two-phase flow in porous media.* International Journal for Numerical Methods in Fluids, 2009. **61**(3): p. 341-354.

94. Inamuro, T., T. Ogata, S. Tajima, and N. Konishi, *A lattice Boltzmann method for incompressible two-phase flows with large density differences.* Journal of Computational Physics, 2004. **198**(2): p. 628-644.

95. Glowinski, R., T.W. Pan, T.I. Hesla, D.D. Joseph, and J. Periaux, *A distributed Lagrange multiplier/fictitious domain method for flows around moving rigid bodies: Application to particulate flow.* International Journal for Numerical Methods in Fluids, 1999. **30**(8): p. 1043-1066.

96. Hu, H.H., D.D. Joseph, and M.J. Crochet, *Direct simulation of fluid particle motions.* Theoretical and Computational Fluid Dynamics, 1992. **3**(5): p. 285-306.

97. Singh, P., D.D. Joseph, T.I. Hesla, R. Glowinski, and T.W. Pan, *A distributed Lagrange multiplier/fictitious domain method for viscoelastic particulate flows.* Journal of Non-Newtonian Fluid Mechanics, 2000. **91**(2-3): p. 165-188.

98. Bertrand, F., P.A. Tanguy, and F. Thibault, *A three-dimensional fictitious domain method for incompressible fluid flow problems.* International Journal for Numerical Methods in Fluids, 1997. **25**(6): p. 719-736.

99. Glowinski, R., T.W. Pan, and J. Periaux, *Distributed Lagrange multiplier methods for incompressible viscous flow around moving rigid bodies.* Computer Methods in Applied Mechanics and Engineering, 1998. **151**(1-2): p. 181-194.

100. Chorin, A.J., *A numerical method for solving incompressible viscous flow problems (Reprinted from the Journal of Computational Physics, vol 2, pg 12-26, 1997).* Journal of Computational Physics, 1997. **135**(2): p. 118-125.

101. Chorin, A.J., *On the Convergence of Discrete Approximations to the Navier-Stokes Equations.* Mathematics of Computation, 1969. **23**(106): p. 341-353.

102. Chorin, A.J., *Numerical study of slightly viscous flow.* Journal of Fluid Mechanics, 1973. **57**: p. 785-796.

103. Turek, S., *A comparative study of time-stepping techniques for the incompressible Navier-Stokes equations: From fully implicit non-linear schemes to semi-implicit projection methods.* International Journal for Numerical Methods in Fluids, 1996. **22**(10): p. 987-1011.

104. Marchuk, G.I., *Splitting and alternating direction methods*, in *Handbook of Numerical Analysis*, P.G. Ciarlet and J.L. Lions, Editors. 1990, Elsevier. p. 197-462.

105. Chen, R.J., S. Bangsaruntip, K.A. Drouvalakis, N.W.S. Kam, M. Shim, Y.M. Li, W. Kim, P.J. Utz, and H.J. Dai, *Noncovalent functionalization of carbon nanotubes for highly specific electronic biosensors.* Proceedings of the National Academy of Sciences of the United States of America, 2003. **100**(9): p. 4984-4989.

106. Cui, Y., Q.Q. Wei, H.K. Park, and C.M. Lieber, *Nanowire nanosensors for highly sensitive and selective detection of biological and chemical species.* Science, 2001. **293**(5533): p. 1289-1292.

107. Hu, J.T., T.W. Odom, and C.M. Lieber, *Chemistry and physics in one dimension: Synthesis and properties of nanowires and nanotubes.* Accounts of Chemical Research, 1999. **32**(5): p. 435-445.

108. Smith, B.W., Z. Benes, D.E. Luzzi, J.E. Fischer, D.A. Walters, M.J. Casavant, J. Schmidt, and R.E. Smalley, *Structural anisotropy of magnetically aligned single wall carbon nanotube films.* Applied Physics Letters, 2000. **77**(5): p. 663-665.

109. van der Zande, B.M.I., G.J.M. Koper, and H.N.W. Lekkerkerker, *Alignment of rod-shaped gold particles by electric fields.* Journal of Physical Chemistry B, 1999. **103**(28): p. 5754-5760.

110. Chung, J.Y., K.H. Lee, J.H. Lee, and R.S. Ruoff, *Toward large-scale integration of carbon nanotubes.* Langmuir, 2004. **20**(8): p. 3011-3017.

111. Holmes, J.D., K.P. Johnston, R.C. Doty, and B.A. Korgel, *Control of thickness and orientation of solution-grown silicon nanowires.* Science, 2000. **287**(5457): p. 1471-1473.

112. Cassell, A.M., N.R. Franklin, T.W. Tombler, E.M. Chan, J. Han, and H.J. Dai, *Directed growth of free-standingsingle-walled carbon nanotubes.* Journal of the American Chemical Society, 1999. **121**(34): p. 7975-7976.

113. Kretschmer, R. and W. Fritzsche, *Pearl chain formation of nanoparticles in microelectrode gaps by dielectrophoresis.* Langmuir, 2004. **20**(26): p. 11797-11801.

114. Husken, N., R.W. Taylor, D. Zigah, J.C. Taveau, O. Lambert, O.A. Scherman, J.J. Baumberg, and A. Kuhn, *Electrokinetic Assembly of One-Dimensional Nanoparticle Chains with Cucurbit[7]uril Controlled Subnanometer Junctions.* Nano Letters, 2013. **13**(12): p. 6016-6022.

115. Zhang, L. and Y.X. Zhu, *Directed Assembly of Janus Particles under High Frequency ac-Electric Fields: Effects of Medium Conductivity and Colloidal Surface Chemistry.* Langmuir, 2012. **28**(37): p. 13201-13207.

116. Lumsdon, S.O., E.W. Kaler, and O.D. Velev, *Two-dimensional crystallization of microspheres by a coplanar AC electric field.* Langmuir, 2004. **20**(6): p. 2108-2116.

117. Velev, O.D. and K.H. Bhatt, *On-chip micromanipulation and assembly of colloidal particles by electric fields.* Soft Matter, 2006. **2**(9): p. 738-750.

118. Simonova, T.S., V.N. Shilov, and O.A. Shramko, *Low-frequency dielectrophoresis and the polarization interaction of uncharged spherical particles with an induced Debye atmosphere of arbitrary thickness.* Colloid Journal, 2001. **63**(1): p. 108-115.

119. Yariv, E., *Inertia-induced electrophoretic interactions.* Physics of Fluids, 2004. **16**(4): p. L24-L27.

120. Wilson, H.J., L.A. Pietraszewski, and R.H. Davis, *Aggregation of charged particles under electrophoresis or gravity at arbitrary Peclet numbers.* Journal of Colloid and Interface Science, 2000. **221**(1): p. 87-103.

121. Masuda, S., M. Washizu, and M. Iwadare, *Separation of Small Particles Suspended in Liquid by Nonuniform Traveling Field.* Ieee Transactions on Industry Applications, 1987. **23**(3): p. 474-480.

122. Hagedorn, R., G. Fuhr, T. Muller, and J. Gimsa, *Traveling-Wave Dielectrophoresis of Microparticles.* Electrophoresis, 1992. **13**(1-2): p. 49-54.

123. Morgan, H., A.G. Izquierdo, D. Bakewell, N.G. Green, and A. Ramos, *The dielectrophoretic and travelling wave forces generated by interdigitated electrode arrays: analytical solution using Fourier series (vol 34, pg 1553, 2001).* Journal of Physics D-Applied Physics, 2001. **34**(17): p. 2708-2708.

124. Hughes, M.P., R. Pethig, and X.B. Wang, *Dielectrophoretic forces on particles in travelling electric fields.* Journal of Physics D-Applied Physics, 1996. **29**(2): p. 474-482.

125. Talary, M.S., J.P.H. Burt, J.A. Tame, and R. Pethig, *Electromanipulation and separation of cells using travelling electric fields.* Journal of Physics D-Applied Physics, 1996. **29**(8): p. 2198-2203.

126. Morgan, H., N.G. Green, M.P. Hughes, W. Monaghan, and T.C. Tan, *Large-area travelling-wave dielectrophoresis particle separator.* Journal of Micromechanics and Microengineering, 1997. **7**(2): p. 65-70.

127. Lin, Z.H., *Two Phase Flow Measurement With Sharp Edge Orifices.* Int. J. Multiphase Flow, 1982(8): p. 10.

128. Lo, Y.J., Y.Y. Lin, U. Lei, M.S. Wu, and P.C. Yang, *Measurement of the Clausius-Mossotti factor of generalized dielectrophoresis.* Applied Physics Letters, 2014. **104**(8).

129. Qian, C., H.B. Huang, L.G. Chen, X.P. Li, Z.B. Ge, T. Chen, Z. Yang, and L.N. Sun, *Dielectrophoresis for Bioparticle Manipulation.* International Journal of Molecular Sciences, 2014. **15**(10): p. 18281-18309.

130. Sebastian, A., A.M. Buckle, and G.H. Markx, *Tissue engineering with electric fields: Immobilization of mammalian cells in multilayer aggregates using dielectrophoresis.* Biotechnology and Bioengineering, 2007. **98**(3): p. 694-700.

131. Braff, W.A., D. Willner, P. Hugenholtz, K. Rabaey, and C.R. Buie, *Dielectrophoresis-Based Discrimination of Bacteria at the Strain Level Based on Their Surface Properties.* Plos One, 2013. **8**(10).

132. Robins, M. and A. Fillery-Travis, *Colloidal dispersions. Edited by W. B. Russel, D. A. Saville & W. R. Schowalter, Cambridge University Press, Cambridge, UK, 1989, xvii + 506 pp., price: £60.00. ISBN 0 521 34188 4.* Journal of Chemical Technology & Biotechnology, 1992. **54**(2): p. 201-202.

133. Happel, J. and H. Brenner, *Low Reynolds number hydrodynamics: with special applications to particulate media*. Vol. 1. 2012: Springer Science & Business Media.

134. He, G.L. and D. Liu, *Coupled Electrohydrodynamic-Dielectrophoretic Pumping of Colloidal Suspensions in a Microchannel.* Proceedings If the Asme 9th International Conference on Nanochannels, Microchannels and Minichannels 2011, Vol 1, 2012: p. 219-227.

135. Hilt, J.Z. and N.A. Peppas, *Microfabricated drug delivery devices.* International Journal of Pharmaceutics, 2005. **306**(1-2): p. 15-23.

136. Sahoo, H.R., J.G. Kralj, and K.F. Jensen, *Multistep continuous-flow microchemical synthesis involving multiple reactions and separations.* Angewandte Chemie-International Edition, 2007. **46**(30): p. 5704-5708.

137. Erickson, D. and D.Q. Li, *Integrated microfluidic devices.* Analytica Chimica Acta, 2004. **507**(1): p. 11-26.

138. Singhal, V. and S.V. Garimella, *Induction electrohydrodynamics micropump for high heat flux cooling.* Sensors and Actuators A: Physical, 2007. **134**(2): p. 650-659.

139. Iverson, B.D. and S.V. Garimella, *Recent advances in microscale pumping technologies: a review and evaluation.* Microfluidics and Nanofluidics, 2008. **5**(2): p. 145-174.

140. Singhal, V., S.V. Garimella, and A. Raman, *Microscale pumping technologies for microchannel cooling systems.* Applied Mechanics Reviews, 2004. **57**(3): p. 191-221.

141. Cahill, B.P., L.J. Heyderman, J. Gobrecht, and A. Stemmer, *Electro-osmotic pumping on application of phase-shifted signals to interdigitated electrodes.* Sensors and Actuators B: Chemical, 2005. **110**(1): p. 157-163.

142. Ramos, A., H. Morgan, N.G. Green, A. Gonzalez, and A. Castellanos, *Pumping of liquids with traveling-wave electroosmosis.* Journal of Applied Physics, 2005. **97**(8): p. 084906 - 084906-8

143. Go, D.B., S.V. Garimella, T.S. Fisher, and R.K. Mongia, *Ionic winds for locally enhanced cooling.* Journal of Applied Physics, 2007. **102**(5): p. 053302 - 053302-8

144. Singhal, V. and S.V. Garimella, *A novel valveless micropump with electrohydrodynamic enhancement for high heat flux cooling.* Ieee Transactions on Advanced Packaging, 2005. **28**(2): p. 216-230.

145. Zhang, W., T.S. Fisher, and S.V. Garimella, *Simulation of ion generation and breakdown in atmospheric air.* Journal of Applied Physics, 2004. **96**(11): p. 6066-6072.

146. Ramos, A., H. Morgan, N.G. Green, and A. Castellanos, *AC electric-field-induced fluid flow in microelectrodes.* Journal of Colloid and Interface Science, 1999. **217**(2): p. 420-422.

147. Iverson, B.D., L. Cremaschi, and S.V. Garimella, *Effects of discrete-electrode configuration on traveling-wave electrohydrodynamic pumping.* Microfluidics and Nanofluidics, 2009. **6**(2): p. 221-230.

148. Melcher, J.R., *Traveling-Wave Induced Electroconvection.* Physics of Fluids, 1966. **9**(8): p. 1548-&.

149. Melcher, J.R. and M.S. Firebaugh, *Traveling-wave bulk electroconvection induced across a temperature gradient.* The Physics of Fluids, 1967. **10**(6): p. 1178 - 1185.

150. Morgan, H., A.G. Izquierdo, D. Bakewell, N.G. Green, and A. Ramos, *The dielectrophoretic and travelling wave forces generated by interdigitated electrode*

arrays: analytical solution using Fourier series. Journal of Physics D: Applied Physics, 2001. **34**(17): p. 2708-2708.

151. Seyed-Yagoobi, J. and J.E. Bryan, *Enhancement of heat transfer and mass transport in thermal equipment with electrohydrodynamics*, in *Electrostatics*, D.M. Taylor, Editor. 1999. p. 127-130.

152. Yazdani, M. and J. Seyed-Yagoobi, *Heat transfer augmentation of parallel flows by means of electric conduction phenomenon in macro- and Microscales.* Journal of Heat Transfer-Transactions of the ASME, 2010. **132**(6): p. 062402 - 062402-9.

153. Yazdani, M. and J. Seyed-Yagoobi, *An electrically driven impinging liquid jet for direct cooling of heated surfaces.* Ieee Transactions on Industry Applications, 2010. **46**(2): p. 650-658.

154. Lian, M. and J. Wu, *Microfluidic flow reversal at low frequency by AC electrothermal effect.* Microfluidics and Nanofluidics, 2009. **7**(6): p. 757-765.

155. Ramos, A., H. Morgan, N.G. Green, and A. Castellanos, *AC electrokinetics: a review of forces in microelectrode structures.* Journal of Physics D: Applied Physics, 1998. **31**(18): p. 2338-2353.

156. Stratton, J.A., *Electromagnetic theory*. 1941, New York: McGraw-Hill.

157. Green, N.G., A. Ramos, A. Gonzalez, A. Castellanos, and H. Morgan, *Electrothermally induced fluid flow on microelectrodes.* Journal of Electrostatics, 2001. **53**(2): p. 71-87.

158. Happel, J. and H. Brenner, *Low Reynolds Number Hydrodynamics*. 1983: Springer.

159. Lee, P.S., S.V. Garimella, and D. Liu, *Investigation of heat transfer in rectangular microchannels.* International Journal of Heat and Mass Transfer, 2005. **48**(9): p. 1688-1704.

160. Incropera, F.P., D.P. DeWitt, T.L. Bergman, and A.S. Lavine, *Fundamentals of Heat and Mass Transfer*. 2005, Hoboken: John Wiley & Sons.

161. *FLUENT 6 User's Guide, 2000*. FLUENT Inc.: Lebanon, NH.

162. Arno, R., *Camo Elettrico Rotante per Mezzo di Difference di Potenziali Alternative.* Atti Accad. Nuz. Lincei Rend, 1892. **1**.

163. Keis, A., *Über die Beweglichkeit der elektrolytischen Ionen. Über Erkennungsenergie und Sublimationswärme bei Alkalihalogeniden und Halogenwasserstoffen.* Zeitschrift für Elektrochemie und angewandte physikalische Chemie, 1920. **26**(19-20): p. 408-412.

164. Lertes, P., *Untersuchungen über Rotationen von dielektrischen Flüssigkeiten im elektrostatischen Drehfeld.* Zeitschrift für Physik, 1921. **4**(3): p. 315-336.

165. Lertes, P., *Der Dipolrotationseffekt bei dielektrischen Flüssigkeiten.* Zeitschrift für Physik, 1921. **6**(1): p. 56-68.

166. Pickard, W.F., *On the born-lertes rotational effect.* Il Nuovo Cimento, 1961. **21**(2): p. 316-332.

167. Holzapfel, C., J. Vienken, and U. Zimmermann, *Rotation of Cells in an Alternating Electric-Field - Theory and Experimental Proof.* Journal of Membrane Biology, 1982. **67**(1): p. 13-26.

168. Goater, A. and R. Pethig, *Electrorotation and dielectrophoresis.* Parasitology, 1999. **117**(07): p. 177-189.

169. Chan, K.L., P.R.C. Gascoyne, F.F. Becker, and R. Pethig, *Electrorotation of liposomes: verification of dielectric multi-shell model for cells.* Biochimica Et Biophysica Acta-Lipids and Lipid Metabolism, 1997. **1349**(2): p. 182-196.

170. Swami, N., C.F. Chou, V. Ramamurthy, and V. Chaurey, *Enhancing DNA hybridization kinetics through constriction-based dielectrophoresis.* Lab on a Chip, 2009. **9**(22): p. 3212-3220.

171. Sanghavi, B.J., W. Varhue, J.L. Chavez, C.F. Chou, and N.S. Swami, *Electrokinetic Preconcentration and Detection of Neuropeptides at Patterned Graphene-Modified Electrodes in a Nanochannel.* Analytical Chemistry, 2014. **86**(9): p. 4120-4125.

172. Fauss, E.K., R.I. MacCuspie, V. Oyanedel-Craver, J.A. Smith, and N.S. Swami, *Disinfection action of electrostatic versus steric-stabilized silver nanoparticles on E. coli under different water chemistries.* Colloids and Surfaces B-Biointerfaces, 2014. **113**: p. 77-84.

173. Chiou, C.H., J.C. Pan, L.J. Chien, Y.Y. Lin, and J.L. Lin, *Characterization of Microparticle Separation Utilizing Electrokinesis within an Electrodeless Dielectrophoresis Chip.* Sensors, 2013. **13**(3): p. 2763-2776.